Lenses for the Unresolved: Probing the Stellar Initial Mass Function of Nearby Massive Early-Type Galaxies

WILLIAM PAUL COLLIER

Lenses for the Unresolved: Probing the Stellar Initial Mass Function of Nearby Massive Early-Type Galaxies

William Collier

A Thesis presented for the degree of
Doctor of Philosophy

Centre for Extragalactic Astrophysics
Ogden Centre for Fundamental Physics
Department of Physics
Durham University
United Kingdom

March 2020

Lenses for the Unresolved: Probing the Stellar Initial Mass Function of Nearby Massive Early-Type Galaxies

William Collier

Submitted for the degree of Doctor of Philosophy

March 2020

Abstract:

The stellar initial mass function (IMF) is a key component of understanding galaxy formation and evolution, and to interpret observed properties (e.g. estimating stellar masses). In the different star-forming environments of the Milky Way (MW), the IMF is well constrained and approximately invariant. However, stellar populations within massive elliptical galaxies were likely formed by short, intense star formation events at early times, and recent observations suggest their cores deviate from a universal IMF. Studies using spectral analysis, stellar dynamics, and gravitational lensing report that for the most massive galaxies (velocity dispersion $\sigma \geq 300$ km s^{-1}), the measured stellar mass-to-light ratios (Υ) are a factor of two larger than implied by a MW-like IMF. However, a subset of three low-z early-type galaxy (ETG) strong-gravitational lenses (SNL-0, SNL-1, and SNL-2) with $\sigma \simeq 300\,\mathrm{kms}^{-1}$ appear to contradict these results. The Υ measured from lensing analyses are consistent with a MW-like IMF, i.e. Kroupa with $\langle\alpha\rangle = 1.06 \pm 0.08$. The mass-excess parameter, α, is relative to the MW, defining 1 as a MW-like IMF, and 1.64 as a Salpeter IMF. These lenses are situated at low-z where, due to the geometry of the lens, the contribution from dark matter within the Einstein radius is lower than for a more distant lens. In this thesis, I investigate the IMF within low-z massive strong-lensing ETGs. The analysis comprises two main parts. First, a re-analysis of two low-z lenses, SNL-1 and SNL-2, using high-resolution *Hubble Space Telescope* data. For SNL-1, I

break the mass-shear degeneracy and measure α relative to the MW as $\alpha = 1.17 \pm 0.09$. For SNL-2, the mass of the similar brightness companion galaxy is constrained. The derived α is 0.96 ± 0.10. Both are consistent with a MW-like IMF and inconsistent with Salpeter or 'heavier' IMFs. The second part of this thesis is a new lens search, using the ESO/VLT Multi-Unit Spectroscopic Explorer (MUSE). The search consists of a targeted survey with new observations specific to the search (MNELLS), and an archival search of data observed for other science. The search yielded one new galaxy-scale lens, J0403-0239, three cluster-scale lenses, and nine galaxy-scale systems in which a single background source is detected within 6 arcsec. J0403-0239 lies at $z = 0.0665$ and has two extremely bright and extended lensed images at $z = 0.1965$. Although the lens is at a slightly higher redshift than the other low-z lenses, the Einstein radius probes just one-quarter of the effective radius. The measured Υ is consistent with a MW-like IMF, $\alpha = 1.16 \pm 0.09$, with a robustly determined old stellar population. Each galaxy-scale lens or singly imaged system is used to constrain the parameters for the ensemble population of the IMF within ETGs. The population has $\langle\alpha\rangle = 1.06 \pm 0.08$ and an upper limit on the intrinsic scatter of $\nu = 0.24$, at 90 per cent confidence. These constraints are consistent with Salpeter only at the $2.4\,\sigma$ level.

Declaration

The work described in this thesis was undertaken between October 2016 and March 2020 while the author was a research student under the supervision of Dr. Russell J. Smith and Dr. John R. Lucey in the Centre for Extragalactic Astrophysics at Durham University, England. No part of this thesis has been submitted for any degree or qualification at Durham University or elsewhere.

Chapter 3 closely follows the publication:

"Improved mass constraints for two nearby strong-lensing elliptical galaxies from Hubble Space Telescope imaging"; Collier W. P., Smith R. J., Lucey J. R., 2018a, MNRAS, 473, 1103

Chapters 4, 5, and 7 closely follow the publication:

MNELLS: The MUSE Nearby Early-Type Galaxy Lens Locator Survey; Collier W. P., Smith R. J., Lucey J. R., 2020, MNRAS accepted, 10.1093/mnras/staa602, arXiv:2002.07191

Chapter 6 closely follows the publication:

A new strong-lensing galaxy at z= 0.066: another elliptical galaxy with a lightweight IMF; Collier W. P., Smith R. J., Lucey J. R., 2018b, MNRAS, 478, 1595

In addition to the work presented in this thesis, the author has also been involved in the following work during the period of their PhD:

'Upper-limit lensing': constraining galaxy stellar masses with singly imaged background sources; Smith R. J., Lucey J. R., Collier W. P., 2018, MNRAS, 481, 2115

Subaru FOCAS IFU observations of two z ≃ 0.12 strong-lensing elliptical galaxies from SDSS MaNGA; Smith R. J., Collier W. P., Ozaki S., Lucey J. R., 2020, MNRAS, 493, L33

All figures in this thesis were prepared by the author, or have been properly attributed in the figure caption.

List of Abbreviations and Acronyms

Here I list some of the most frequently used Abbreviations and Acronyms.

SNELLS: SINFONI nearby elliptical lens locator survey

MNELLS: MUSE nearby early-type lens locator survey

SLACS: Sloan Lens ACS survey

MaNGA: Mapping galaxies at the Apache point observatory

HST: *Hubble Space Telescope*

MW: Milky Way

DM: Dark matter

IMF: stellar initial mass function

ETG: Early-type galaxy

FoV: field-of-view

Acknowledgements

Four years is a long time. Here I would like to pay thanks to the people who have helped me during the last four. Of course, thanks to the CEA for everything they have provided in the last four years, and to Alan Lotts for excellent tech support, in the form of screens, storage allowance and many other ways I probably never noticed.

First, to Russell and John. Thank you for all of your support throughout. In particular, I would like to thank Russell for his expertise during the last 3 and a half years of supervision. Without it, my knowledge, and this thesis would undoubtedly be very different. John, thank you for all of the time you have put in. Especially in the last month guiding the structure and careful use of language within this thesis, even with the change to working from home. If there are any poorly written sentences, misspellings, or overabundance of commas,(!) it should be known that these are the purest form of my writing style and not a lack of care from my supervision.

Second, to friends in Physics. There have been many people during my time at Durham within the physics department that I have chatted with, whether whilst teaching, during coffee (yuck!), breaks or in the office. Every person has made Physics a more entertaining place to be. There are too many of you to name one-by-one, but I am grateful to you all. Special thanks to Ollie for all of his helpful comments during the writing of this thesis, both relevant and not, whilst sharing a table, generally excellent(?) humour, and delightful meatballs. I hope by the time he reads this, he is back in Lyon having a wonderful time. Also to Stuart, for outdoing any expectations of his cynicism time and time again. The office would have been a very different place without it.

There are few people who know me, who do not know I play frisbee. It has a stupid name, but in the last four years, it has offered me the chance to play with some great people. To Durham, I am gutted this season was ruined, but every previous season we ruined by ourselves. However, the memory of coming second at indoor nationals will stay with me for a long time. Thanks to Cal, Kenn, and Dylan along with Kate, Sarah, Ellie and Lizzie who amongst many have put up with my unending nonsense. To Smog, I wish you were Brum, but I suppose winning a national title has made up for that. Special thanks to Lexi, and Fras for the motivation and asking for lifts, Carlo for his punctuality and midday gym attendance, and Tush for making me smile, and also for a place to stay and write a thesis. Frisbee has undoubtedly kept me sane, and pushed me to be a better person. Or at least helped me condense all of my terrible chat into one part of my life.

Oh, and Steve. I think this is the part where the author is supposed to talk about their partner or something, which, I suppose if you talk to anyone from DUF or Astronomy, I sort of am. You've been a great officemate, a great housemate, a great teammate and a great friend. Thanks.

Finally, to my family, they have supported me in every decision I have made, not just in the last four years, but every year before that. Everyone else I have mentioned has been important, but not one has been with me as long as my parents. Although, I suppose that is true for every person, at least, whilst their parents are living. So, thank you to my parents and sister for always making me laugh, checking up on how I am, helping me out and feeding me until I can't eat anymore at Christmas, the weekend, the weekday, whenever.

Contents

List of Figures

List of Tables

CHAPTER 1

Introduction

1.1 Galaxies in the Universe

The production of glass from sand is a technique that has existed for thousands of years. However, the alignment of two glass lenses to magnify distant objects was first reported, only, in the early 1600s by Dutch 'eyeglass maker' Hans Lippershey, who unsuccessfully attempted to patent the design. The first astronomer to point a refracting telescope skyward was Galileo. He used an instrument of his own design to observe the rings of Saturn amongst other objects in the Solar System.

Beyond the Solar System, is the Milky Way itself. The plume of dust and stars which stretches across the night sky invites an observer to imagine untold numbers of solar systems, spread throughout a single gravitationally bound structure.

As astronomy moved forward and telescope designs continued to improve, numerous "nebulus" objects (Messier, 1781) were recorded across the sky. However, the exact location of these objects was much debated, with some groups placing them inside the MW (Shapley & Curtis, 1921). But, in 1925, Edwin Hubble used the 100-inch telescope on Mount Wilson Observatory to resolve spiral arms, and invoke the distance relation for

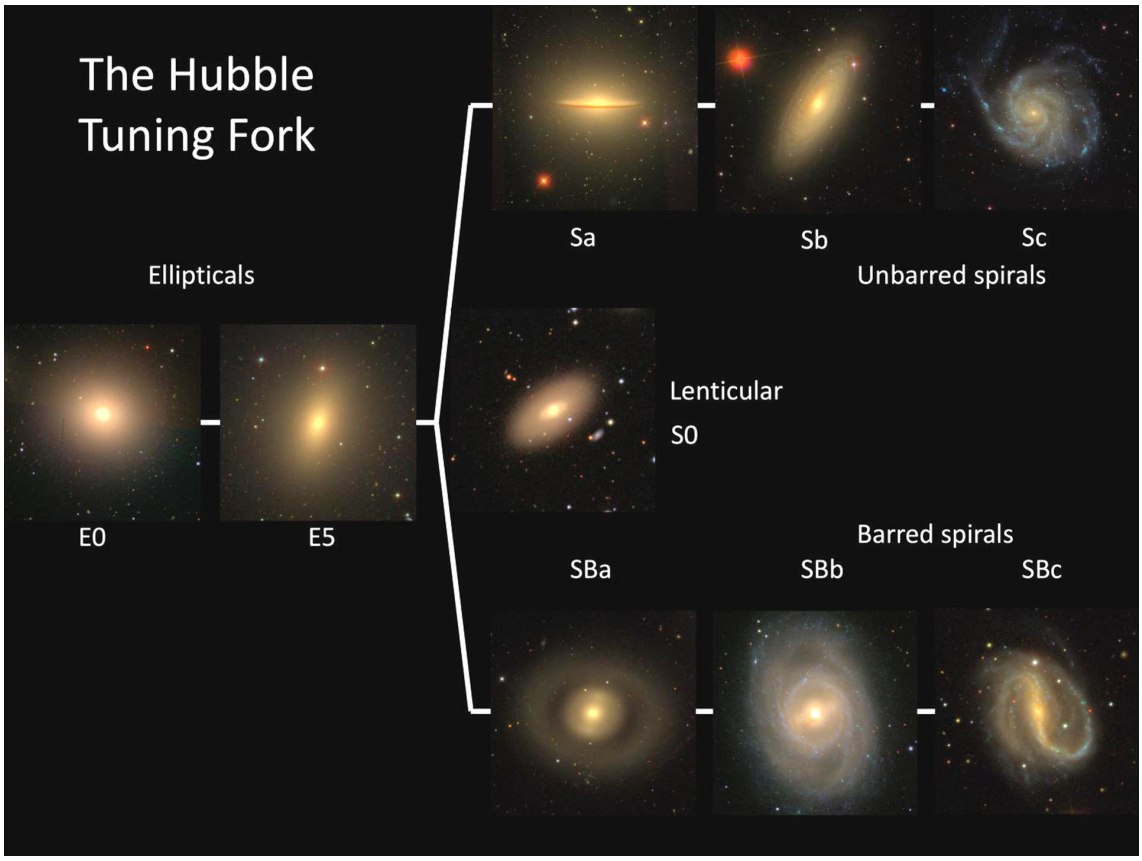

Figure 1.1: The Hubble tuning fork, developed in 1926 to classify galaxies via their morphological appearance. Image credit: Karen Masters, Sloan Digital Sky Survey.

Cepheid stars (discovered by Leavitt & Pickering, 1913) to show that these objects must lie outside of the Milky Way (Hubble, 1925).

At the simplest level, galaxies can be separated into two main categories based on their observed appearance (morphology, see Sandage, 2005, and references therein), and see Figure 1.1. The "late-type" or ‘spiral’ galaxies exhibit distinctive arms in their light profiles. Within this classification are two subsets, those with bars (SB) and those without (S). Within those subsets, galaxies are further categorized by the tightness of the spiral arms from a-c. The term "early-type" incorporates both ‘elliptical’ and S0 galaxies. Elliptical galaxies exhibit smooth light profiles and are labelled by increasing ellipticity, from E0 to E7. S0 or ‘lenticular’ galaxies exhibit a central bulge but contain no spiral arms. The ‘irregular’ galaxies fit neither of the previous classifications, typically exhibiting a clumpy structure.

The use of "early-" and "late-" might encourage the idea of an evolutionary path, especially

with the layout of the tuning fork. This is not intended to be the case and there is no direct evolution in left-to-right or vice versa in the diagram.

Late-type and early-type galaxies are typically split by visual appearance. However, other properties also differ. One case is the comparison between an optical colour and a broad-band magnitude for a population of galaxies. The resulting distribution is roughly bi-modal, with some overlap (e.g. shown in Figure 1.2 from Schawinski et al., 2014). The colour not only separates the two classifications but also it implies a difference in the stellar populations. The bluer late-type galaxies are still undergoing star formation, whereas the redder early-types typically formed the majority of their stars at $z > 2$ (Thomas et al., 2005).

Early-type galaxies are fit by several empirical scaling relations. One, the Faber-Jackson relation compares the velocity dispersion to the total luminosity (Faber & Jackson, 1976). A second is the fundamental plane, which is a much tighter relation between luminosity, velocity dispersion, effective radius and effective luminosity (Djorgovski & Davis, 1987). However, understanding why these galaxies follow these relations relies on a detailed picture of how these galaxies form.

1.2 The formation of early-type galaxies

In the 1923 paper by Edwin Hubble (Hubble, 1923), an elliptical galaxy is described as having two main characteristics. First, a rotational symmetry about the dominant non-stellar nuclei, and second, a steady decrease in luminosity from the nuclei outward. The term early-type galaxy (ETG) incorporates both elliptical galaxies and S0 galaxies.

How a galaxy forms and subsequently evolves is a surprisingly difficult question to answer. The collapse of a protogalactic cloud is one potential route to producing the present-day galaxies. Eggen, Lynden-Bell & Sandage (1962) found that within the Galaxy, metal-poor stars tend to have larger eccentricities and lower orbital angular momenta. They suggest that the smooth monolithic collapse of a protocloud with a timescale of 10^8 yrs was responsible for the MWs formation, with minimal following structural evolution.

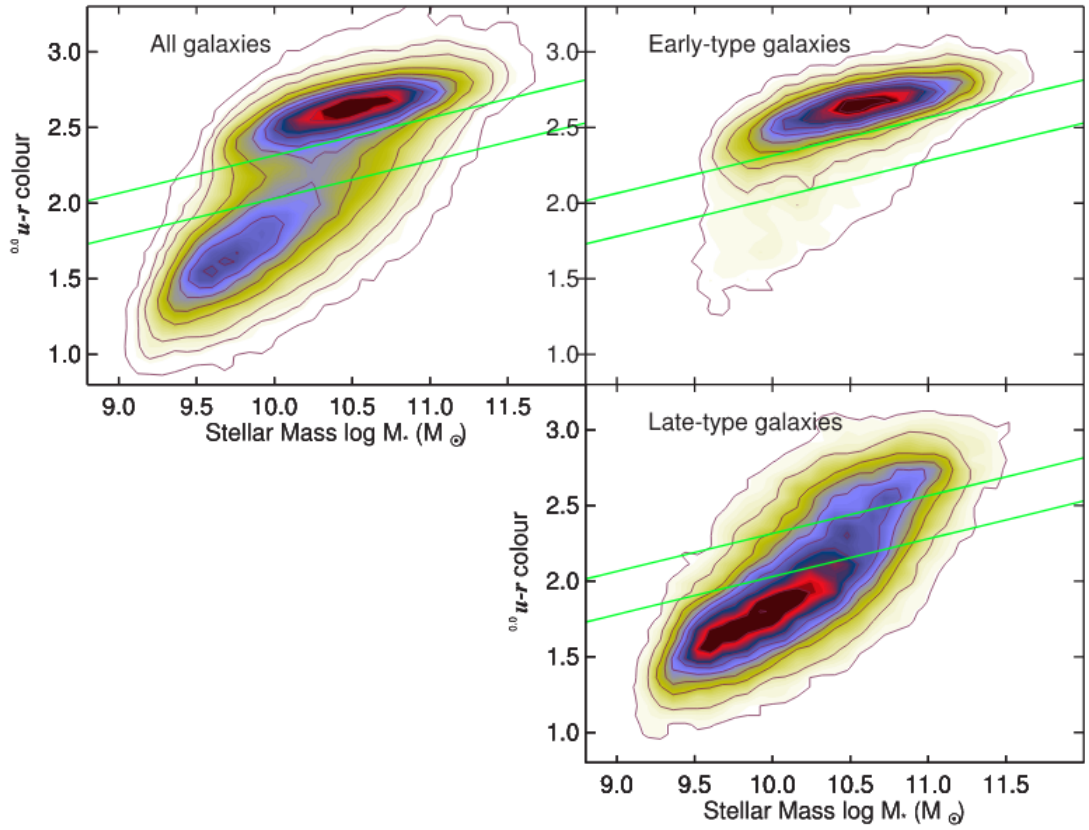

Figure 1.2: The colour-magnitude(mass) diagram taken from Schawinski et al. (2014). The *u*-*r* colour from SDSS is compared to the estimated stellar mass. In the right panels, the distribution is split by morphology, and the different locations of the populations becomes clear. Although both populations span the colour space, they are clearly peaked with early-types much redder than the peak of the late-type galaxies.

Monolithic collapse is one potential route for galaxy formation. The main alternative is an initial rapid collapse into small fragments, followed by an extended period of aggregation. In this model, the fragments have masses $\sim 10^8\,M_\odot$, and then coalesce to form the present-day galaxies. Theoretical studies have found agreement with a hierarchical growth formation route Peebles (1971); Press & Schechter (1974).

The differences between monolithic collapse and hierarchical growth have started to blur in recent times. In models with ΛCDM initial conditions, the ETG progenitors at $z = 2$–3 are predicted to be a factor of two or more smaller than the present-day (Loeb & Peebles, 2003; Naab et al., 2007). A similar picture is found observationally, galaxies similar to present-day ETGs (massive, passive) at $z \simeq 2$ are typically more compact (Daddi et al., 2005; van Dokkum et al., 2008). This implies formation from an initial massive collapse followed by a long period of accretion called inside-out growth. The inside-out growth theory is also supported by a study of lensed compact ETGs ($0.4 < z < 0.7$) which lie below the galaxy size-mass relation (Oldham et al., 2017a,b). These lensed ETGs could be the failed progenitors of the massive ETGs we observe at $z = 0$.

Typically two-thirds (~ 68 per cent) of an ETG's stellar population has formed by $z = 2$ (Thomas et al., 2005; Estrada-Carpenter et al., 2019). This star-formation history is generally well matched to the intense star-forming galaxies detected at high redshift with sub-mm observations (Whitaker et al., 2012). It also correlates with the peak of cosmic star formation at $\simeq 10$ Gyrs, (Madau & Dickinson, 2014). However, this direct evolution is complicated as high-redshift galaxies are typically observed to be disk-dominated systems (van der Wel et al., 2011), different to the dispersion-dominated cores observed in present-day massive ETGs. In either case, the star formation histories of ETGs strongly suggest that after an initial starburst, an extended period of dry mergers is required to match the observed size and mass growth. These events deposit stars onto the outskirts of the galaxy without igniting new starbursts.

Accretion only impacts the outskirts of ETGs. The core, which has experienced some of the most intense starbursts in the known universe, i.e. star-formation rates up to 1000's of solar masses per year (Sub-mm Galaxies Whitaker et al., 2012), has undergone little to no

subsequent mixing. Within the cores, the period of star formation anti-correlates with the mass of the galaxy. Due to the star-formation time scaling, the so-called α-elements are increasingly enhanced compared to iron (Fe) as a function of mass. Type II supernovae produce the α-elements, whereas the Fe abundance is enhanced by type Ia supernovae. Type Ia supernovae have low-mass progenitors which only accrete sufficient material to exceed the Chandrasekhar limit on timescales of hundreds of Myrs to Gyrs. Therefore, during short periods of star formation, type-1a supernovae will not enrich the cooling gas until after star-formation has ceased and hence the stars will not be enhanced in Fe.

The bursty star-formation histories of massive ETGs makes them an ideal test site for many physical processes involved in galaxy evolution, such as gas accretion, star formation efficiency and metal production (Oppenheimer et al., 2012; Somerville & Davé, 2015; Torrey et al., 2018). The intense star formation could lead to a different distribution of stellar mass into stars compared to the stellar populations found in late-type galaxies. The description of the mass distribution of stars is known as the stellar initial mass function.

1.3 The stellar initial mass function

Stars have produced most of the 'heavy' elements present in the Universe. The main-sequence mass of a star governs its subsequent evolutionary path and hence the range of elements which are produced. Therefore, the distribution of stellar mass in stars during star formation is key to estimating the metal enrichment of a galaxy.

The stellar initial mass function (IMF) describes the apportioning of stellar-mass into stars during a single formation event (introduced by Salpeter, 1955). Not only does the IMF directly inform the evolution of star clusters, but it is also required to study many astrophysical quantities. For example, in a typical MW-like stellar population, 80 per cent of the stellar mass resides in the dwarf stars, for a 10 per cent contribution to the bolometric luminosity. Giant stars produce the remaining 90 per cent of the bolometric luminosity for comparatively little mass. A stellar mass-to-light ratio (Υ) is measured from the parameterized IMF by co-adding stellar spectra in the appropriate ratios. The stellar

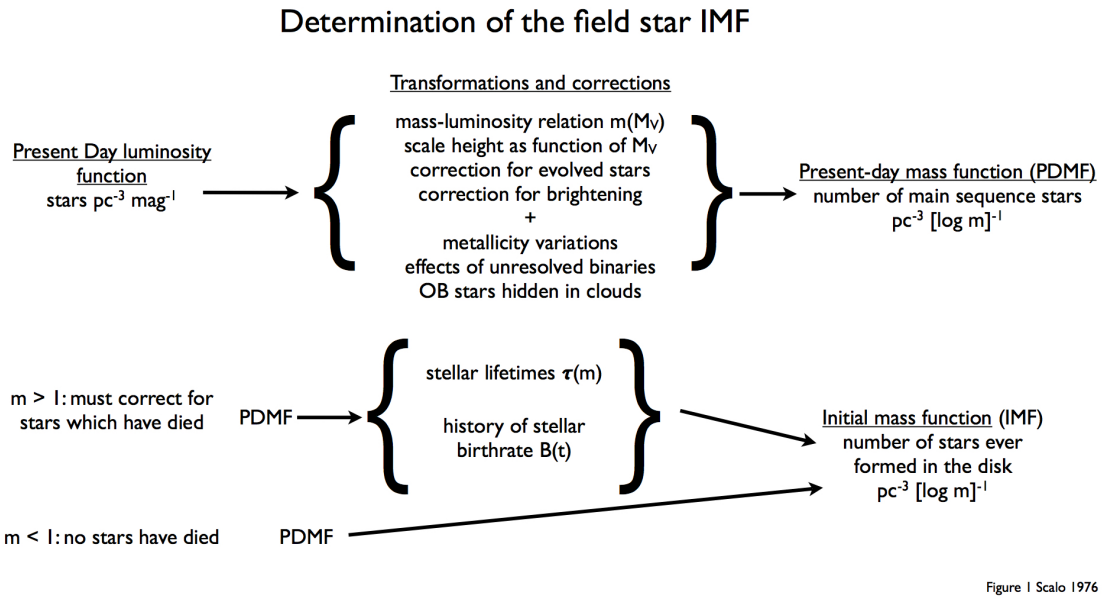

Figure 1.3: The process converting observed star counts into an initial mass function. The present day luminosity function is directly observed, and then the numerous transformations and corrections are applied. (Adapted from figure 1, Scalo, 1986).

mass of a galaxy is, therefore, the product of a measured broad-band luminosity and the predicted Υ. However, changes in the shape of the assumed IMF can significantly alter the mass predicted. It is therefore key to always caveat any measurement which requires an IMF with the shape of the IMF assumed.

Measuring an IMF?

The early IMF studies, up to and including the 1990s, were limited to stars up to 5.2 pc from the sun due to the completeness of the stellar parallax catalogue (van de Kamp, 1971). Subsequently, the volume probed was increased using a magnitude limited sample, and after accounting for observational biases a single IMF prescription was fit to both datasets (Kroupa et al., 1993). After, a complete sample of stars within the Galactic disk was observed out to 8 pc (Reid & Gizis, 1997).

Figure 1.3 highlights the complexity of measuring the IMF within a resolved stellar population. The most important quantity is a precisely measured present-day luminosity function (PDLF). All methods for measuring the PDLF involve counting the number of stars as a function of the apparent magnitude and then estimating their distances to acquire absolute magnitudes and space densities (Scalo, 1986). To generate the present-day mass

function, (PDMF), several transformations and corrections are applied to the PDLF, see Figure 1.3. After acquiring the PDMF, the age of the stellar population must be determined. For a population $\sim 10\,\mathrm{Gyrs}$ old, the observable main sequence stars will have masses $M \leq 1.0\,\mathrm{M}_{\odot}$, as the older stars will have evolved and no longer be present (Bastian et al., 2010). Therefore, a correction must be applied to account for the 'missing' stars, which requires an estimation of the star formation history (SFH). This introduces degeneracies which are dependent on the SFH chosen, and as such must be selected carefully (Elmegreen & Scalo, 2006).

The *Gaia* satellite aims to map a billion stars in the Milky-Way. However, this is only approximately 1 per cent of the total number. So far there have been two data releases covering approximately 1.3 billion sources with parallaxes and proper motions (Gaia Collaboration et al., 2018). To apply these catalogues to the IMF, complex completeness corrections must be carefully applied, such as a cross-reference with the *Tycho-2* catalogue (Bovy, 2017), or selecting stars within globular clusters (Baumgardt et al., 2019).

What is the functional form of an IMF?

When looking to describe a complex, many-parameter function, it is useful to find an elegant analytic solution to approximate the true distribution. The most commonly used function for this is the power-law distribution, and it was first used as a solution for the IMF in Salpeter (1955). They used the following form:

$$\Phi(\log m) = dN/d\log m \propto m^{-\Gamma} \tag{1.3.1}$$

This can be re-written in linear mass as a power spectrum where

$$\chi(m) = dN/dm \propto m^{-\mathrm{x}} \tag{1.3.2}$$

and $x = \Gamma + 1$. For the Salpeter slope, $\Gamma = 1.35$.

For a simple power-law, there is an arbitrarily increasing number of dwarf stars, however as instrumentation improved the IMF was investigated to lower stellar masses. In the late

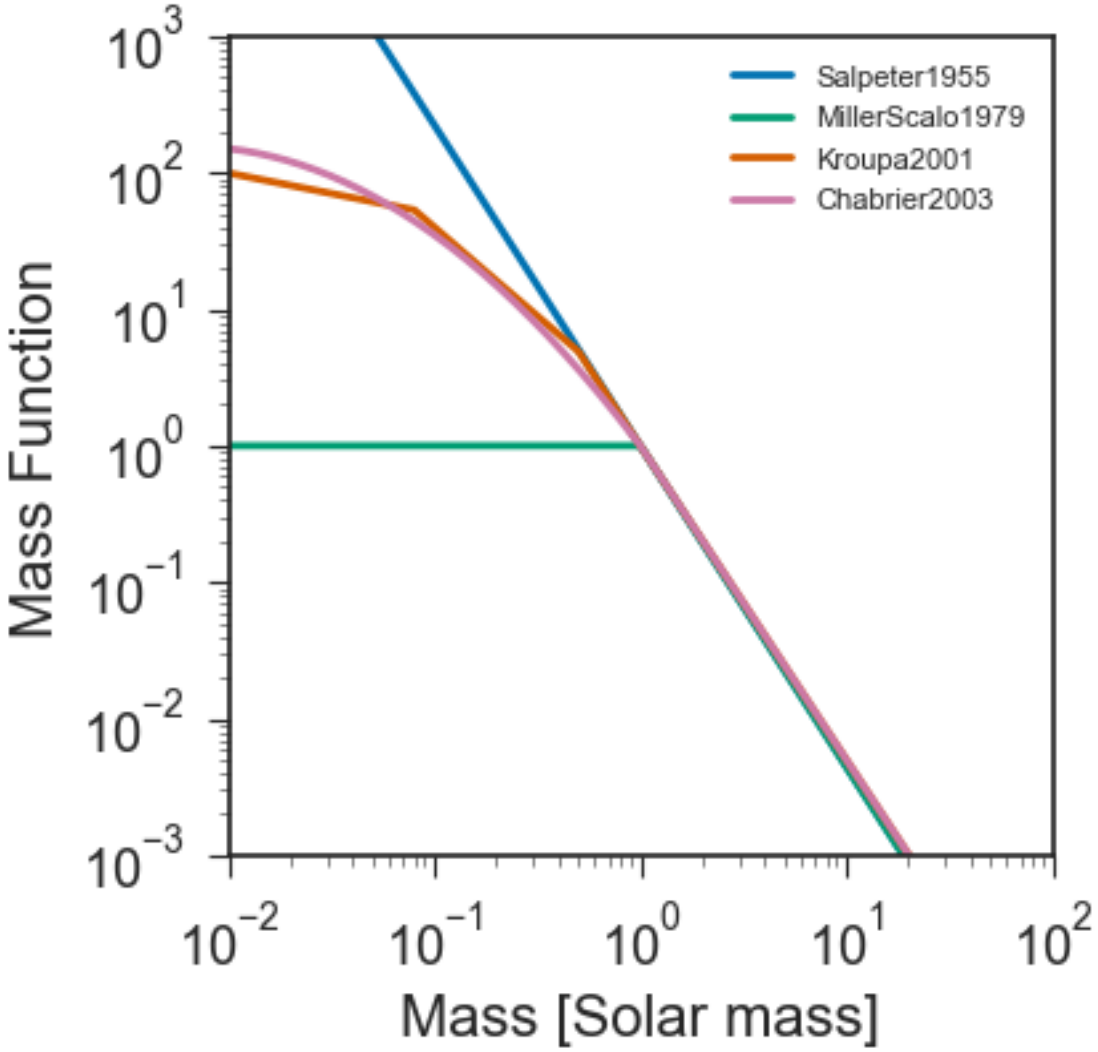

Figure 1.4: The functional form for four different IMFs. The high mass slope ($M > 1\,\mathrm{M}_{\odot}$) is consistent between all four fits. However, the difference lies at the low-mass end ($M < 1\,\mathrm{M}_{\odot}$). The prescription of the slope is different in each case, which is important for comparing stellar populations modelled with different IMFs.

1970s, the IMF was found to deviate from the single power-law profile, and segmented power-law profiles were preferred (i.e. Miller & Scalo, 1979; Kroupa, Tout & Gilmore, 1993). These profiles incorporate two segments in the power-law at the low mass end, shallower than the Salpeter slope, one at 0.08 $M_\odot$, and the other close to 1.0 $M_\odot$ (Kroupa, 2001). Alternatively, instead of a combination of power-law slopes, a lognormal distribution at the low mass end captures a very similar result (Chabrier, 2003). Here, the break is at $\sim 1.0\,M_\odot$, and the characteristic mass of the lognormal region is 0.2–0.3 $M_\odot$. These three IMF parameterisations are shown in Figure 1.4, which demonstrates the similarity between the Chabrier (2003) and Kroupa (2001) IMFs. Recent surveys with *Gaia* catalogues find close agreement with the Kroupa broken power-law (i.e. Sollima, 2019).

What does this mean for a stellar population?

There is no reason *a priori* for the IMF to be invariant in time or space. The IMF is a conditional probability whose form may depend on the metal abundance, gas density, turbulent velocity or other properties of the interstellar medium (Scalo, 1986). As the properties of the interstellar medium varies over the lifetime of a galaxy it follows that the IMF may also vary. However, within the MW, it seems that a single IMF can well match the disk, field, starburst clusters, globular clusters, and the galactic centre (e.g. Chabrier, 2003).

Throughout the Universe, the star-forming conditions may be significantly different from the MW. However the MW may represent a system in which the gas collapse conditions are close to uniform, and this causes the IMF to appear to be well-matched with a single description. However, other galaxies will have different environments where the gas and dust which collapsed to form stars may have significantly different metallicity, density or temperature.

The number density of dwarf stars is a key difference between the IMFs, see Figure 1.4. The dwarfs contribute only a small fraction of a population's luminosity but contribute significant mass. For a simple stellar population which is 10 Gyrs old, the ratio of M/L between the Salpeter and Kroupa (MW-like) IMFs is ~ 1.6. So for a luminosity

measurement, the mass is 60 per cent different. Therefore constraining the IMF is key to understanding galaxy evolution.

1.4 Investigating the initial mass function within unresolved populations

Resolved studies of galaxies beyond the local group are not possible, so the IMF must be inferred from the integrated light and/or gravitational mass tracers. Broadly, the observational techniques fall into two categories. The first method infers the stellar population via high signal-to-noise spectroscopy. The relative strength of dwarf and giant star gravity-sensitive absorption features are measured by fitting detailed stellar population synthesis templates. The second method measures the stellar population indirectly by comparing a stellar mass-to-light ratio (Υ) measured from stellar dynamics, strong gravitational lensing, or a combination of both, with a reference mass-to-light ratio ($\Upsilon_{\rm ref}$) from a fixed IMF stellar population synthesis model. The IMF mismatch parameter, α is defined as:

$$\alpha = \frac{\Upsilon}{\Upsilon_{\rm ref}} \tag{1.4.1}$$

where $\Upsilon_{\rm ref}$ is the stellar mass-to-light ratio for a model stellar population with a MW-like (Kroupa) IMF. Studies using both techniques have found evidence for an increasingly 'heavy' IMF (more mass per unit luminosity than a MW-like IMF model predicts) in the most massive ETGs (e.g. Treu et al., 2010; Cappellari et al., 2012; Conroy & van Dokkum, 2012b; La Barbera et al., 2013). In this section, I will examine these techniques.

1.4.1 Spectroscopic features

Individual dwarf stars are faint. However, the dwarf star fraction is encoded into the spectrum of a stellar population. The first attempt to investigate the relative abundance of

dwarf and giant stars used the Na D lines (Spinrad, 1962). In the twenty years that followed, additional dwarf or giant star spectral features were included in the analyses, such as Mgɪ, Caɪ, Caɪɪ, TiO, CN, CaH, MgH and the molecular FeH Wing-Ford band, (WFB), (Spinrad & Taylor, 1971; Carter et al., 1986; Couture & Hardy, 1993). Additional complications were found when separating the intrinsic dwarf-giant ratio effects from abundance effects, as both can impact the strength of gravity-sensitive features. The first robust constraints from stellar population models came in the early 2000s when high-quality stellar population synthesis models and data became available (Cenarro et al., 2003).

In the last 10 years stellar population synthesis modelling has developed significantly. Key to these developments are the improved resolution (<3 Å) and metallicity coverage Bruzual & Charlot (2003); Maraston (2005); Conroy et al. (2009). However, even with these models difficulties with some phases of stellar evolution remain. Some examples of these are the blue stragglers, the horizontal branch, the asymptotic giant branch, and the thermally pulsing asymptotic giant branch. Typically, these limitations occur because of a lack of spectral coverage of stars in the transitional phases, as there are few in the MW. However, as different models appear to measure consistent results, the measurements appear robust to these potential issues. (Spiniello et al., 2015).

The overall results from different models appear robust, however, including or excluding different spectral features seem to derive different final parameters. One example is that excluding Naɪ leads to a derived fit requiring a lighter IMF (e.g. a 3σ shift in Newman et al., 2017). Another is the FeH WFB in MaNGA data, which is inconsistent with several other absorption features, Hβ, Mgb, NaD, Naɪ, (Parikh et al., 2018). However, despite these inconsistencies, spectral analysis is a powerful tool for investigating a large number of ETGs in a self-consistent manner.

1.4.2 Stellar dynamics

Whereas spectral analysis directly probes features dependent on the stars, an alternative technique is to directly measure Υ. This is a proxy for the ratio of giant to dwarf stars,

assuming no high-mass variations, i.e. remnant-dominated IMFs. The dynamic modelling of stellar kinematics infers Υ using line-of-sight velocity dispersions. To simplify the modelling, a galaxy is assumed to be in a steady-state and have a spherical, axisymmetric, or triaxial shape. The gravitational potential is constrained and decoupled into stellar and dark matter, although a central supermassive black hole may be included (Cappellari, 2016). The line-of-sight velocity moments are measured radially across a galaxy to constrain the gravitational potential. Edge-on systems are preferred to limit inclination effects.

This technique has been applied to both integral field spectroscopy (Cappellari et al., 2006) and single fibre spectra (Graves & Faber, 2010). The preferred approach uses integral field spectroscopy, see Section 2.3, to exploit spatially resolved kinematics and resolve some of the degeneracies associated with the DM profile. The Jeans Anisotropic Multi-Gaussian Expansion (JAM) modelling method is frequently applied to IMF studies (Cappellari et al., 2012). The JAM method uses the equations from Jeans (1922) to describe the velocity moments in an assumed anisotropic system with a density derived from a Multi-Gaussian Expansion (for more details, see Cappellari, 2012). A series of oblate spheroids with Gaussian profiles are fit to the light profile of the galaxy, which are de-projected for inclination effects. The DM profile is incorporated as a gravitational potential and may take one of multiple functional forms. The measured stellar mass is compared to the light from photometry, to infer Υ, and then compared to $\Upsilon_{\rm ref}$. Typically, Υ is assumed to be constant, however, it may be varied with radius the modelling (Li et al., 2017; Oldham & Auger, 2018).

Stellar dynamics offer another route to measure the stellar mass and hence infer the IMF within a large sample of galaxies. Any bright galaxy which is spatially resolved by the selected instrument can be investigated. However the modelling requires many simplifying assumptions are required.

1.4.3 Gravitational strong-lensing

Using gravitational lensing to investigate the IMF is key to this thesis. This section presents the formalisms of lensing and will discuss the application of lensing to the IMF afterwards.

The idea of light bending due to gravity was first attributed to Isaac Newton in the early 1700s, and the first formal calculations were published in 1801 by Johann Georg von Soldner. Just over 100 years later, these calculations were repeated by Albert Einstein in the framework of general relativity and spacetime (GR), instead of classical mechanics. He considered the deflections of starlight around the Sun and concluded that the deflection was twice that predicted classically. The deflection angle is given by:

$$\alpha = \frac{4GM}{bc^2} \tag{1.4.2}$$

where b is the impact parameter (the distance of closest approach to the centre of the Sun), c is the speed of light, G is Newton‘s gravitational constant, and M is the mass of the lens. The equation was tested in 1919 by Eddington who measured the displacement of a background star during a solar eclipse when the position of the star could be measured accurately. Although the effect was small (the prediction from GR was ~ 1.75 arcsec), the measured deflection was 1.61 ± 0.30 arcsec (Dyson et al., 1920).

However, with such a small deflection and such a bright object, could more massive distant systems in the Universe have a larger effect? Fritz Zwicky suggested in his 1937 letter "Nebulae as Gravitational Lenses" (Zwicky, 1937) that galaxies or galaxy clusters could deflect light "by up to half a minute of arc". Hence for an alignment of a lens and a background source which forms multiple images, these images may form with sufficient separation and contrast to be observed.

The first gravitational lens was discovered 42 years later, when two quasars at $z = 1.41$ separated by 6 arcsecs with near-identical spectra were reported as either a gravitational lens or twin quasi-stellar objects (Walsh et al., 1979). This system was confirmed when a galaxy cluster was discovered at redshift 0.36, within which the BCG and cluster potential

form the lens (Young et al., 1980; Stockton, 1980). After the discovery, the number of known lenses increased to a few tens into the 1990s. Improved selection techniques and instruments has increased the current sample to a few hundred at present.

Depending on the strength of the lensing deflections, there are three main regimes.

Strong Lensing: This is the alignment of a massive foreground object (i.e. galaxy cluster/group/massive galaxy) which strongly distorts the light of one (or more) background sources to form multiple images of each. Gravitational strong lensing has a wide range of applications, from investigating the mass distribution of early-type galaxies (e.g. Treu & Koopmans, 2004; Kochanek et al., 2006), the IMF (e.g. Treu et al., 2010; Smith et al., 2015), the nature of dark matter, (e.g. Ritondale et al., 2019), to the expansion of the Universe, and constraining the Hubble constant (e.g. Chen et al., 2019).

Weak Lensing: Whenever there is a mass distribution between a source and an observer, the light profiles will be slightly distorted. These are not observable galaxy-to-galaxy, but instead are investigated statistically. Weak lensing is generally used to investigate the mass or DM in galaxy clusters (e.g. Clowe et al., 2006), but can also be used to investigate cosmological parameters (e.g. Hoekstra & Jain, 2008; Wang & Mukherjee, 2006).

Microlensing: The final case occurs on the smallest scales. Typically, microlensing requires an extremely compact source (i.e. point source) with a lens on the scale of a star or smaller. The extremely small lensing cross-section leads to deflections smaller than 1 milli-arcsec, and can lead to deviations in the flux-ratio within quasar strong lenses (e.g. Schechter & Wambsganss, 2002; Schechter et al., 2014). These magnifications can change on the timescale of years, to tens of years (Treu, 2010). This unique effect was exploited to investigate the nature of dark matter, as massive compact halo objects (MACHOs) could microlens stars within the Galaxy (Alcock et al., 1993).

1.4.3.1 Formalism of strong gravitational lensing

This section will explain the geometry of strong gravitational lensing and how the Einstein radius ($R_{\rm Ein}$) is defined. This is the aperture in which the total mass is robustly constrained.

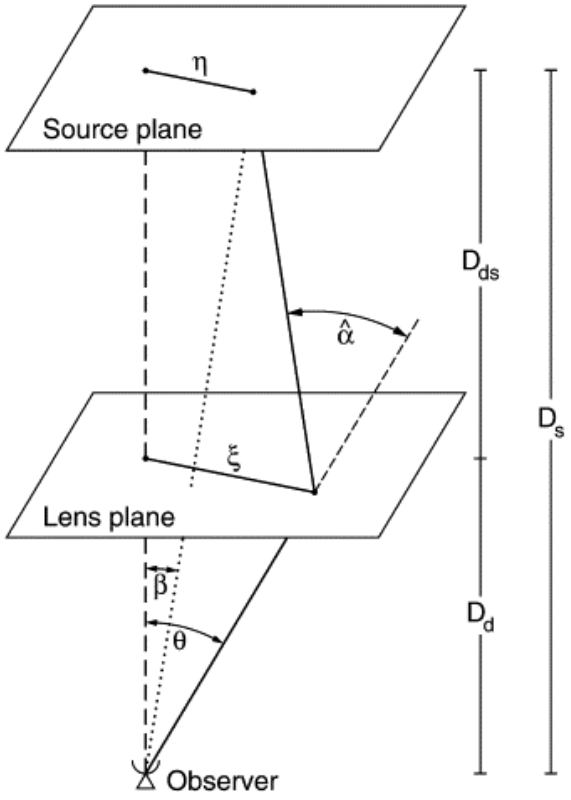

Figure 1.5: The geometry of a gravitational lens from Bartelmann & Schneider (2001). This shows the path of a light ray which passes from a source offset from the centre of the lens by η, and is deflected by the lens at a distance ξ and focused to the observer through an angle θ. The angular diameter distances D_d, D_s and D_{ds} are shown.

An example of gravitational lensing is shown in Figure 1.5. A single light ray originates from the source plane at angular diameter distance D_s, subtending an angle β to the observer. The light ray is deflected by a lens at angular diameter distance D_d through angle $\hat{\alpha}$. The deflection is considered for a thin lens with an impact parameter ξ, i.e. the lens is small compared to the distances between the observer, deflector and source. From simple geometry

$$\eta = \frac{D_s}{D_d}\xi - D_{ds}\hat{\alpha}(\xi). \tag{1.4.3}$$

This equation can be re-written in angular co-ordinates using the small angle approximation, $\sin(\theta) = \theta$, $\eta = D_s\beta$, and $\xi = D_d\theta$ which generates the lens equation:

$$\beta = \theta - \frac{D_{ds}}{D_s}\hat{\alpha}(D_d\theta) = \theta - \alpha. \tag{1.4.4}$$

This describes how the light ray originating at an angle β will instead be observed subtending the angle θ on the sky. The scaled deflection angle is defined as $\alpha = \frac{D_{ds}}{D_s}\hat{\alpha}\,(D_d\theta)$.

This equation is simplified further if the lens is assumed to be a mass-sheet (i.e. have a constant density), and in this case

$$\alpha(\theta) = \left[\frac{4\pi G\Sigma D_d D_{ds}}{c^2 D_s}\right]\theta = \left[\frac{\Sigma}{\Sigma_{crit}}\right]\theta. \tag{1.4.5}$$

Here, the critical density for lensing is defined as $\Sigma_{crit} = \frac{c^2 D_s}{4\pi G D_d D_{ds}}$, and the convergence, $\kappa(\theta) = \frac{\Sigma(D_d\theta)}{\Sigma_{crit}}$. This makes the deflection angle $\beta = (1\text{-}\kappa)\theta$. Therefore, when $\kappa = 1$ two or more parallel rays from the source plane will focus on the observer plane.

The limit for strong lensing to occur is when Σ exceeding Σ_{crit}. For $\kappa > 1$ multiple images may also form, by over-focussing.

For a circularly symmetric lens, the lens equation can be written as

$$\beta = \theta - \frac{4GM(\theta)D_{ds}}{c^2 D_s D_d}\frac{1}{\theta}, \tag{1.4.6}$$

which can be re-arranged to find $R_{\rm Ein}$. The case of $\beta = 0$ forms a perfect Einstein ring with,

$$R_{\rm Ein} = \left[\frac{4GM(\theta)D_{\rm ds}}{c^2 D_{\rm s} D_{\rm d}}\right]^{\frac{1}{2}} \tag{1.4.7}$$

For an axisymmetric (in 2D) lens, i.e. ETGs galaxies, the deflection angle becomes

$$\beta = (1 - \langle\kappa\rangle(\theta)\theta) \tag{1.4.8}$$

For an Einstein ring where $\beta = 0$, it requires $\langle\kappa\rangle(\theta) = 1$. Hence, for any lens, the average convergence inside $R_{\rm Ein}$ is unity, or alternatively, $R_{\rm Ein}$ is the radius at which the average enclosed convergence is unity. For lenses with ellipticity $\langle\kappa\rangle(\theta)$ is typically measured within a circular aperture.

1.4.3.2 Strong gravitational lensing for the IMF

Strong gravitational lensing measures the total mass within $R_{\rm Ein}$ to a high level of precision. The total mass, however, incorporates both stellar and dark matter. To investigate the IMF the stellar mass must be robustly determined. Therefore, the treatment to decouple the light and dark matter is key.

Currently, there are two main approaches to separate the luminous and dark matter within $R_{\rm Ein}$. The first is to incorporate stellar dynamics and stellar population synthesis models to infer the DM halo contribution. This technique relies on using a fixed relationship between the mass derived from stellar dynamics and the stellar mass (see equation 1, Auger et al., 2010). Including stellar dynamics incorporates into the analysis the assumptions listed in Section 1.4.2. For 'typical' lenses, with $\langle z\rangle \simeq 0.2$, the dark matter contribution to $M_{\rm Ein}$ is 40–75 per cent when assuming a Chabrier IMF. Even for a Salpeter IMF, the DM contributes up to 50 per cent of $M_{\rm Ein}$ (see Auger et al., 2009). Therefore, estimates of the stellar component of these systems are reliant on the dynamical modelling assumptions.

A second approach uses lensing alone to measure $M_{\rm Ein}$ and then applies a correction factor from simulated DM halos (Smith & Lucey, 2013). However, for this correction to be

reliable, the contribution from DM within $R_{\rm Ein}$ must be smaller than for the 'typical' lenses. Therefore, each lens must be selected to have preferable geometry to probe only the stellar dense core ($R_{\rm Ein} < 0.5 R_{\rm Eff}$). An example is the sample of low-redshift ($z < 0.1$) lenses, in which the contribution to $M_{\rm Ein}$ from dark matter is ~ 20 per cent (Smith et al., 2015).

The favourable geometry of a low-z lens relies on the angular size of $R_{\rm Ein}$ being a small fraction of the effective radius ($R_{\rm Eff}$). For a source at infinity, the angular size of $R_{\rm Ein}$ remains roughly constant with a varying lens redshift. However, the lens galaxy will have a larger angular $R_{\rm Eff}$ as the redshift decreases. Therefore, a lens with the same velocity dispersion, or mass, will, in physical terms, have a smaller $R_{\rm Ein}$ when situated at low-z, compared to the same lens, but more distant from the observer.

Strong gravitational lensing is an excellent probe of the IMF. The mass within $R_{\rm Ein}$ is very tightly constrained, to a precision of a few per cent in the best cases (Treu, 2010). The complication arises when separating the two components of the mass, which introduces some additional modelling uncertainty. However, in preferential cases decoupling the stellar and DM components can require very few assumptions.

1.5 Searching for strong gravitational lenses

In the preceding section, we presented three different techniques to investigate the IMF. The only criteria for targets of stellar dynamics or spectral analysis is a dataset of sufficient quality, so in principle, any galaxy can be investigated. Spectral analysis, in particular, requires very high S/N observations (~100s). In comparison, for a lensing analysis, the target must exhibit strong gravitational lensing, which is not a fundamental galaxy property and is intrinsically rare. These particular cases rely on the chance alignment of a background source within the lensing cross-section of a foreground galaxy.

The current census of galaxy-scale lenses was compiled using techniques that fall into two broad categories: those searching spatially within imaging, and those using single-fibre spectroscopy to detect background emission-line objects. Within imaging, the preferred

methods focus on identifying either elongated arcs (i.e. strong lensing challenge, Metcalf et al., 2019), or multiple sources with similar colour properties distinct from the foreground galaxies (Lemon et al., 2018, 2019; Lucey et al., 2018; Delchambre et al., 2019; Rusu et al., 2019). The second category yields lenses from spectral features distinct from the foreground galaxy in redshift space, in large spectroscopic surveys (e.g. SDSS). In most systems, the background source is detected in emission (e.g. SLACS, BELLS, Bolton et al., 2006; Brownstein et al., 2012). However, it is also possible to detect background absorption line systems (i.e. early-early lenses, Oldham et al., 2017a). The foreground lens galaxy is fit with a model spectrum, and then the residual is searched for higher-redshift residual features. Due to the small angular size of the individual fibres (e.g. 3 arcsec, SDSS), if a background source is detected, it is likely to lie within the multiply imaged region of the source plane.

For lens systems identified through either of the classical techniques, the discovery data are generally insufficient for a full analysis. Imaging only reveals the number, and fluxes of potential lensed images, but does not provide the redshifts which are required to confirm a single source of origin. Conversely, spectroscopy only confirms the redshift of a background object, but not the configuration. Therefore, neither of these are usually observationally efficient. Furthermore, the detection method biases any discovered lens systems. To detect within imaging alone, the lensed sources must be resolved against the foreground lens light. Therefore, the lensed images often have large angular separations (compared to the lens $R_{\rm Eff}$). Spectroscopic searches are limited by the fibre size. To detect an emission line, enough of the lensed image flux must be contained within a fibre, which may not be the case for highly asymmetric systems. (This issue increases with next generation single fibre surveys as the apertures are selected to target more distant galaxies.) Therefore, both of these techniques may fail to detect valid strong-lensing systems.

The advent of large field-of-view (FoV) integral field units (IFU) with sufficient angular and spectral resolution offers a third approach for lens discovery. IFU observations use spectral pixels to uncover background emission lines and have the spatial resolution to search simultaneously for redshift-matched, spatially separated images. Due to the large

FoV, the positions of lensed images are no longer limited to the small fibre aperture size regime. With the spectral resolution, fainter background sources may be discovered at the peak contrast between the lensed emission, and the foreground continuum (i.e. Smith et al., 2015; Smith, 2017). Some studies also use IFUs to create pseudo-narrowband images to search for arcs (Lee, 2017), or treating each spatial pixel as an independent fibre to search for background emission after a model spectrum is subtracted (Talbot et al., 2018). IFU data is an observationally efficient method to discover and analyse strong gravitational lenses.

1.6 The present state of the field

The IMF within the solar neighbourhood is well-defined. Star counts, and careful treatment of their completeness and biases, lead to a definition of an invariant IMF, as described by a Kroupa or Chabrier IMF, regardless of location or scale (see section 2, Bastian et al., 2010, and references therein).

However, as there is no clear reason for this invariance, one might suggest a search on the extragalactic scale for regions of extreme star formation. Such regions may seem an enticing prospect for deviating from the MW-like IMFs (Chabrier et al., 2014). From their formation histories, ETGs would appear to have undergone intense star formation episodes at the start of their lifetimes, when the universe was relatively young compared to the present-day, followed by an extended period of quiescence. Therefore, ETGs may represent a different population of stars than is observed in present day late-type galaxies. If different galaxies form stars from a different IMF, then this may have important implications for the understanding of galaxy evolution and estimates of fundamental properties such as stellar masses or chemical enrichment.

Each of the three IMF tracing techniques which have been applied to study ETGs were described in Section 1.4.

Using a small sample of 8 galaxies, the first full spectral fit used early-version stellar population models from Conroy & van Dokkum (2012a, hereafter CvD models). The

galaxy spectra required a stellar population with an increased number of dwarf stars compared to the MW (van Dokkum & Conroy, 2010). Although the exact fitting techniques vary slightly, generally in the treatment of the low-mass limit, further studies with the CvD models all require a 'heavier' than Salpeter IMF (low-mass slopes x in the range 2–3) to fit massive, $\sigma \simeq 300\,\mathrm{kms}^{-1}$, ETGs (Spiniello et al., 2012; Smith et al., 2012; Conroy & van Dokkum, 2012b; Newman et al., 2017). Furthermore, the same studies find a trend with increasing galaxy mass for increasingly dwarf-enriched populations.

Comparable results are found with different stellar libraries, (i.e. E-MILES Ferreras et al., 2013; La Barbera et al., 2013). In particular, La Barbera et al. (2013) obtain results consistent with an IMF with a low-mass slope of $x = 2.8$–3.0. For a similar set of SDSS ETG spectra, Newman et al. (2017) found a considerably shallower low-mass slope ($x \simeq 1.8$), but still inconsistent with a MW-like IMF. Therefore, spectroscopy, whether fitting to individual features, or a full spectrum, requires a varying IMF to describe the whole population of ETGs, see Figure 1.6 for the results from Conroy & van Dokkum (2012b).

The results from stellar dynamics typically agree with the spectral analysis. The first dynamical analysis investigated the M/L ratio for 25 ETGs using the Jeans equations and found a tight relation between the dynamical masses and the inferred Υ_{ref} from spectral analysis (SAURON Cappellari et al., 2006). This suggests only a small IMF variation from galaxy to galaxy; however, there was no explicit treatment for a DM halo. In contrast, Thomas et al. (2011) used long-slit spectroscopy and an explicit model for the DM halo. The inferred IMF varied from Salpeter ($\alpha \simeq 1.5$) at $\sigma = 200\,\mathrm{kms}^{-1}$ to 'heavyweight' ($\alpha \simeq 2.0$) at $\sigma = 300\,\mathrm{kms}^{-1}$ (see figure 8, Thomas et al., 2011).

The first large sample of ETGs (260 galaxies) used to probe the IMF with stellar dynamics was compiled in the ATLAS^{3D} survey (Cappellari et al., 2011). Using the JAM modelling technique described in Section 1.4.2, Cappellari et al. (2012) found that the IMF varied from MW-like at $\sigma = 100\,\mathrm{kms}^{-1}$ to Salpeter-like $\sigma = 300\,\mathrm{kms}^{-1}$, (see Figure 1.6). Therefore, stellar dynamics, alike to spectral analysis, requires an increasingly 'heavy' IMF with larger velocity dispersion. Although the results between stellar dynamics and spectral

analysis agree, on a case-by-case basis, Smith (2014) found that aperture effects may lead to inconsistent measurements.

Analysis with both single-fibre spectroscopy and stellar dynamics assumes a constant Υ profile across a galaxy. There is no reason *a priori* for this to be true. In fact, given the two-stage formation model for an ETG, Υ may vary with radius; which can also be inferred as an IMF gradient. With spatially-resolved spectroscopy, there has been evidence for (i.e. Martín-Navarro et al., 2015; La Barbera et al., 2016; van Dokkum et al., 2017; Sarzi et al., 2018; La Barbera et al., 2019) and against (i.e. Vaughan et al., 2018; Alton et al., 2018; Zieleniewski et al., 2017) IMF variations. Generally, in larger samples, stronger gradients are found with more massive ETGs. A variable Υ gradient can be incorporated when modelling stellar dynamics. In two systems, M87 (Oldham & Auger, 2018) and ESO325–G004, (Collett et al., 2018), steep gradients are found, with increasingly 'heavyweight' IMFs in the cores ($< 0.2\,R_{\rm Eff}$). Due to the different apertures used to estimate the spectral fits and dynamical masses, a Υ gradient could have a large impact on the derived stellar mass (see Bernardi et al., 2018).

The final technique is strong gravitational lensing. The SLACS lenses were discovered from single-fibre SDSS spectra by fitting a model for the foreground ETG and searching the residual for background emission line objects (Bolton et al., 2006). Promising targets were followed up with a *HST* snapshot survey to confirm the lensing configurations. The lenses typically have a $\langle z \rangle = 0.2$, and the stellar mass is measured using a two-part model combining lensing and dynamics (Treu et al., 2010). The measured α parameter favours a systematic variation in the IMF with velocity dispersion, and these results, re-scaled to a reference Kroupa IMF, are shown in Figure 1.6. The inconsistency with a MW-like IMF is also robust with variations in the parametrisation of the DM halo (Auger et al., 2010). The results from ATLAS3D and the SLACS lenses are mostly consistent and indicate a continuing trend (Posacki et al., 2015).

All of the currently described α parameters show variation with velocity dispersion. However, a low-redshift ($z = 0.034$), massive ($\sigma = 312\,\mathrm{kms}^{-1}$) ETG strong lens, which was discovered serendipitously within *HST* data by Smith et al. (2005), favoured an α parameter

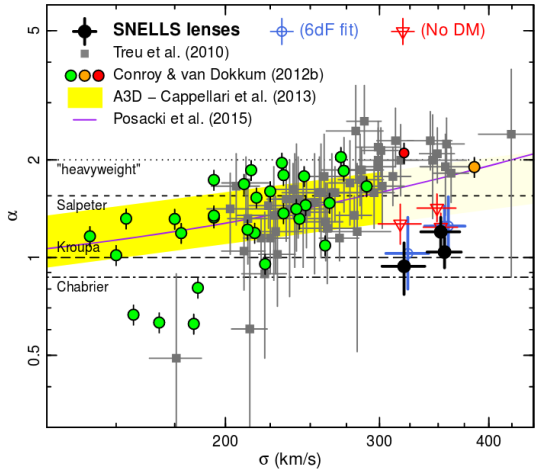

Figure 1.6: The mass-excess parameter, α (with Kroupa $\alpha = 1$), as a function of velocity dispersion within ETGs. (Taken from figure 7, Smith et al., 2015) The measurements from the SNELLS lenses are shown with three DM prescriptions; lensing and DM, a dynamical DM estimate and no DM. The results from the SLACS lenses (Treu et al., 2010), spectral analysis (Conroy & van Dokkum, 2012b) and ATLAS^{3D} stellar dynamics (Cappellari et al., 2012) are shown. The SNELLS lenses are clearly separated from the suggested trend from the other techniques.

consistent with a MW-like IMF (Smith & Lucey, 2013). A campaign to discover similar lenses uncovered two new systems, SNL-1 and SNL-2, using the ESO/VLT SINFONI instrument (Smith et al., 2015). The stellar masses of both systems were also consistent with MW-like IMFs using strong-lensing analysis and DM masses estimated from simulated halos (see Figure 1.6). The $R_{\rm Ein}$ is less than one half $R_{\rm Eff}$ in each case. Even if all of the mass within $R_{\rm Ein}$ is attributed to the stars, i.e. no DM, these systems remain inconsistent with a 'heavyweight' IMF.

All three of the discussed IMF techniques can be applied to the low-z SNELLS lenses, making them a unique test sample. Newman et al. (2017) analysed the three systems, with each technique independently, as well as combining dynamics and lensing. For two out of three SNELLS lenses, there is an inconsistency between the results from the spectral and lensing analyses. The best fit stellar population has a mass greater than the total mass within $R_{\rm Ein}$, for a standard IMF parametrisation, unless NaI is removed from the fit (see figure 4, Newman et al., 2017).

The SNELLS systems are 3 σ deviated from the SLACS measured α at the same velocity

dispersion. Each system has a $R_{\rm Ein}$ which probes a small fraction of the $R_{\rm Eff}$ ($< 0.5 R_{\rm Eff}$), and the dark matter correction is sufficiently small (~ 20 per cent) that the tension remains even when the total lensing mass is attributed to the stellar component.

1.7 The next step

Many of the current studies investigating the IMF focus on spectroscopy or stellar dynamics using different tracers or models. However, Sonnenfeld et al. (2018) re-analysed the SLACS lenses using a set of weak lensing measurements for a set of comparable galaxies to constrain the stellar mass. When a radially dependent IMF is assumed the modelling suggested that the SLACS analysis overestimated the stellar mass, and hence overestimated α.

A preferable way to investigate the population of strong-lensing ETGs is to continue to work with the low-z lenses. Not only do they provide a 'golden sample' by which all three IMF probing techniques can be compared, they also have comparably lower DM masses within their respective $R_{\rm Ein}$, and hence provide the most robust measurements of the stellar mass. However, the current low-z sample is beset by two important issues. First, the lensing analyses for two of the three (SNL-1 and SNL-2) systems are constrained only from low-resolution SINFONI data, and the ground-based shallow 2MASS photometry. Secondly, there are only three. From such a small sample the intrinsic distribution of α for the population cannot be rigorously determined.

The thesis will address the following key questions:

- Are the SNELLS lenses robust against improved lens modelling and the inspection of higher-resolution photometry?
- Can the SNELLS search techniques be applied other IFUs successfully?
- Are the three currently known SNELLS lenses outliers of the intrinsic population?
- Is the IMF a universal quantity?

1.8 Thesis outline

This thesis is divided into two parts: an update to the previously known low-z strong-lenses SNL-1 and SNL-2 from SNELLS, and the effort to use MUSE on ESO/VLT to discover new low-z strong-lenses. Both cases exploit low-z systems to constrain the stellar mass-to-light ratios. Hence the IMF is inferred.

- **Chapter 2:** In this chapter, I introduce the two gravitational lensing codes, GRAVLENS (Keeton, 2001) and PYAUTOLENS (Nightingale et al., 2017), which are used for all of the lensing analysis. I also briefly introduce integral field spectroscopy. I give some instrument specifics for the IFU MUSE, which is used to observe candidate gravitational strong lenses in Chapter 4 onwards.

- **Chapter 3:** In this chapter, I describe the observations and analysis of SNL-1 and SNL-2 from the SNELLS survey. The lensing analysis uses *Hubble Space Telescope* data and incorporates the lensed image flux ratios. This ratio is used to constrain the external shear for SNL-1, and the mass of the companion galaxy for SNL-2. From the analysis, the mass-excess parameter is measured and compared to the previous results SNELLS.

- **Chapter 4:** In this chapter, I introduce the MNELLS survey, a MUSE-based lens search based on the SNELLS target selection. I also undergo a complimentary search of data from MUSE archives. Each IFU observation is searched for distant emission-line objects which may be multiply imaged. From the detected sources several systems are identified as candidates for analysis. The selected galaxies are either singly imaged but close-projected systems (those with one candidate lensed image projected within 6 arcsec), or multiply imaged candidate lenses.

- **Chapter 5:** In this chapter, I investigate the three cluster-scale multiply imaged lenses, and the nine singly imaged but close-projected systems identified in Chapter 4. I constrain a probability distribution on the mass-excess parameter for each singly

imaged system, and infer Υ for two cluster-scale lenses. I measure the detection threshold of the MNELLS survey, and suggest possible adaptations for future similar surveys.

- **Chapter 6:** In this chapter, I present the newly discovered strong lens J0403-0239. First, the lens is analysed using the MUSE data assuming an old stellar population to measure the mass-excess parameter. Then I perform a more rigorous analysis with *HST* imaging and ESO/VLT FORS2 spectroscopic data. The wavelength range of FORS2 covers key spectral features sensitive to recent star formation to robustly determine the age of the stellar population. The higher resolution *HST* data enables a detailed lensing analysis with PYAUTOLENS.

- **Chapter 7:** In this chapter, I characterize the IMF distribution within massive ($\sigma \simeq 300\,\mathrm{kms}^{-1}$) ETGs. I combine the four confirmed low-z lenses with the nine singly imaged but close-projected systems analysed in Chapter 5, and two previously analysed by Smith et al. (2018), SNL-4, and MaNGA target J0728+4005. Assuming a lognormal distribution I derive the intrinsic mean and scatter of the $\sigma \simeq 300\,\mathrm{kms}^{-1}$ ETG population.

- **Chapter 8:** In this chapter, I summarise the work presented in this thesis. I suggest some continuation projects to expand the scope of this work, and describe some of the future surveys which will discover new low-z strong-lensing ETGs.

Chapter 3 consists of published work Collier et al. (2018a). Chapters 4, 5 and 7 present work published in Collier et al. (2020). Chapter 6 comprises a mix of published work, Collier et al. (2018b), and new unpublished analysis.

CHAPTER 2

Instruments and Tools

2.1 Preamble

Strong gravitational lensing is a key technique for investigating the stellar initial mass function (IMF) within early-type galaxies (ETG). For each system, the IMF is inferred by measuring the mass-excess parameter, α, which is the stellar mass-to-light ratio (Υ) compared to a reference mass-to-light ratio ($\Upsilon_{\rm ref}$). The reference model is a stellar population synthesis model assuming a fixed, MW-like, IMF for a single starburst which has evolved passively from formation to the observed redshift. The mass within $R_{\rm Ein}$ is measured using a parametric or non-parametric mass profile fit to the lensing configuration. The two lensing codes used in the forthcoming analysis, GRAVLENS, and PYAUTOLENS, and the preferred mass profiles are introduced in Sections 2.2.1 and 2.2.2.

Two of the three known low-z lenses were discovered using the SINFONI integral field spectrograph (Eisenhauer et al., 2003). However, other instruments with comparable or improved wavelength coverage and resolution are now available. Section 2.3 introduces integral field spectroscopy (IFS) and discusses the different instrument designs currently in use. Data from MUSE (Bacon et al., 2014) will form the basis of several chapters, and so specifics for this instrument are detailed in Section 2.3.2.

2.2 Gravitational lensing codes

Gravitational lensing robustly probes the mass within $R_{\rm Ein}$, making it a powerful technique for investigating the IMF within ETGs. Lensing analysis optimizes a mass model to fit the observed parameters. There are numerous different publicly available codes which will perform the lensing calculations, and so the selection is dependent on the target parameter(s) and the data available.

Precisely constraining the mass within $R_{\rm Ein}$requires two components. First is access to high-quality data to accurately measure the lensed image positions (i.e. optical/NIR imaging with *HST*, Lehár et al., 2000). Second is flexibility in the mass models to include external or internal complexity. To the first order, this would be the ellipticity of the lens (Keeton, Kochanek & Seljak, 1997). However, there may be gravitational effects from substructure within the galaxy (i.e. Mao & Schneider, 1998; Vegetti & Koopmans, 2009), or the effects from nearby objects or line-of-sight structures, (i.e. Keeton & Kochanek, 1997; Witt & Mao, 1997; Evans & Witt, 2003). These are generally approximated with an external shear.

The simplest route to estimating the mass within $R_{\rm Ein}$ is to approximate the lens as spherically symmetric, with $R_{\rm Ein}$ equal to the half-image separation. Re-arranging equation 1.4.7;

$$M_{\rm Ein} = 1.23 \times 10^{10} \left(\frac{R_{\rm Ein}}{1\,\mathrm{arcsec}}\right)^2 \frac{D}{100\,\mathrm{Mpc}} M_{\odot} \tag{2.2.1}$$

where D is $\dfrac{D_d D_s}{D_{ds}}$, which is the angular diameter distance to the lens multiplied by that to the source divided by the angular diameter distance between the lens and source. However, this omits any ellipticity in the lens which will impact the position of the lensed images, and the relative magnification.

Although there are a broad range of parametric and non-parametric lensing codes, for the analysis presented here, we select GRAVLENS (Keeton, 2001) and PYAUTOLENS (Nightingale et al., 2017).

2.2.1 Gravlens

The package referred to as GRAVLENS throughout this work contains two applications. The *gravlens* application performs basic lensing calculations with an extensive range of circular and elliptical mass models. The second application, *lensmodel*, adds the functionality to fit a mass profile to an observed system.

lensmodel is designed to fit a mass model to the observational constraints. For point-like lensed images, the constraints are image positions, relative fluxes, and/or time delays. For extended images the fitting is optimised for efficient computation and hence uses either 'ring fitting' for Einstein rings, or 'curve fitting' for arcs in which the images are typically smoothed (see Kochanek et al., 2001, for a more detailed explanation). Although *lensmodel* is the application, the package is referred to as GRAVLENS hereafter.

GRAVLENS has been available for almost twenty years and has been applied to investigate a wide range of science. The most frequently analysed systems are galaxy-scale lenses with point-like sources. Some examples are: measuring the accretion disk size for microlensed quasars (i.e. Morgan et al., 2010; Blackburne et al., 2011), attempting to measure the abundance of satellite halos in lensing galaxies (i.e. Dalal & Kochanek, 2002), or measuring gravitational lens time delays (i.e. Fassnacht et al., 2002; Kochanek, 2006).

Typical massive ETGs are well modelled with isothermal mass profiles (Rusin et al., 2003; Koopmans et al., 2006; Barnabè et al., 2011). However these mass models, in general, require a shear term to account for any additional structure which is not replicated with a single, smooth profile (Keeton et al., 1997; Witt & Mao, 1997). The approximation for an isothermal lens in GRAVLENS uses an elliptical power law profile. This is defined as;

$$\kappa = \frac{1}{2}(b')^{2-\alpha}[(s')^2 + \zeta^2]^{(\alpha/2-1)}. \tag{2.2.2}$$

Here, κ is the mass density as a function of elliptical radius ζ, where $\zeta = [(1\text{-}\epsilon)x^2 + (1+\epsilon)y^2]^{1/2}$ and ϵ is related to the axis ratio (q) by $q^2 = (1\text{-}\epsilon)/(1+\epsilon)$. The other parameters are; b' which is the deflector strength, and s' is a central core in the mass profile. α is set to 1 for an

isothermal profile.

When using a singular isothermal ellipsoid (SIE) model the ellipticity and position angle can be fixed to a fitted light profile from GALFIT (Peng et al., 2010) if the stars are assumed to dominate the mass. (A singular isothermal sphere is fixed at an ellipticity of zero.) The remaining parameters which are optimised during the modelling are $R_{\rm Ein}$and the shear amplitude and its position angle.

In GRAVLENS the mass profile is optimized using a least-squares fitting method. The χ^2 is calculated by comparing the observed lensed-image positions to the best fit model (if more constraints are provided, these will be incorporated). In a doubly imaged system, if only the image positions are used as constraints, there is a degeneracy between the lens mass and the external shear amplitude. However, the magnification at a given x,y position is not fixed when the shear and lens mass are varied. Hence, using a well constrained image flux ratio, time delay or relative image size will break the degeneracy between the models.

An example of fitting to a lens system with two point source images is shown in Figure 2.1. The accuracy of the recreated image positions improves with the addition of ellipticity to the mass profile. For the top two rows, the external shear (moving from the first to second column) acts along the lensed image axis and 'stretches' the caustics. Although the image positions are well matched in either column, the image fluxes require a shear amplitude in order to be reproduced.

The third row shows a mass-follows-light (MFL) profile. Within this thesis, the low-z lenses $R_{\rm Ein}$ probes the central, stellar dense core. As the total mass is dominated by the stars, the mass distribution is assumed to closely follow the light profile. With this assumption, we can take into account any non-uniformality in the galaxy profile with an MFL profile, instead of parameterizing the lens potential. For this particular lens configuration, the MFL profile captures the additional complexity of the system which was fit as an external shear in the SIE case, see Figure 2.1.

Converting from a broad-band image of a galaxy to a MFL profile is straightforward. The data is converted from counts into luminosity, and hence, via an assumed constant M/L,

converted to a mass surface density (Σ). The critical density for lensing relates Σ to a lensing deflection. This has a dependence on the geometry of the system:

$$\Sigma_{\rm crit} = \frac{c^2 D_{\rm s}}{4\pi G D_{\rm ds} D_{\rm d}} \tag{2.2.3}$$

where $D_{\rm d}$, $D_{\rm s}$ and $D_{\rm ds}$ are the angular diameter distances to the lens, source and between the lens and source respectively.

The ratio of Σ over $\Sigma_{\rm crit}$ is the lensing convergence (κ), and $R_{\rm Ein}$ is defined as the radius at which the mean enclosed κ is equal to 1 (See Section 2.2.1). The only slight non triviality is that this is a pixelised grid, and hence the resolution must be sufficient to resolve the steep inner light profile.

For a MFL profile in GRAVLENS the optimizable parameters are a scaling of the input profile, and the shear amplitude and position angle (KAP2LENS is the input command). The scaling factor is the best fit constant M/L for the lens system.

For my analysis, the mass within $R_{\rm Ein}$ is extracted by outputting the best fit solution as a κ map. Using $\Sigma_{\rm crit}$, the map is converted to a surface mass density which is summed within an aperture equal to $R_{\rm Ein}$.

The GRAVLENS code is relatively simple to use, and can quickly model lens systems for various mass profiles when point-like images are assumed. The software optimises the fit with a least-squares fitting method which preferentially weights the image positions over other constraints.

2.2.2 PyAutoLens

The second lensing software which will be used in this thesis is AUTOLENS (Nightingale et al., 2017). Throughout I will refer to PYAUTOLENS, as this is the python ported version of the original fortran AUTOLENS code. PYAUTOLENS is specialized to decompose the internal mass distribution of galaxies (Nightingale et al., 2019), and to automate the lens modelling

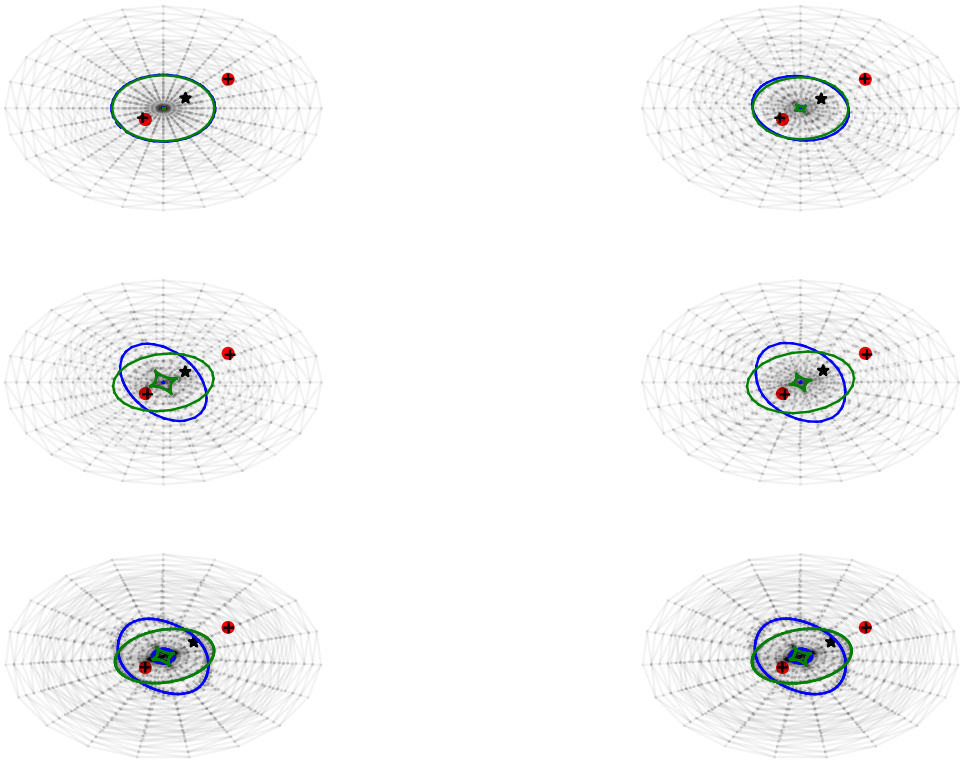

Figure 2.1: Output best fit mass models from GRAVLENS for SIS, SIE and kappa mass profiles. The caustic and critical lines are shown in green and blue respectively, and the image positions used to optimise the models are shown in red. The best fit source position is shown with a black star, and the recreated image positions are shown with a black cross. The left column has a fixed zero external shear, and the right column allows the external shear to be fit in the modelling.

for large samples of strong-lenses. PYTAUTOLENS has also been used to measure the $R_{\rm Ein}$ and $M_{\rm Ein}$ of individual galaxy-scale lenses (Smith et al., 2020).

PYAUTOLENS is designed to exploit the information offered by extended lensed images in a fully automated way. The input is a broad-band image, and PYAUTOLENS then fully fits all components of the lens light and mass profiles along with the source light profile. To carry out this more complex analysis the lensed images must be detected, and so deep, high-resolution imaging (e.g. *HST*) is required.

In contrast to many alternative techniques PYAUTOLENS fits the galaxy's light as part of the process, in addition to reconstructing the source galaxy and the lens mass profile. The light-profile fitting can be complex with multi-component models available. By modelling the lens and source light simultaneously, the observed light profile can be decomposed into the two components to a higher level of accuracy. (Typically the source must be 'masked out' when the lens light is fitted.) Additional information which may have previously been lost, such as the central image, or faint radial arcs from the lensed images, can then further constrain the mass-profile. A Bayesian model comparison is used to compare the likelihoods of features within the residuals of the light profile models to find the best fit solution (following the framework of Suyu et al., 2006).

In addition to the more standard mass profiles (i.e. isothermal), PYAUTOLENS contains the flexibility to decompose the light and dark matter purely from lensing. This uses a MFL model, assuming that the stellar mass is traced by the lens light, and hence the mass profiles deviation from the light is attributed to the dark matter component. Therefore, by fitting both a dark matter mass profile and the stellar mass profile, the stellar mass-to-light ratio can be directly measured.

More specifically to this thesis, there are a number of pre-designed pipelines in the PYAUTOLENS suite. The most suitable pipelines for ETGs are the 'lens Sérsic, SIE, source Sérsic' or the 'lens Sérsic, SIE, source inversion' which are the selected profiles for the lens light, lens mass and source light profile respectively. (A source inversion ray traces the image pixels onto the source plane to recreate the source light profile.) These are

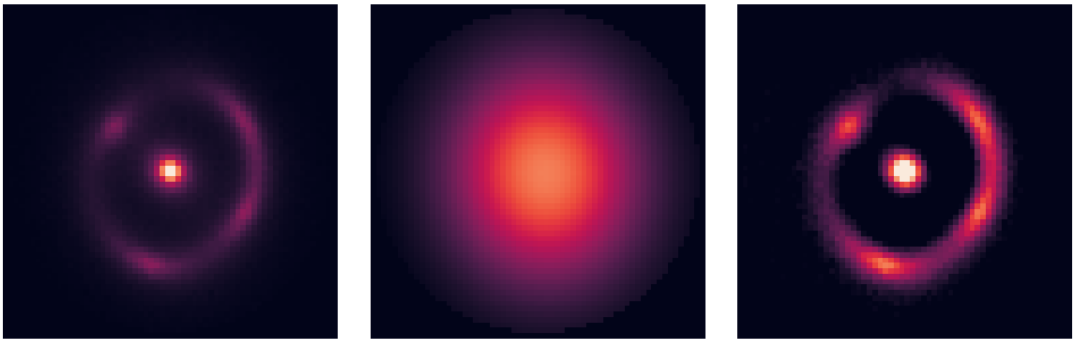

Figure 2.2: An example of phase one in the PYAUTOLENS pipeline, the initial light profile fitting. In the left panel, a simulated gravitational strong lens with a central lens galaxy at $z = 0.5$, and a near complete Einstein ring for a background source at $z = 1.0$. The second panel contains the initial simple fit for the light profile of the lens. In the right panel is the residual. At this stage the lens light residual is large, as the source was not masked.

relatively simple pipelines, however they provide all of the fits required for analysing M_{Ein} whilst making use of the information from an extended source.

The pipelines are broken down into phases. Each phase forms a different part of the fitting process. In the simplest pipeline (lens Sérsic, SIE, source Sérsic), the fit is performed in three 'phases'. For the initialization, PYAUTOLENS requires the image data, the point-spread-function (PSF) of the imaging, and a noise map.

In the first phase, the lens light profile is fit with a Sérsic, and priors are placed on the galaxy x,y position. An example of the outputs are shown in Figure 2.2. The fit at this stage leaves a large residual, with the fitted light profile appearing to have a shallower profile due to the lensed image light.

In the second phase, the initial estimation of the galaxies mass profile and the source galaxies light is fit. The centre of the lens mass profile is assumed to match the centre of the Sérsic profile from phase one. PYAUTOLENS then fits for a Sérsic background source and ray traces through the mass profile to recreate the extended images. The lens light profile is not changed, and hence the middle left panel of Figure 2.3, matches the model shown after phase one. However now the source light profile is mapped to a model of the partial Einstein ring, shown in the middle right panel, leading to a residual with most of

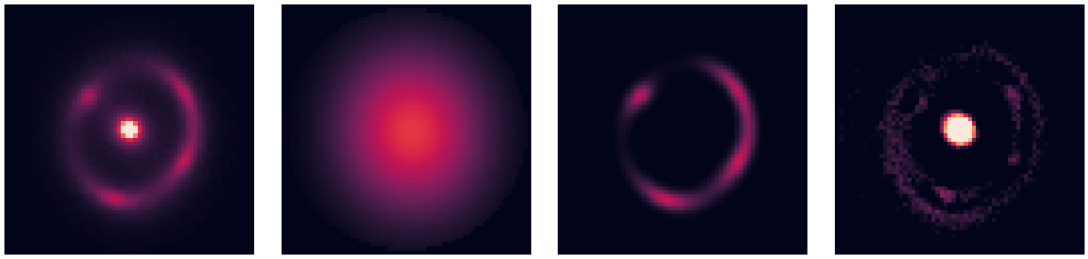

Figure 2.3: Panels to show the phase two of the PYAUTOLENS pipeline, the initial fitting of the lens mass profile, and source light profile. The left panel is the input model, and the middle left panel is the initial fit for the lens profile. The middle right panel is the preliminary fit for the source profile, displayed on the image plane, given the initial fit to the lens mass model. The right panel shows the residual which is still contaminated by the lens.

the source light removed, shown in the right panel.

In the third phase, the earlier fits from phase one and two initialize a fit to all components simultaneously. This provides the final fit for the lens system, shown in Figure 2.4. The lens light residual is less than one per cent, as the lens, and lensed images have been accurately decomposed as two components. Due to the change in lens light, the source model becomes attributed with more light, and hence the residual is also minimized compared to phase two. From this final fit, M_{Ein} is measured, along with other properties.

For a source inversion, there is a fourth and fifth phase in which the lensed image light is ray traced onto the source plane. In the fourth phase the fit is initialized and then in the fifth the final best fit is found. The inversion is carried out with an adaptive meshgrid in order to preferentially sample the position of the source at higher resolution. This final output can be used to infer morphological properties of the background lensed source, as shown in Figure 2.5. The source was originally a Sérsic, and hence the reconstruction reveals the same general structure which is expected.

2.2.3 Comparison

The decision for which lensing code to use for a given situation is based on the complexity of the analysis.

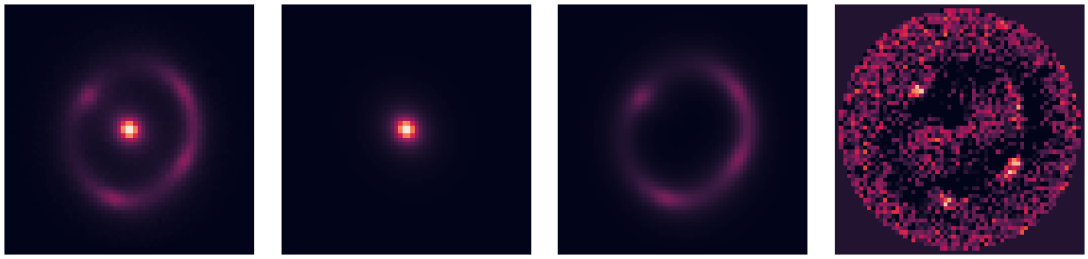

Figure 2.4: Panels to show the phase three of the PYAUTOLENS pipeline, in which phase one and two are used to initialise the fitting process for the entire lens system. Described left to right. The first panel is the input simulated lens. The second panel is the best fit to the lens light, which is now more compact. The third panel shows the best fit for the source on the image plane, mapped through the mass model. And the fourth panel is the residual from the best fit components. This is now significantly improved from phase one or two, although a few structures can be seen in the residual at the 1 per cent level.

GRAVLENS offers a tool that is versatile and easily adaptable to simple systems when the user wishes to describe a range of inputs and optimize for each. For a compact background source which lenses to point-like images, GRAVLENS is quicker, and requires no detailed lens light profile. However the software lacks application to incorporate the fitting of the galaxy's light. This must instead be a user input, which therefore must be carried out with additional software. Extended sources are also not dealt with in a complete sense.

For much of the work in this thesis GRAVLENS is preferred over PYAUTOLENS. There are two reasons behind this choice. First, at the beginning of this work, PYAUTOLENS was not publicly released, and hence was not available for the analysis. Second, is that much of my analysis does not require the complex decomposition, and as such the image positions are enough to constrain the systems. In fact, much of the broad-band imaging used in this thesis are fairly shallow, and have a large PSF (~1–3 arcsec) (2MASS, Pan-STARRS1 and VISTA), and hence the faint lensed images are below the detection threshold, or smoothed into the light profile of the lens. Indeed, modelling systems in which the lens has not been confirmed with high resolution data, or only a single image is present, or mock systems different to the observations, is far simpler computationally for the GRAVLENS software. However, for galaxies with high-resolution data, in which the lensed images are detected

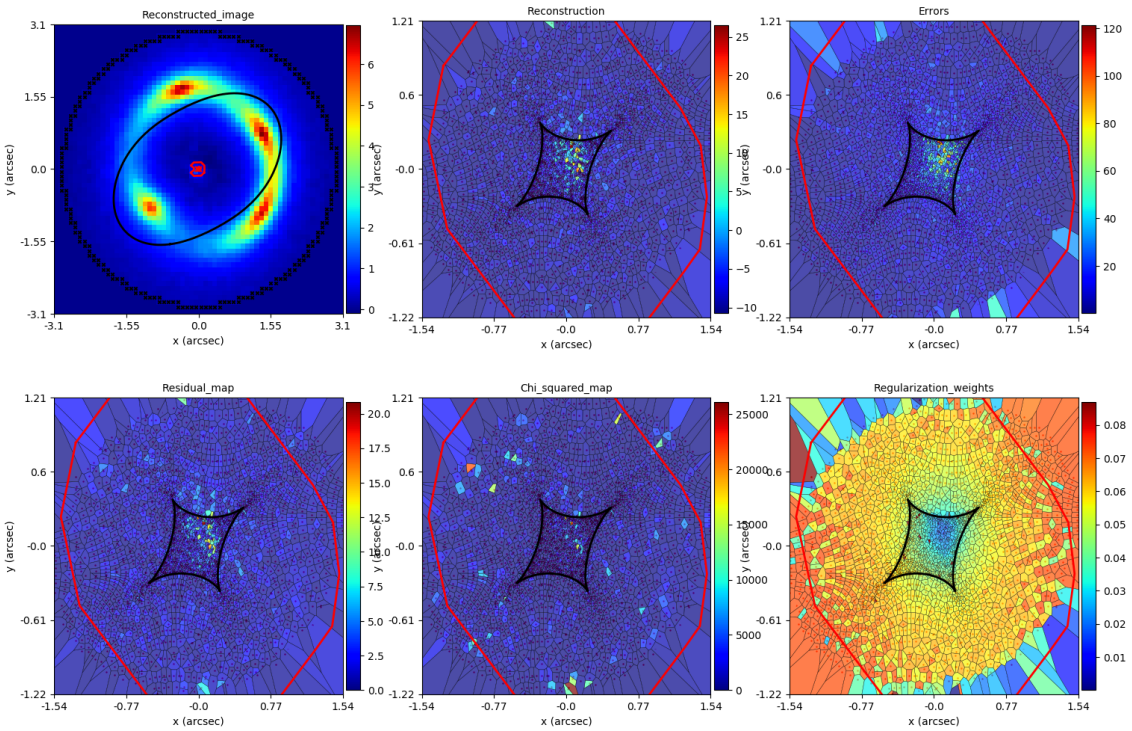

Figure 2.5: The PYAUTOLENS output for a lensed image light inversion. This maps the light from the images back to the source plane using the best fit mass model. Moving from left to right, top to bottom, the first panel shows the mass model critical lines in black, with the source position in red. The Einstein ring is plainly visible with the lens having been subtracted. The second panel shows the reconstruction of the source, having mapped the image light to the source plane. The caustic is shown in black, and the source is mapped as extended and with an apparent ellipticity. The uncertainty on the mapping is shown in panel three. The lower panels show the source plane mapped image plane residuals, the chi-squared map which suggests a good fit, and then the regularization weights.

and extended, the more complex analysis offered by PYAUTOLENS is preferable.

Chapters 3, 4, 6 and 7 all make use of GRAVLENS. However, after the acquisition of *HST* data, Chapter 6 will also make use of PYAUTOLENS.

2.3 Integral field spectroscopy

Chapters 4, 5 and 6 use Integral Field Spectroscopy (IFS) to detect and characterise background emission line objects. Generally the strongest emission lines are the [OII]λ3726,3729 doublet, [OIII]4959 Å,5007 Å, Hβ 4861 Åand Hα 6562 Å. I will now briefly outline some salient features of an Integral Field Unit (IFU).

2.3.1 Integral field units

Integral Field Spectroscopy (IFS) is a observational tool to obtain a 3D image of a galaxy with a single observation. The instrument resolves spatially, with a spectrum of an object at each position. The output from such an instrument is a 3-dimensional datacube; there is the spectroscopic λ direction and then two spatial dimensions (x,y in the datacube). An example of this is shown in Figure 2.6, with a marked wavelength range. If the wavelength resolution of the IFS instrument is high enough, individual emission lines can be isolated and analysed.

There are two key components of an integral field spectrograph. The first is the field splitter, which collects the light and breaks down the focal plane into many smaller segments. The second is a spectrograph which disperses the light onto a detector. The three most common field splitting designs are shown in Figure 2.7.

The first IFU, used lenslets to break up the object with an array of micro-lenses. The output of each element is then dispersed onto a detector. The system is relatively simple, and the throughput is high. However the wavelength range must be small to avoid different spectra overlapping, and this leads to inefficient use of the CCD. Examples of these IFUs

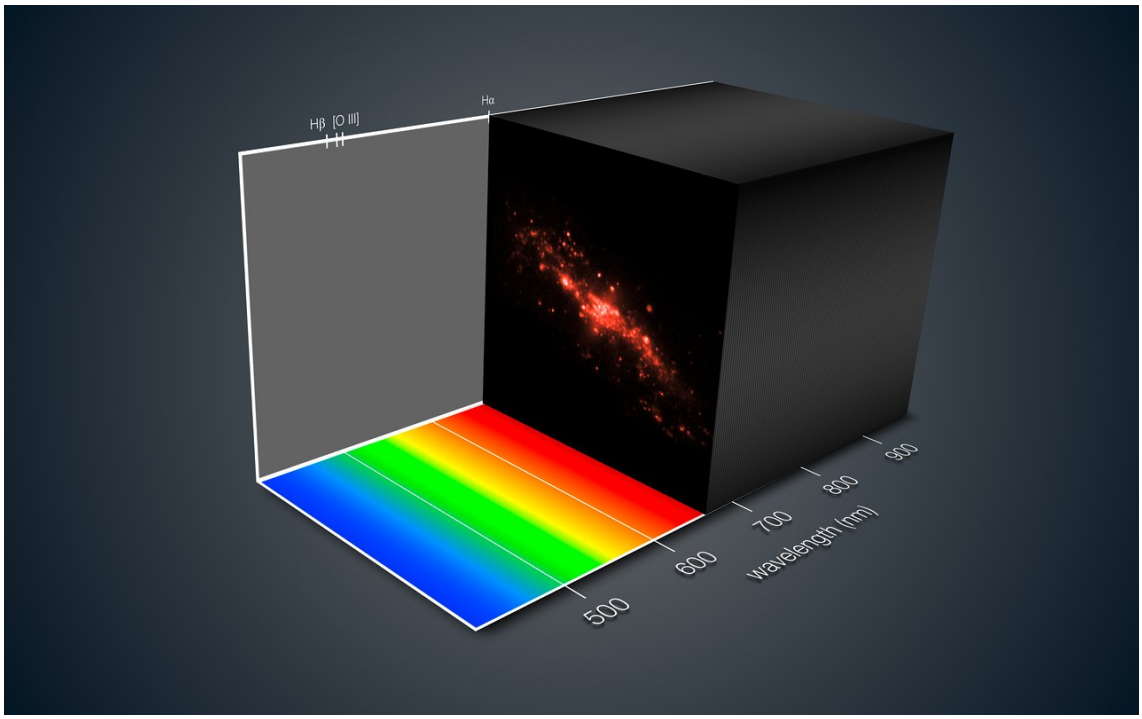

Figure 2.6: A schematic of a datacube from an integral field unit (IFU). Here the k axis is marked with the wavelength range of the MUSE spectrograph, and the galaxy frame shows x,y dimensions. Credit: ESO/MUSE consortium/R. Bacon/L. Calçada.

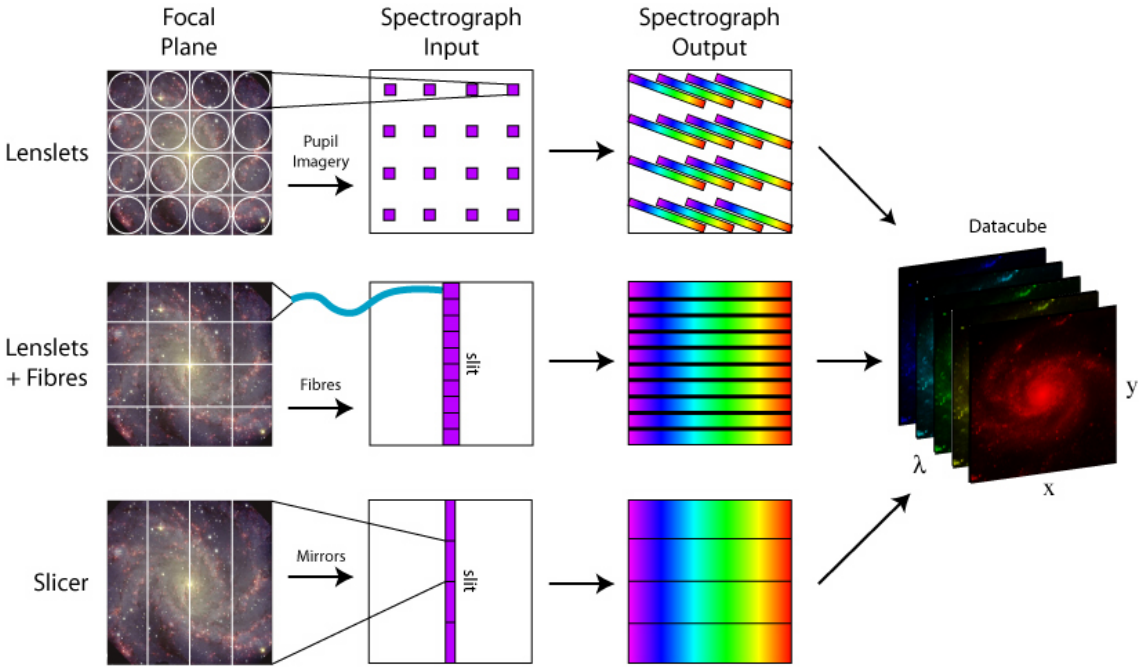

Figure 2.7: A schematic of different techniques which may be employed within integral field units. Each method redistributes the light from the focal plane to multiple spectrographs which are then reconstructed into a datacube final product. Credit: M. Westmoquette 2007

are SAURON at the William Herschel Telescope, (Bacon et al., 2001), and OSIRIS on Keck (Larkin et al., 2006).

The second generation of IFUs used a closely packed bundle of fibre-optic cables (which can be combined with lenslets to minimize focal ratio degredation). The light from each fibre can then be dispersed as required onto the detector, alike to multi-object spectrographs. An advantage of these systems is that they are relatively simple to 'piggyback' onto existing spectrographs. However, these systems struggle to maximise the fill factor for the fibres. Instruments using close-packed fibres are the Sydney-AAO Multi-object Integral-field (SAMI) at the Australian Astronomical Observatory (Croom et al., 2012), and Mapping Nearby Galaxies at Apache Point Observatory (MaNGA) (Bundy et al., 2015).

Some of the newest instruments are 'image slicer' IFUs. In this design the observed light passes through an array of differently angled mirrors which divide the light into strips across the frame. This directs each strip of data along different paths, to different gratings which disperse the light onto a detector. Image slicers provide a high density of spectra on the detector, with very few gaps in the image plane. These systems lead to efficient CCD usage, and a high throughput, however the manufacturing optics is challenging. Examples of image slicers are the Multi-Object Spectroscopic Explorers (MUSE) (Bacon et al., 2014), and the multi-object spectrograph KMOS (Sharples et al., 2013).

2.3.2 The MUSE instrument

Chapters 4 onwards are based on MUSE observations of massive, low-z ETGs. The instrument is on the ESO/VLT at Paranal, on telescope number 4 (UT4). MUSE is an optical IFU, operating between 4650 – 9350 Å with a mean resolving power of 3000. It has two imaging modes and each has the option to use adaptive optics (AO) to significantly improve the instrument resolution. The observations in this thesis were taken in wide-field mode, with no AO. The spatial pixel scale is 0.2×0.2 arcsecs within a 1×1 arcmin FoV.

As discussed in Section 1.5, the entire lensing configuration can be charactersized from a single IFU observation. The spectral resolution confirms a common source origin, and the

spatial resolution uncovers the number and position of the lensed images.

2.3.3 Summary

This chapter introduced the two gravitational lensing codes which are used in the forthcoming lensing analysis, and described the IFU MUSE which is used to observe low-z massive ETGs.

Of the two lensing codes, GRAVLENS will be used for lensing analysis in which the system is assumed to have point source images, or for analysis which requires the models to be re-run many times. The PYAUTOLENS software performs a more detailed analysis by including the lens light profile, and therefore can only be applied to systems with high resolution imaging where the lensed images are resolved.

IFUs are a powerful tool for detecting new gravitational strong lenses. The large wavelength dimension of the MUSE instrument is well-suited to the search for background emission line objects. In addition, the large FoV removes any possibility of a non-detection due to a highly asymmetric galaxy-scale lens configuration.

The following chapter will use GRAVLENS to re-analyse two lensing systems, SNL-1 and SNL-2, from the SNELLS sample.

CHAPTER 3

Improved mass constraints for two nearby strong-lensing elliptical galaxies from Hubble Space Telescope Imaging

---

This chapter closely follows the work in Collier et al. (2018a), MNRAS, published.

3.1 Preamble

The SINFONI Nearby Elliptical Lens Locator Survey (SNELLS) sample consists of three low-z early-type galaxy (ETG) strong-gravitational lenses. SNL-0 ($z = 0.034$) was a serendipitous discovery within *HST* data, and has a near-complete Einstein ring. SNL-1 (z = 0.031) and SNL-2 (z = 0.055), were discovered using SINFONI observations, and each has a doubly imaged background source. The lensing masses of all three are consistent with a MW-like IMF, in contrast to other samples of similarly massive ETGs, i.e. SLACS. For SNL-0, the high resolution data, combined with the configuration, robustly constrained the lensing mass. However, for SNL-1 and SNL-2 the poorer sampled (0.125×0.25 arcsec pixels) SINFONI data were used to measure the image positions. In addition, a doubly imaged lens configuration has a degeneracy between the lens mass and external shear,

which requires the relative magnification of the lensed images to be accurately measured. Hence, SNL-1 and SNL-2 are less well constrained. In this chapter, I present an update to the lensing analysis of SNL-1 and SNL-2 using imaging from the *Hubble Space Telescope* (*HST*) to precisely measure the image positions and the relative lensed image flux ratio.

3.2 Introduction

The three lowest redshift ($z \lesssim 0.05$) massive ETG lenses are ESO 325–G004, ESO 286–G022 and 2MASX J01414232–0735281. Whereas ESO 325–G004 was serendipitously discovered via *HST* imaging (Smith et al., 2005; Smith & Lucey, 2013), the other two lenses were identified via targeted integral-field infrared spectroscopy with SNELLS (Smith et al., 2015, hereafter SLC15); we refer to these three galaxy lens systems as SNL-0, SNL-1 and SNL-2, respectively. The SLC15 lensing analysis of the SNELLS systems favoured a Milky-Way like IMF (Kroupa, 2001) and is strongly inconsistent with the 'heavy' IMFs found in studies of massive ETGs using distant lenses, stellar dynamics, and direct spectral analysis (Treu et al., 2010; Cappellari et al., 2012; Conroy & van Dokkum, 2012a).

The very local nature of the SNELLS sample allows the application of multiple independent techniques to determine the IMF. High S/N optical spectra of the SNELLS lenses display features typical for a population of ETGs selected from SDSS to have similar velocity dispersions (σ = 280 km s^{-1}) (Newman et al., 2017, figure 5). The spectral features for SNL-2 are consistent with a MW-like IMF, in agreement with the lensing analysis, whereas the spectra of SNL-1 favours a 'heavy' IMF. Furthermore, the stellar population synthesis modelling for SNL-1 finds a mass in excess of the total lensing mass estimated by SLC15. This result is further evidence of a tension between the results of different IMF estimators, motivating a more refined lens model for both galaxies.

The lensing mass of SNL-0 is robustly determined from earlier *HST* observations (Smith & Lucey, 2013). SNL-0's near-complete Einstein ring lensing configuration provides accurate constraints on the mass model, with a 4 per cent uncertainty. By contrast SNL-1 and SNL-2 are two-image systems. The previous lensing analysis combined weak lensed-

Table 3.1: Galaxy properties of SNL-1 and SNL-2. The magnitudes are quoted in the observed frame. The quoted luminosities are corrected for band-shifting, derived from EZGAL (Mancone & Gonzalez, 2012), and galactic extinction, from Schlafly & Finkbeiner (2011). (The full 2MASS name for SNL-2 is 2MASXJ01414232-0735281) 1. Campbell et al. (2014) 2. Newman et al. (2017) 3. SLC15, SINFONI–based 4. PSF-corrected 2MASS 5. extinction and band-shifting corrected 6. this paper, *HST*–based

Quantity	SNL-1	SNL-2	Notes
NED ID	ESO 286-G022	2MASXJ0141-0735	
Lens z	0.0312	0.0519	
σ_{6dF} (km s^{-1})	356 ± 18	320 ± 18	1
$\sigma_{e/2}$ (km s^{-1})	289 ± 14	263 ± 13	2
Source z	0.926	1.969	
Fiducial aperture, R_{ap} (arcsec)	2.38	2.21	3
$J(\leq R_{ap})$	12.80	13.53	4
$I_{F814W}(\leq R_{ap})$	13.85 ± 0.02	14.53 ± 0.02	
$L_{F814W}(\leq R_{ap})$ (10^{10} L$_\odot$)	2.52 ± 0.04	3.86 ± 0.07	5
Half image-separation (arcsec)	2.43 ± 0.03	2.30 ± 0.03	6
$I_{F814W}(\leq$ separation)	13.83 ± 0.02	14.50 ± 0.02	
Flux Ratio (A/B)	2.2 ± 0.1	2.5 ± 0.1	

image positional constraints from SINFONI with low resolution 2MASS imaging (SLC15). The estimated mass uncertainties were 5 and 10 per cent, respectively, due to the unknown contribution from external effects (i.e. shear).

In this chapter, we present improved mass estimates for SNL-1 and SNL-2 by exploiting recently acquired *HST* imaging. In Section 3.3 we outline the data and our reduction procedures. In Section 3.4, we will provide a visual inspection of these galaxies, along with photometric analysis. In Section 3.5, we analyse the lensing geometry with multiple parametric models, building upon the previous work and exploiting newly measured lensed image flux ratios. Finally in Section 3.6, we summarise these results and compare them to SLC15.

We use parameters from the 7-year *Wilkinson Microwave Anisotropy Probe* (WMAP), i.e. $H_0 = 70.4$ km s^{-1} Mpc^{-1}, $\Omega_m = 0.272$ and $\Omega_\Lambda = 0.728$ (Komatsu et al., 2011).

3.3 Data

We observed SNL-1 and SNL-2 using *HST* Wide Field Camera 3 (WFC3), Uv-VISual (UVIS) channel, in GO cycle 23, (PI: Smith, R). We acquired three dithered F814W exposures for each target, for a total of 1050/1002 sec respectively. We took a further three dithered exposures totalling 4413/4272 sec, selecting a filter short of the 4000 Å break for the lens-galaxy, but longer than any potential line-of-sight Ly α absorption in the source galaxy spectrum. Due to the differing redshifts of the lens-galaxies, SNL-1 was observed using F336W, and SNL-2 in F390W.

We post-processed CALWF3 pipeline reduced UVIS data using the ASTRODRIZZLE software (Gonzaga, 2012). The images were drizzled onto a cosmic ray rejected final frame with a pixel scale of 0.025 arcsec/pix. Due to the limited number of frames in each passband, some artefacts remain after this process, which were masked in the subsequent analysis.

3.4 Lens and source properties

In this section we report our measurements from the *HST* imaging. This includes: (a) morphological descriptions of the lens and the lensed sources, (b) improved measurements of the lensed image positions and their relative fluxes, (c) independent measurements of the lens structural properties. The relevant parameters are summarised in Table 3.1.

SNL-1

Extracted regions from the *HST* imaging for SNL-1 are shown in Figure 3.1(a-d). SNL-1 displays a regular E/S0 morphology, with an ellipticity of ~ 0.4 (measured at the half-image separation from an ELLIPSE fit), and slightly discy isophotes. SNL-1 was shown to be a fast rotator by Newman et al. (2017) and the *HST* imaging reveals dust obscuration within the central region (~ 1 arcsec, Figure 3.1b). This suggests the presence of a small cold ISM disc.

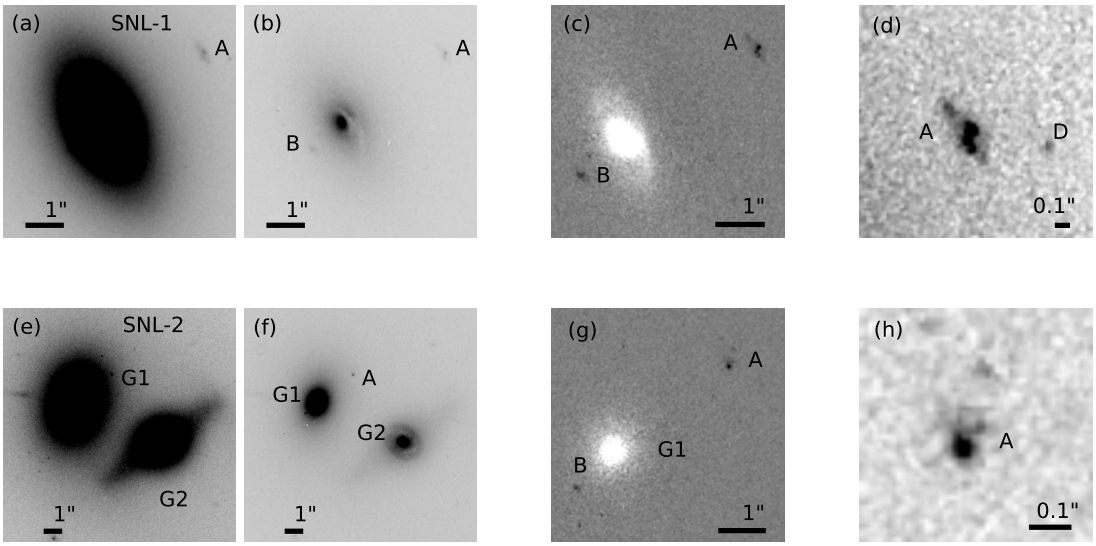

Figure 3.1: *HST* data of SNL-1 and SNL-2. Panels (a-d) show SNL-1. A is the outer, and B the inner lensed image. (a) F814W image showing the lens ellipticity. (b) F336W image showing the inner obscuration from a disc. (c) scaled F336W with F814W subtracted for improved contrast of the lensed images. (d) detail of the outer image, A; there is a faint object D, which may or may not be associated. Panels (e-h) show SNL-2, G1 is SNL-2, G2 is the companion galaxy, with A the outer, and B the inner lensed image. (e) F814W image containing the lens and companion (f) F390W image showing the star formation ring in G2. (g) Scaled F390W with F814W subtracted for improved contrast of the lensed images. (h) the outer image, showing a compact core with a potentially associated diffuse structure.

The *HST* imaging confirms the two-image system discovered from previous SINFONI data. In Figure 3.1(d), we see internal structure in the background source. The outer image, A, displays a clumpy structure with a bright core, implying a late-type galaxy. Little structure is visible in the inner image. From the new imaging we improve the locational constraints of the lensed images, and measure a half-image separation of 2.43 ± 0.03 arcsec, which is 2 per cent larger than in SLC15. We derive the uncertainty from our ability to define centroids for the lensed images' internal structure. The observed flux ratio (A/B) is 2.2±0.1, measured from aperture photometry within a lens-galaxy-subtracted image.

We measure the total lens flux with a two part model. The first component is a direct summation of the flux inside an elliptical aperture with a radius set at a preliminary estimate for $R_{\rm Eff}$. The second component derives the flux contribution outside this region with a 1D Sérsic fit to the outer profile. We find the total magnitude to be $I_{F814W} = 12.75 \pm 0.05$, and a half-light radius of 3.90 ± 0.03 arcsec. This is ~ 20 per cent larger than the low S/N 2MASS-based $R_{\rm Eff}$measurement reported in SLC15.

For consistency with previous work, we adopt a fiducial aperture of $R_{ap} = 2.38$ arcsec (the half-image separation derived by SLC15) when quoting magnitude measurements. We find $I_{F814W}(\leq R_{ap}) = 13.85 \pm 0.02$. Combined with the J band measured in SLC15 we measure an $(I_{F814W} - J)$ colour of 1.05, which is consistent with the range of 1.01–1.07 derived for old metal-rich populations from synthesis models (Conroy et al., 2009).

SNL-2

We present the *HST* imaging of SNL-2, in Figure 3.1(e-h). SNL-2 is confirmed to have an elliptical morphology, with a smooth light profile, and no discernible additional structure. However, SNL-2 lies with a nearby galaxy within a common, extensive and non-symmetric diffuse light halo. The companion, G2, located ~ 7 arcsec away, is an edge-on late-type galaxy, with disk and bulge components. A star-forming ring within the companion's central bulge is seen in Figure 3.1(f).

SNL-2 is confirmed to have a two-image lensing system, as found in the original SINFONI

discovery data. The bright outer image, A, is a compact object, shown in Figure 3.1(h). We clearly observe a bright central region, with a tentatively associated low brightness structure extending outwards in a single direction. It is possible that an AGN dominates the flux of SNL-2's source, however the exotic lines which may confirm this explanation cannot be confirmed. From the imaging, we measure a half-image separation of 2.30 ± 0.03 arcsec (a 4 per cent increase on SLC15), with an uncertainty from our ability to centroid the unresolved source, and a flux ratio (A/B) of 2.5 ± 0.1.

Due to the more complex local environment of SNL-2, we use GALFIT (Peng et al., 2002) to model and subtract the companion. We model the companion with a Sérsic bulge and a $n \approx 1$ Sérsic disc. Then we fit SNL-2's light profile following the procedure used for SNL-1. We measure a total magnitude of $I_{F814W} = 13.80 \pm 0.10$, and an effective radius of 3.25 ± 0.03 arcsec. This is significantly smaller than the 6 arcsec measured by SLC15, from low S/N 2MASS imaging. However, the complexity of SNL-2 with a bumpy, asymmetric light halo and companion galaxy limits the accuracy achievable when modelling this two-galaxy system.

As with SNL-1, we measure the magnitudes within a fiducial radius, in this case adopted as $R_{ap} = 2.21$ arcsec, shown in Table 3.1. The (I_{F814W}-J) colour of 1.00 is slightly bluer than the synthesis model predictions of 1.04–1.11 for old metal-rich populations (Conroy et al., 2009).

3.5 Lens modelling

The main aim for this study, is to improve the mass estimates for SNL-1 and SNL-2 beyond the basic treatment in SLC15. We use the LENSMODEL code (Keeton, 2001) to create parametrized profiles for each lensing system, informed by the *HST* imaging under the assumption that stellar mass dominates the lensing deflections (See Section 2.2.1, for a discussion on the selected profiles). We measure the profiles' normalization, from which we extract the mass enclosed within the fiducial radius (R_{ap}, from Table 3.1). In Section 3.5.1 we apply only the improved image position constraints. Then in Section 3.5.2 we

Table 3.2: Lens mass estimates from LENSMODEL in units of 10^{10} $M_{\odot}$. Masses are measured within the fiducial radius, R_{ap}. However the values are derived from the *HST* data and refined mass models.

Model	SNL-1	SNL-2	Notes
Constrained by image positions, no shear			
SLC15	9.27	13.07	table 2, No f_{corr}
SIS	9.48	13.62	
SIE	8.78	14.11	
MFL	9.22	13.42	
Constrained by flux ratio and positions, with shear (Shear)			
SIS + γ	9.08	–	+4.3 %
SIE + γ	9.57	–	–8.8 %
MFL + γ	9.41	–	–2.1 %
Constrained by image positions with companion (Flux Ratio)			
MFL + SIS	–	12.83	3.28
MFL + SIE	–	12.87	3.26
MFL + MFL	–	13.15	3.75
Constrained by flux ratio, positions with companion			
MFL + SIS	–	12.28	
MFL + SIE	–	12.38	
MFL + MFL	–	12.69	
Adopted Mass	**9.49±0.15**	**12.59±0.30**	

include information from image flux measurements to break the degeneracy between mass and external shear for SNL-1, and constrain the companion's effect on SNL-2. The results of our analysis are summarised in Table 3.2.

3.5.1 Positional constraints

For SNL-1, we start our analysis with a singular isothermal sphere (SIS). This is the closest model to the spherical symmetry used in SLC15. From the SIS model we measure $M(\leq R_{ap}) = 9.48 \times 10^{10}$ $M_{\odot}$, 2 per cent larger than the previous estimate, due to the increased image separation. Figure 3.1(a) shows SNL-1 to have significant ellipticity, and to be orientated off axis to the image separation. We incorporate this using a singular isothermal ellipsoid (SIE) profile with a fixed ellipticity of 0.4. The resulting enclosed mass within R_{ap} is ~ 7 per cent smaller than predicted using a SIS model.

As the stellar mass dominates within R_{Ein}, we create a pixelised mass-follows-light (MFL) profile for the mass distribution. For the light profile we use an IRAF ELLIPSE

fit (Jedrzejewski, 1987), to minimise contamination from both the dust lane and the lensed images, as the basis for the mass profile. We assume the surface mass density is proportional to the surface brightness, such that the resulting model normalization is the mass-to-light ratio. The MFL estimated mass is ~ 3 per cent smaller than the SIS model.

For SNL-2 we begin with a simplified case, in which we neglect the companion, and follow the procedure for SNL-1. The SIS model mass is ~ 4 per cent larger than in SLC15, attributable to the larger *HST* measured image separation. We observe that SNL-2, like SNL-1, has a non-zero ellipticity and so model a SIE case, which increases the estimated mass by ~ 4 per cent. We form a MFL profile for SNL-2, from an ELLIPSE fit to a companion-subtracted F814W image, which will account for structure in the light profile. The MFL model estimates $M(\leq R_{ap})$ to be ~ 1.5 per cent smaller than SIS model.

3.5.2 Flux constraints

The previous lensing solutions assume an isolated lens galaxy. In reality the local environment causes a measurable effect on the lensing configuration, resulting in a degeneracy between mass and external shear (γ). An external shear causes an expansion along a given axis, and a perpendicular compression. We define a positive/negative shear to represent expansion/compression dominating in the image-separation axis, which reduces/increases the required enclosed mass for a given set of image positions. As the shear factor varies, the magnification of each image from a lensed source will change (illustrated for SNL-1 in Figure 3.2). The observed flux ratio, acting as a proxy for relative magnification of the lensed images, can therefore break this degeneracy between mass and shear.

For SNL-1, we constrain the shear using the measured flux ratio (A/B) of 2.2 ± 0.1, and show the resultant masses in Table 3.2. For the SIE and MFL profiles this method recovers a compressive (negative) shear, increasing the measured lensing mass by ~ 9 and ~ 2 per cent respectively. (The SIS is less well defined, as the shear factor accounts for the combined effects of ellipticity, orientation and shear in this case.) Adopting the SIE+γ and

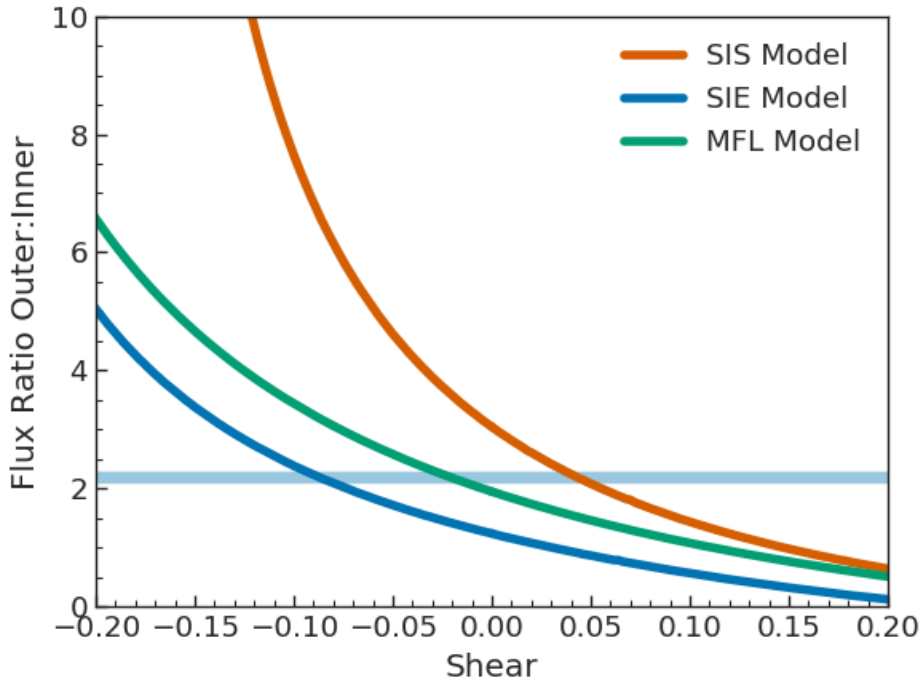

Figure 3.2: The external shear for given fixed image positions will modify the magnification each lensed image is subject to. We show this for SNL-1, comparing the predicted flux ratio of the lensed images to the shear. We shade in blue the measured flux ratio range of 2.2 ± 0.1, indicating a weak compressive (negative) shear along the image-separation axis, for the SIE and MFL models.

MFL+γ models we derive limits on $M(\leq R_{ap})$ from model-to-model uncertainty, within the flux ratio bounds, to be $9.34 - 9.64 \times 10^{10}$ $M_{\odot}$, which is shaded in Figure 3.3.

For SNL-2, the close companion galaxy likely dominates the external mass distribution. We constrain the companion galaxy's contribution with the measured flux ratio, similar to the method for SNL-1. We treat SNL-2 with a MFL model throughout, and consider SIS, SIE and MFL descriptions for the secondary. We use these two-component models to predict the flux ratio as a function of the companion's mass normalization. In Figure 3.4, we compare the total lensing mass to the observed flux ratio (A/B), of 2.5 ± 0.1. We find close agreement between the SIS and SIE secondary models, with significant divergence in the MFL case toward low flux ratios. As the companion is external to the primary lens configuration, we must consider its extended profile, and thus total (stars plus dark matter) mass. We therefore prefer the isothermal models for our treatment of the companion.

As shown in Figure 3.4, there are no models which match both the image positions and

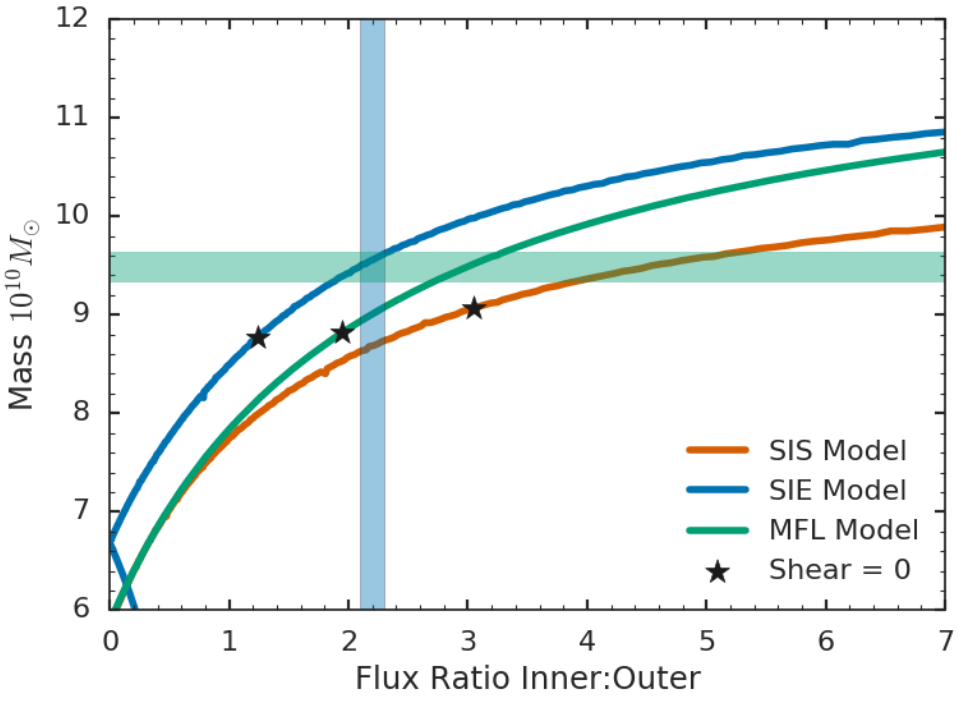

Figure 3.3: The model predicted flux ratio against mass for the three primary lens models of SNL-1. We shade the measured flux ratio of 2.20 ± 0.1 in blue, from which we estimate the mass range breaking the mass-vs-shear degeneracy. The star symbols display the mass estimated for the case of no external shear. The mass range estimated by the SIE and MFL models for SNL-1 is shaded in green.

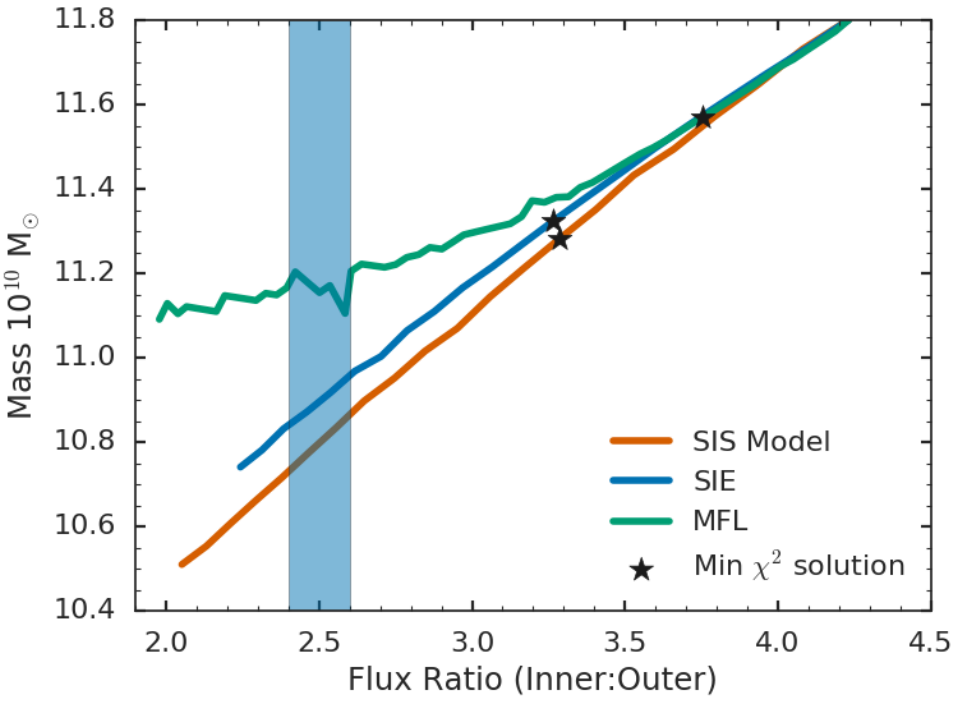

Figure 3.4: The modelled mass for SNL-2 against flux ratios for a varying mass companion. The shaded region defines the measured flux ratio of 2.5 ± 0.1, with the black symbols indicating the best fit for the image positions. In order to fit the measured flux ratio, the offset in image position is ~ 0.1 arcsec.

the observed image flux ratio. The models which reproduce the measured flux ratios yield a lensing mass of $\sim 12.33 \times 10^{10}$ $M_\odot$, but lead to an offset of ~ 0.1 arcsec between the observed and predicted image positions. The models which best fit the image positions lead to a comparatively heavier primary lens, with a mass of $\sim 12.85 \times 10^{10}$ $M_\odot$.

The deviation between measured and predicted flux ratios in our modelling, (2.5 and ~ 3.3 respectively) seen in Figure 3.4, corresponds to ~ 0.3 magnitudes. The compact nature of the source galaxy tentatively suggests a flux dominated by AGN activity, and for such a source microlensing can cause a discrepancy between the measured and predicted flux ratios of order a few tenths of a magnitude (e.g. Schechter & Wambsganss, 2002; Schechter et al., 2014). Alternatively a similar effect may result from intrinsic AGN variability combined with lensing path-length differences. These factors preclude obtaining an improved lensing mass estimate for this galaxy with the present data.

3.6 Discussion and conclusion

The newly acquired *HST* data have revealed insights into the two-image lensing systems from SNELLS, including uncovering evidence for a previously unknown dust disc within the fast rotating SNL-1. We improved upon previous strong lensing analysis using the *HST* data to break the mass-vs-shear and companion degeneracies for SNL-1 and SNL-2 respectively. We measure precise lensed-image positions, and reliably quantify the lensed image flux ratio, which was not possible with the SINFONI discovery data. We compare our adopted masses, shown in Table 3.2, to those of SLC15, and estimate the stellar mass-to-light ratio (Υ). Furthermore, combining the measured mass and luminosity in this paper, with the spectroscopically fit Kroupa reference stellar mass-to-light ratio ($\Upsilon_{\rm ref}$) (Newman et al., 2017, table 1) (converted to I_{F814W} from the *r*-band, with EZGAL) we independently estimate the IMF mismatch parameter α within the fiducial radius (R_{ap}).

For SNL-1 we adopt a final lensing mass estimate of $M(\leq R_{ap}) = 9.49 \pm 0.15 \times 10^{10}\ M_{\odot}$, from the SIE+$\gamma$ and MFL+γ models. The quoted error is derived from the spread between lens profiles incorporating the flux ratio uncertainty. Due to the extended nature of the source, the contribution from microlensing is negligible. The positional errors provide a formal uncertainty of ≤ 0.5 per cent. We obtain the stellar mass by subtracting the EAGLE DM mass contribution estimated in SLC15 (~ 15 per cent) from the lensing mass. The estimated I_{F814W} measured $\Upsilon_{R_{ap}}$ is 3.21 ± 0.12, and so combined with the converted $\Upsilon_{\rm ref}$ of 2.75 (Newman et al., 2017), we derive $\alpha = 1.17 \pm 0.09$. This is 3 per cent smaller than 1.20 ± 0.13 found by SLC15.

For SNL-2 the final lensing mass estimate is $M(\leq R_{ap}) = 12.59 \pm 0.30 \times 10^{10}\ M_{\odot}$, derived from the MFL+SIS, and MFL+SIE models for the two regimes in Table 3.2. The uncertainty is dominated by tension between the measured and predicted flux ratios. Following the SLC15 EAGLE DM procedure, and incorporating the newly measured I_{F814W} luminosity we estimate $\Upsilon_{R_{ap}}$ to be 2.49 ± 0.15. With the converted $\Upsilon_{\rm ref} = 2.59$, we obtain $\alpha \simeq 0.96 \pm 0.10$. This is a 2 per cent increase upon 0.94 ± 0.17 measured by SLC15.

In conclusion, our analysis of higher resolution and deeper imaging of SNL-1 and SNL-2 from *HST* supports the lensing masses, and the IMF α factors, estimated by SLC15. For SNL-2 further caution is required due to the complexity in modelling its source and companion galaxy. For SNL-1 the results show that the discrepancies in α reported by Newman et al. (2017) can not be attributed to the simplistic assumptions of the SLC15 lens modelling. Future stellar- and gas-dynamical studies of SNL-1 should help to resolve this specific puzzle, and perhaps by implication begin to provide an explanation for the broader issue of agreement between the various methods for constraining the IMF.

3.7 Summary

In this chapter, I presented the improved lens modelling of SNL-1 and SNL-2. The imaging reveals previously unseen structure in both the lens galaxies and lensed images. For SNL-1, which has a well-resolved source, the mass-vs-shear degeneracy is broken using the relative flux information. The measured lensing mass is $9.49 \pm 0.15 \times 10^{10}$ $M_{\odot}$, a 7 per cent increase on the previous estimate. For SNL-2, the imaging reveals a bright unresolved component to the source and this presents additional complexity due to possible AGN microlensing or variability. Using the relative magnification information to constrain the contribution from the nearby companion galaxy, the measured lensing mass for SNL-2 is $12.59 \pm 0.30 \times 10^{10}$ $M_{\odot}$, a 9 per cent increase in mass. The results are consistent with the previous analysis, with newly measured mass excess parameters of 1.17 ± 0.09 and 0.96 ± 0.10 for SNL-1 and SNL-2, respectively, relative to a MW-like IMF.

A key result from this chapter, is that although high resolution data is required to precisely constrain a lensing system, the lower resolution discovery data are sufficient for these purposes. Therefore, future lens searches with other IFU instruments can confidently make measurements of the lensing masses without follow-up data. The next chapter will discuss a new lens search, using the MUSE instrument (see Section 2.3.2). This search aims to discover new lensing systems comparable with the SNELLS sample. New lenses are required to constraint the distribution of α within massive ETGs.

CHAPTER 4

MNELLS: The search for strong-lensed emitters

This chapter is based on the first half of *MNELLS: The MUSE nearby Early-Type Lens Locator Survey* (Collier et al., 2020).

4.1 Preamble

Low-redshift strong-lensing galaxies provide robust measurements of the stellar mass-to-light ratios in early-type galaxies (ETG) and hence constrain variations in the stellar initial mass function (IMF). However, at present only a few such systems are known. The three SNELLS lenses have all been thoroughly analysed to infer their IMF, using lensing (see Chapter 3), dynamics, and stellar population modelling (see Section 1.6, Newman et al., 2017; Collier et al., 2018a). All three lenses are consistent with a MW-like IMF. However, with only three, the *intrinsic* distribution of α within the massive ($\sigma \simeq 300\,\mathrm{kms}^{-1}$) ETG population cannot be fit without a poorly-constrained intrinsic scatter.

To improve the *intrinsic* scatter constraints, new lenses are required. In this chapter, I report the results from a blind search for gravitationally-lensed emission-line sources behind 52 massive $z < 0.07$ ETGs with MUSE integral field spectroscopy. The sample comprises 36 galaxies selected from the ESO archive and 16 galaxies which are specifically targeted

with new observations (MNELLS). Each observation is searched for background emitters, and the results are presented in Tables 4.1 and 4.2.

4.2 Introduction

Recent efforts to detect low-redshift strong-lensing ETGs have been driven largely by the seeming discrepancy between the measured α parameters of the SLACS lenses ($\langle z \rangle \sim 0.2$), compared to those from the SINFONI nearby elliptical lens locator survey (SNELLS, Smith et al., 2015, $\langle z \rangle \sim 0.03$). These two samples measure significantly different IMFs within massive (high velocity dispersion) ETGs, i.e. at the 3σ level. Additionally, these SNELLS lenses are valuable as they provide a 'golden sample' for which all three of the main IMF tracing techniques—strong-lensing, stellar dynamics and spectral synthesis—can be applied, and therefore compared (Newman et al., 2017). However, observable strong gravitational lensing by nearby massive ETGs is inherently rare.

Broadly, there are two techniques for discovering strong-gravitational lenses, as discussed in Section 1.5. A sample discovered with a single technique may incorporate biases into the sample (i.e. the lensed images to be bright compared to the lens, or there must be enough flux within the fibre aperture). However, each of these classical techniques (broad-band imaging or fibre spectroscopy) requires the other to confirm the lensing system. The newest method combines both, using large field-of-view IFUs to resolve both the spatial and spectral information of the lens system. This technique should also reduce the biases, with minimised edge-effects and faint image detection.

To date, almost all low-redshift lenses have been discovered with IFU observations. Two lenses, SNL-1, and SNL-2 were the subject of targeted observations with the SINFONI instrument for the SNELLS survey (Smith, Lucey & Conroy, 2015). An additional lens, J0403-0239 (Chapter 6, and Collier, Smith & Lucey, 2018b), was discovered in archival data from the Multi-Unit Spectroscopic Explorer (MUSE, Bacon et al., 2014), with the observation taken for non-lensing science. This lens was independently reported by Galbany et al. (2018). With the completion of current large IFU surveys, (i.e. SDSS-IV

MaNGA, SAMI, Bundy et al., 2015; Bryant et al., 2015), of order 10^4 galaxies will be observed and searched for lensed images. Future surveys such as HECTOR (Bland-Hawthorn, 2015) will expand the size of this sample towards 10^5 galaxies. The MaNGA survey selects nearby galaxies across a range of masses and environments, with a median redshift of $z \sim 0.05$. However, the massive ETGs tend to lie at higher redshift so the same fraction of $R_{\rm Eff}$ is sampled by the instrument FoV. In the DR14 data-release Smith (2017) discovered one new lens, and new candidate systems were reported from a sample of galaxies by Talbot et al. (2018).

A key difference between the SNELLS approach and the MaNGA and SAMI surveys is the selection criteria for the targeted galaxies. SNELLS selected only the most massive ETGs as they have the largest lensing cross-sections. In doing so, the number of galaxies which must be observed to return a significant yield of lenses is greatly reduced. Although SNELLS discovered two lenses, choosing to use SINFONI for this search has limitations. The FoV of 8×8 arcsec leads to highly asymmetric systems still being contaminated by FoV edge effects, see SNL-2, (Smith et al., 2015). In addition, the wavelength range 1.1–2.45 μm limits the number of emitters being probed, as only sources with redshift greater than ~ 0.7 will have strong emission lines, such as Hα, in the detection range. Furthermore, there is a significant sky background present when working in the near-IR.

To overcome some of these limitations, we extend the technique to a wide FoV optical IFU. The MUSE Nearby Early-Type Galaxy Lens Locator Survey (MNELLS) utilises the 1×1 arcmin FoV to detect even the most asymmetric systems, whilst retaining a high angular sampling (0.2×0.2 arcsec). The wavelength range of 4750 – 9300 Å probes [O II] emitters up to a redshift of $z = 1.5$ and Ly-α above $z \sim 3$. Here, we work with data from the ESO Period 101 observations (PI: Smith). As the MUSE IFU has been in operation since 2014, we also select galaxies from the large public archive.

In this chapter, we report the results from our targeted and archival lens searches. In Section 4.3 we present the sample selection for the targeted observations and the archival sample. In Section 4.4 we present the process for identifying the emission-line sources within the datacubes. We report detections and promising candidates from the sample in Section 5.3.

Our lensing analysis is presented in Section 5.4, and we assess the detection limits of our search in Section 5.5. In Section 5.5.3 we compare our reliability and detection limits of our observations compared to those expected and comment on implications of this for future searches.

In this chapter we adopt cosmology from Planck Collaboration et al. (2018), i.e. $H_0 = 67.4$ km s^{-1} Mpc^{-1}, $\Omega_m = 0.315$ and $\Omega_\Lambda = 0.685$.

4.3 Data

In this section we outline the sample selection for the galaxies which will be used in our analysis. We describe our MUSE targeted programme in Section 4.3.1, and then our selection of archival MUSE observations in Section 4.3.2.

4.3.1 Targeted sample

Our MUSE survey targets massive ETGs, selected by velocity dispersion, in the local universe. These massive galaxies maximise the lensing cross-section per target, and hence increase the probability of discovering a lens. In this subsection we outline our target selection criteria.

4.3.1.1 Target selection

MNELLS builds upon the previous SNELLS survey, and we used the following selection criteria, similar to the earlier work:

1. A redshift, $z < 0.060$.

2. A stellar velocity dispersion measured from high S/N spectra, from either the 6dFGSv (Campbell et al., 2014), or SDSS (York et al., 2000), ($\sigma_{6dF} > 300\,\mathrm{km\,s^{-1}}$, $\sigma_{SDSS} > 310\,\mathrm{km\,s^{-1}}$, to allow for the differing fibre sizes).

3. The galaxy must not lie in a rich cluster/massive group environment. This prevents additional complexity in the modelling to account for either the cluster potential, or lensing effects (external shear) from other nearby massive galaxies. We judge this using the NASA/IPAC Extragalactic Database.

4. The galaxy must be observable in ESO Period 101, April - September from the VLT. The targets were chosen to cover the full Right Ascension range available for the semester, with a preference for southern Declinations, to take advantage of the wind restrictions on northern pointings at Paranal.

4.3.1.2 Observations and data reduction

The MUSE observations were undertaken in service mode (April - September 2018). Each galaxy was assigned two 40 minute observing blocks (OB, rotated by 45 deg), composed of four 380 second exposures. Using wide-field no-AO mode, each frame consists of a 1×1 arcmin^2 FoV, with a pixel scale of 0.2×0.2 arcsec and a wavelength resolution of ~ 2.7 Å, sampled at 1.25 Å/pix.

A total of 16 candidates were observed, and of these, 14 have both OBs (i.e. full depth). The average PSF is 1 arcsec. The galaxies with at least one OB are shown in Table 4.1. Each observation was retrieved as a pipeline-reduced file as provided by ESO.

4.3.2 MUSE archival sample

There are over 9000 existing MUSE observations publicly available. Therefore, we supplement our targeted programme with archival data. As the data already exist we relax our criteria from the very restrictive targeted selection of Section 4.3.1∗. Particularly, we allow BCGs into the sample† as these can act as strong-lenses for the same background

∗In principle the archive could be searched for strong gravitational lenses independent of specific morphologies or redshift. However, this is beyond the scope of this work, specific to the IMF of massive ETGs.

†BCGs are excluded from the targeted survey as the lensing mass is typically dominated by DM, and the galaxy has a low surface brightness, compared to a field massive ETG, and hence mass density. This leads to a $R_{\rm Ein}$ significantly larger than found in a typical isolated galaxy. Hence, the DM modelling dominates the uncertainty on the constraints of the IMF.

emitters. In this subsection, we outline our selection criteria for the supplementary sample drawn from the MUSE archive.

4.3.2.1 Target selection and observations

In order to build a sample of low-z galaxies from the MUSE archive, we use positions, redshifts and luminosities from the 2MASS Redshift Survey (2MRS, Huchra et al., 2012). We use the 2MRS due to its high completeness in our redshift range. We select galaxies with redshifts $0.01 \leq z \leq 0.07$, and massive galaxies with a cut on the absolute K band magnitude (as a proxy for stellar mass), at K $\leq$ –25.4 mag. We show the redshift distribution of the matched galaxies against their absolute magnitude in Figure 4.1. All observations which were publicly available as of February 2019 were searched.

We visually inspect the MUSE collapsed datacube product, in order to exclude galaxies which would require complex lens analysis (i.e. very nearby similarly sized galaxies, or an irregular light profile). We also exclude galaxies which may have complex stellar populations (i.e. extended/strong emission, and mergers), or are of a spiral morphology. The resulting archival sample totals 36 galaxies.

The investigated galaxy properties, along with the run ID and exposure times are listed in Table 4.2. Many of the observations were acquired by the 'MUSE most massive galaxy (M3G)' survey (Krajnović et al., 2018, PI: Emsellem).

For each galaxy in the sample we select the deepest available observation, which in many cases is the MUSE-DEEP data product. The datacubes are acquired as an ESO pipeline reduced final product. The selected observations range from exposure times comparable to, or shorter than our MNELLS sample, $<$ 3600 seconds, or much longer, $>$10000 seconds and have varied seeing conditions.

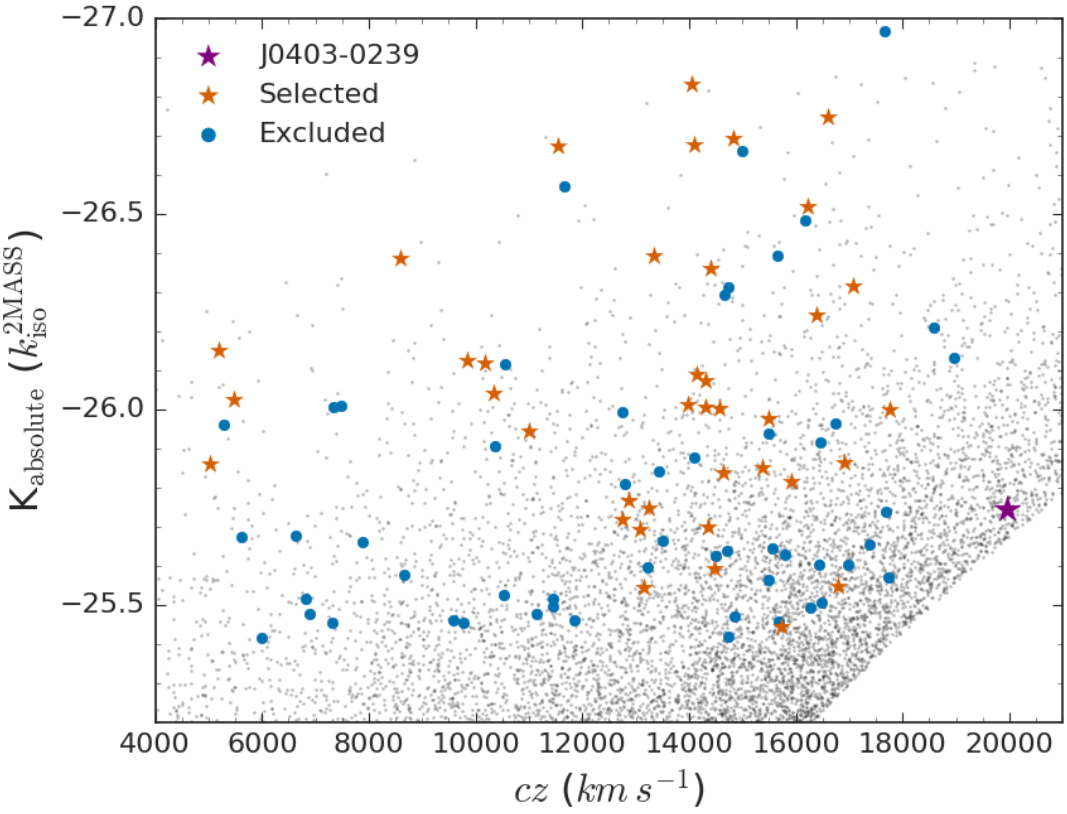

Figure 4.1: The redshift and absolute magnitude distribution of the 2MRS galaxies (background points), with those previously observed with MUSE (red, blue and purple points). Out of those matched to the MUSE archive we exclude a large number of systems (usually due to a complex light profile, morphology or companion galaxies), in blue, and mark the selected galaxies with red points. The confirmed lens J0403-0239 is shown in purple.

4.4 Galaxy subtraction and emission line detection

In this section, we outline our method to detect background emission line sources. In the SNELLS survey, each datacube was visually inspected to search for background emitters. Here, we automate the process, incorporating a search algorithm as a first pass. Then we visually inspect each detection to confirm the reliability.

The detection process consists of two main steps: 1) the removal of the foreground, candidate lens light profile and other nearby bright continuum objects and 2) the detection and identification of emitters within the continuum-subtracted datacubes.

To help isolate compact narrow emission features, we first subtract a continuum spectrum from each pixel computed using a running median with a 75 Å bandwidth. The residuals from this step are next fitted with an elliptical profile computed for each wavelength channel independently, with the centre, ellipticity and position angle fixed to match the target galaxy. When other bright sources are present in the field, their residuals are modelled similarly. This process works well except near strong spectral features in fast-rotating galaxies. After subtracting these profiles, the remaining residuals are normalised to the local standard deviation (estimated using quantiles for robustness) and smoothed with a Gaussian of 0.6 arcsec FWHM in the spatial directions and 3.5 Å FWHM in wavelength.

We developed a python-based framework for detecting emission line features within the filtered and smoothed datacubes using routines from the SCIPY.NDIMAGES.LABEL package. This package groups connected pixels above a threshold, allowing the spatially and spectrally extended peaks, due to the emission line features, to be identified. The selection of the threshold involves a trade-off between the number of spurious detections to inspect manually, and those faint sources which may be missed.

The smoothed residual datacube is separated into 40 Å slices with an overlap of 5Å and a labelling threshold is applied. For each labelled region, the number of pixels and the spatial extent are required to be above thresholds of 10 and 2×2 respectively. Those which do not meet these criteria are not considered for further processing. These are usually

artefacts from the subtraction of bright sky lines, or the lens candidates light. If a detected source is spatially and spectrally extended, this is a strong indication of an emission line, which is then processed for identification.

The candidate emitter's spectrum is extracted within a 2 arcsec diameter aperture, and at ± 125 Å around the brightest detected pixel. This range is chosen to contain [O III] 4959 Å if the lead detection is [O III] 5007 Å, whilst avoiding H β to simplify the emission line fitting. (The range will also contain [N II] for H α.) The extracted spectrum is then fit with a single, double and triple Gaussian, with appropriate peak ratios and separation for [O II], [O III], and H α+[N II]. We perform a chi-square minimisation to select the best fit identification, and measure a redshift.

After these detections are carried out for each 40 Å segment of the datacube, we matched detections spatially to combine sources with multiple emission lines at a consistent redshift, and included a step to associate the single Gaussian lines to other identified lines (generally this matches H β to detected [O III]). We do not specifically fit the asymmetric Lyman–α profile, as these will be the best fit with a single Gaussian with a wide FWHM, and so will be included in the sample without more complex modelling.

Finally the candidate lines are manually inspected and either verified as sources or rejected. Sources within a 10 arcsec radius of the candidate lens centre are recorded separately. This minimises the time per datacube on a first pass for lensed images. In Figure 4.2, we show an example of the outputs which were visually inspected. Narrowband images of the respective positions for the four strongest optical emission lines ([O II], H β, [O III], and H α) are displayed in the top panels. Inspecting the panels will show those detections which appear false in the spectral domain due to their lack of a clear peak, or spatial extent due to a residual (see Section 4.4.1 for an example of an excluded detection).

The end result of the processing described in this section is a final catalogue of visually-screened emission line sources for each datacube.

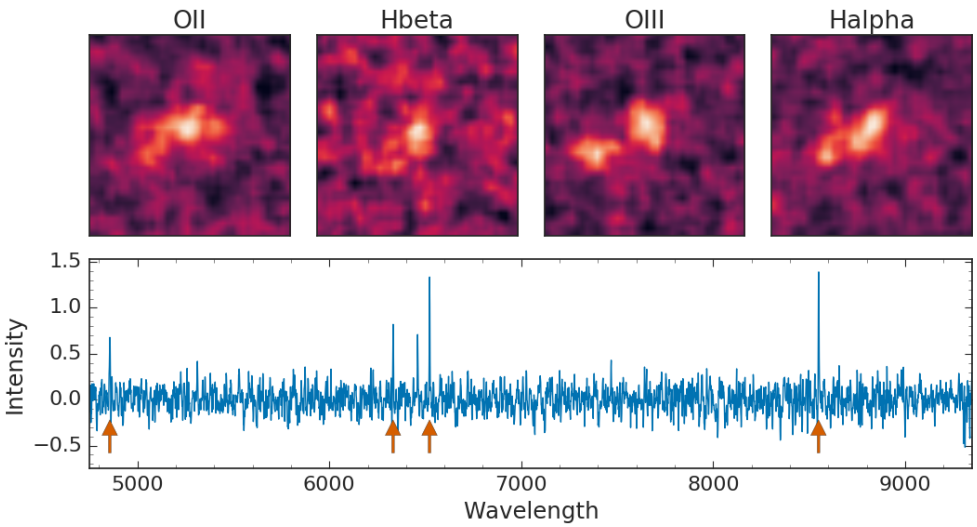

Figure 4.2: An example emitter from a MNELLS observation. The upper panels show the spatial extent of the emission in narrow-band slices around [O II], H β, [O III] and H α, which tend to be the strongest optical emission lines. The panel size is 8×8 arcsec. Below is the spectrum extracted within a 2 arcsec diameter aperture, at redshift 0.3024. The emission lines extracted for the narrowband images are indicated with orange arrows.

4.4.1 Example rejected emitter detection

We show an example of a rejected detection in Figure 4.3. In this example, the detection is of a H α residual at the redshift of the candidate galaxy. The process can be automated to reject such emission during the detection process, using the known lens redshift. As the [O II] emission line is outside of the MUSE wavelength range the panel which would contain a narrowband extraction is left blank.

4.5 The Emission Line Detections

We display the tabulated results for the 52 galaxies in this section. Each was subject to a consistent search method which was detailed in this chapter. The results are summarised in Table 4.1 for MNELLS (N = 16), and Table 4.2 for the archival search (N = 36).

Each system is labelled as a not, or single- and multiple- imaged. These systems are the key to analysis in the following chapter. A single-imaged system is defined as a galaxy

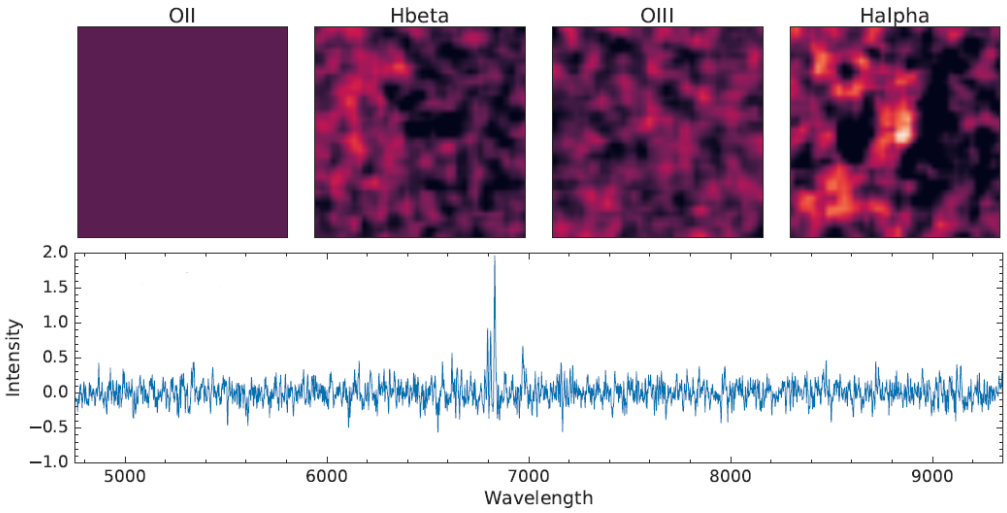

Figure 4.3: An example rejected detection from a MNELLS observation of J0058-1628. The four panels across the top show the spatial extent of the emission in narrow-band slices around the [O II], Hβ, [O III] and Hα, which tend to be the strongest optical emission lines. Here there is no [O II], as it out of the MUSE wavelength range for the fitted redshift. Below is the spectrum extracted within a 2 arcsec diameter aperture, which shows that this is likely a residual of the lens subtraction. The best fit redshift is 0.03735.

with an emitter detected within 6 arcsec with no observed counter-image. Large separation systems are those with an emitter outside of 6 but within 10 arcsec. Anything defined as multiple-imaged must have a typical lensing configuration and well-defined image redshifts. These are discussed further in the following chapter.

Table 4.1: The results of the MNELLS survey. We include the exposure time, galaxy redshift and absolute K_s magnitude. We state for each galaxy if there is a multiple– or single– imaged lensing system. Where either of these are possible, we report the distance to any emitters within 10 arcsec. We use 'large separation' to describe systems with an emitter more distant than 6 arcsec ($\sim 2\,R_{\rm Ein}$), but within 10 arcsec. Single-imaged denotes a galaxy with an emitter within 6 arcsec. J13522521-3456009, and J15105568-1128477 were only observed for a single exposure.

Galaxy (2MASX)	t_{exp}	z	K_{iso}^{2MASS}	Total Emitters	Single-Imaged	Ang. Sep. (arcsec)
J00031127-5444588	3060	0.03258	–25.456	22	large sep.	9.7
J00585131-1628092	3060	0.05408	–26.484	15	–	–
J01455353-0656086	3060	0.05229	–25.460	14	large sep.	7.6, 7.7
J02023082-5055539	3060	0.02148	–25.127	9	Yes	1.9,3.4,4.7,5.6,7.6,9.3
J03023835-6032198	3060	0.05425	–25.494	6	–	–
J05480837-4724177	3060	0.05166	–25.939	6	–	–
J11530823-3233574	3060	0.02712	–25.331	11	large sep.	9.7
J12332514-3121462	3060	0.05194	–26.395	19	Yes	5.1, 7.0, 7.1, 8.7
J13522521-3456009	1530	0.03824	–25.497	25	Yes	5.0,7.0
J15105568-1128477	1530	0.02495	–26.011	9	–	–
J18322937-6017262	3060	0.05170	–25.564	15	large sep.	7.2
J19163258-4012332	3060	0.01858	–25.676	7	large sep.	9.1
J19281700-2931442	3060	0.02432	–25.456	15	large sep.	6.6, 7.7, 9.3
J21075218-4710445	3060	0.01620	–24.969	5	large sep.	9.7
J21293744-2111443	3060	0.03563	–26.116	13	–	–
J23184637-1023575	3060	0.03170	–25.347	7	large sep.	6.6

Table 4.2: The results of our lens search within the MUSE archive. In the first column is the galaxy 2MASS ID, and in the second is the target object from the MUSE data header. For each galaxy we report the number of emitters, the exposure time, and if there is evidence for a multiple– or single– imaged lens system. The distance to the nearest emission line source within 10 arcsec is noted, or the distances to the multiple images. We also note two 'potential' systems which have single emission line detections which we do not find compelling.

2MASX	Target (header)	t_{exp}	Total Emitters	Multiply-Imaged	Single-Imaged	Ang. Sep. (arcsec)	Programme ID
J00561610-0115197	PGC003342	15660	39	–	large sep.	8.4	095.B-0127(A)
J01024177-2152557	LSQ13cmt	2805	5	–	–	–	099.D-0022(A)
J01145760+0025510	PGC004500	5180	12	–	Yes	4.7	094.B-0592(A),099.B-0242(A)
J01260057-0120424	3C040	1200	11	–	Yes	5.4	099.B-0137(A)
J02001493+3125457	NGC777	2700	20	–	–	–	097.A-0366(B)
J02021730-0107405	PGC007748	6390	20	–	Yes	3.5, 4.2	094.B-0592(A)
J02150461-2046037	SN2006ot	2220	8	–	–	–	095.D-0091(B)
J02431504+3225300	NGC1060	2700	15	–	–	–	097.A-0366(B)
J04333784-1315430	A0496	9000	38	–	–	–	094.B-0592(A),095.B-0127(A)
J04035024-0239275	LSQ13cwp	2805	22	Yes	–	1.17, 1.71	098.D-0115(A)
J05005065-3839169	LSQ12fvl	2805	1	–	–	–	099.D-0022(A)
J05571255-3728364	AS555	2700	17	Potential	–	–	094.A-0859(A)
J06004111-4002398	A3376	4680	20	–	large sep.	8.4	094.B-0592(A)
J06273625-5426577	A3395	16590	29	–	Yes	4.4	094.B-0592(A),096.B-0062(A)
J12542222-2900466	PGC043900	6840	10	–	–	–	097.B-0776(A)
J12571157-1724344	A1644	2700	7	–	–	–	094.A-0859(A)
J13232900-3150392	PGC046785	8280	33	–	large sep.	6.8	096.B-0062(A),097.B-0776(A)
J13240669-3140118	PGC046832	3240	25	–	–	–	096.B-0062(A),097.B-0776(A)
J13242275-3142239	PGC046860	2880	11	–	Potential	2.7	098.B-0240(A)

Table 4.2: Continued...

2MASX	Target (header)	t_{exp}	Total Emitters	Multiply-Imaged	Single-Imaged	Ang. Sep. (arcsec)	Programme ID
J13272961-3123237	PGC047154	3240	18	–	–	–	095.B-0127(A),096.B-0062(A)
J13275493-3132187	PGC047197	2880	12	–	–	–	095.B-0127(A),096.B-0062(A)
J13275688-3129437	PGC047202	1440	16	–	–	–	095.B-0127(A)
J13283871-3120487	PGC047273	5040	15	–	large sep.	7.1	097.B-0776(A)
J13292810-3133048	PGC047355	3240	19	–	large sep.	8.9	096.B-0062(A),097.B-0776(A)
J13303277-3134339	PGC047467	2880	19	–	–	–	098.B-0240(A)
J13312752-3149140	PGC099188	8640	27	–	–	–	098.B-0240(A),099.B-0148(A)
J13320334-3146430	PGC047590	5940	43	–	Yes	4.7	098.B-0240(A),099.B-0148(A)
J13333473-3140201	PGC047752	3960	19	–	large sep.	7.7	096.B-0062(A)
J13472838-3251540	PGC048896	13920	20	–	–	–	097.B-0776(A)
J14014186-1136251	PGC049940	2160	7	–	–	–	097.B-0776(A)
J14543146+1838325	A1991	2700	8	–	–	–	094.A-0859(A)
J15164448+0701180	A2052	7485	38	Yes	–	7.4, 13.2	097.B-0766(A)
J20515691-5237473	PGC065588	14310	41	–	–	–	097.B-0776(A),099.B-0148(A)
J23135863-4243393	AS1101	2700	16	–	Yes	3.6	094.A-0859(A)
J23363057+2108498	A2626	1800	7	–	Potential	3.5	095.A-0159(A)
J23570068-3445331	A4059	10080	33	Yes	–	8.6, 9.8	094.B-0592(A)

4.6 Summary

In this chapter, I introduced MNELLS and the MUSE archive search. These are two complementary searches for low-z strong lensing galaxies. Each target is selected to maximise the lensing cross-section and hence, the lensing-likelihood of a galaxy. The surveys use different proxies for galaxy mass, with MNELLS selecting galaxies with $\sigma > 300\,\mathrm{kms}^{-1}$, and the archival search using 2MASS absolute K-band magnitude as a proxy for stellar mass.

In ESO P101, 16 galaxies were observed for MNELLS. Of these, 14 were observed to full depth, (two observing blocks, totalling 3060s on source) and two at half depth. From the archive, 36 candidates were selected; however, the constraint removing cluster BCGs was relaxed. Although these systems poorly constrain the IMF, the same background emitters will be lensed, and so provide strong test cases for the detection method.

Each pipeline reduced data product was processed in the following manner. The candidate lens galaxy is filtered from the datacube in each spectral channel, and the residual is smoothed spatially and spectrally. This process can also remove other continuum sources in the frame. The residual datacube is then searched automatedly for emission line peaks which are extended in all three dimensions. Each detection is assigned a redshift, and then the detection catalogue is vetted by human inspection.

This chapter concluded with the results presented in Tables 4.1 and 4.2, which contain the complete list of detected and confirmed sources. The 'successes' can be separated into four detected gravitational strong-lenses and nine singly-imaged but close-projected systems. The next two chapters will analyse each of these cases to constrain the lensing M/L. The galaxy-scale lens J0403-0239 is discussed in Chapter 6. The other discovered potential lenses are analysed in the next chapter.

CHAPTER 5

MNELLS: The lenses and near misses

This chapter is based on the second half of *MNELLS: The MUSE nearby Early-Type Lens Locator Survey* (Collier et al., 2020).

5.1 Preamble

The previous chapter outlined the detection technique for distant emitters in MNELLS and the complimentary archival search. The numbers of detected emission line objects for each target are listed in Tables 4.1 and 4.2. There are three cluster-scale, and hence dark-matter-dominated, lensing systems (central galaxies of A4059, A2052 and AS555). For a further nine galaxies, there is a singly imaged but close-projected source detected within 6 arcsec, including one candidate with three sources at different redshifts. In this chapter, I present the lensing analysis of the cluster-scale lenses and infer upper limits on the mass-excess parameter for the singly imaged systems. To assess the MNELLS search method and test the detection threshold, simulated sources are injected into and recovered from the short-exposure MUSE observations.

5.2 Introduction

Zwicky (1937) first described how a nearby galaxy could act as a gravitational lens to a more distant source, and the resulting lensed images could be of sufficient size and surface brightness to be observable. The first discovered lensed images were a pair of quasars at $z = 1.41$ separated by 6 arcsec with near-identical spectra (Walsh et al., 1979). Recent lensing studies, with better characterised lens light profiles, provide key constraints on a wide range of astrophysical quantities, such as H_0, general relativity and the nature of dark matter (e.g. Wong et al., 2019; Collett et al., 2018; Ritondale et al., 2019).

Strong lensing measures the total mass, including dark matter (DM) as well as stars, projected within the Einstein radius ($R_{\rm Ein}$). In cases where the relative contributions of the two components can be distinguished, the stellar mass-to-light ratio (Υ) can be determined. This is particularly important when investigating the stellar initial mass function (IMF), which is a key component of galaxy evolution, and for interpreting observed properties e.g. estimating stellar masses. The IMF is probed via the mass-excess parameter (α)

$$\alpha = \frac{\Upsilon}{\Upsilon_{\rm Ref}} \tag{5.2.1}$$

which compares a measured Υ to a reference mass-to-light ratio ($\Upsilon_{\rm ref}$) for a modelled stellar populations with a fixed IMF. Disentangling the dark and stellar matter, in general, requires additional information which can in principle be determined from stellar dynamics (i.e. SLACS, Treu et al., 2010). However, this technique requires further modelling assumptions and appears to require the addition of Υ gradients to match similar measurements from weak lensing constraints (Sonnenfeld et al., 2018).

Low-z ETG strong-lenses are incredibly rare. There are only three confirmed at $z < 0.05$, and thse systems are uniquely applicable to investigating the stellar IMF (Treu, 2010; Smith et al., 2015). Within a galaxy, the stars are more centrally concentrated than the DM halo, e.g. a NFW halo (Navarro, Frenk & White, 1996). Lenses in which the $R_{\rm Ein}$ occurs at a fraction of the effective radius ($R_{\rm Eff}$) directly probes the stellar content of a galaxy. For low

redshift lenses ($z \leq 0.1$), the required critical density for forming multiple images is higher, (compared to the same lens, but more distant from the observer), and is therefore exceeded only at small physical radius where the stars contribute up to 80 percent of the mass.

For a galaxy within a cluster environment there is a 'boost' in the lensing from the cluster DM halo. This acts to increase the surface mass density, and hence exceed the critical density at larger radii (irrespective of the low-z nature of the lens). These systems are therefore significantly less useful for investigating the stellar content of a galaxy.

In this chapter, Section 5.3 discusses the three cluster-scale strong-lenses which were discovered during the search for galaxy-scale lenses. In Section 5.3.4, the 'near misses' are discussed. These systems have a close-projected but singly imaged source. Section 5.5, investigates the efficiency of the MNELLS search technique, and Section 5.5.3 presents possible improvements to the method.

5.3 Identified/Candidate Lenses

In this section we will detail the results of the line emission search on a total of 52 galaxies. The results are summarised in Table 4.1 for MNELLS, and Table 4.2 for the archival search.

We use three main criteria for any galaxy we label as a multiply imaged lens. The first is a secure redshift for each image, from either multiple consistent emission lines or a clear [O II] doublet. The second is a configuration which has a strong resemblance to theoretical lens systems modelled with a singular isothermal sphere (SIS) or singular isothermal ellipsoid (SIE) parametric model. The third is any velocity offset between each image must be small ($v_{\rm offset} < 100\,{\rm km\,s^{-1}}$), and similar emission line ratios. The presence of weaker, less commonly observed emission lines, (i.e O I, Hγ, Hδ, [Ne III] or He I) in both spectra are also strong indicators of a common source. For a close-projected single-imaged system, only the first criterion is relevant.

In the combined sample, four galaxies show evidence for double-imaged sources, with confirmation from multiple emission lines. These are 2MASXJ04035024-0239275 (here-after

J0403-0239), an isolated elliptical, (see Chapter 6), and three BCGs, from A4059, A2052 and AS555. These are 2MASX J23570068-3445331, 2MASX J15164448+0701180, 2MASX J05571255-3728364 respectively. Detailed discussion and analysis of these 'cluster-lenses' is presented in Section 5.3.1.

During our systematic search, we recorded separately any emitters discovered within 10 arcsec of the galaxy centres. For a given lens, the region on the image-plane within which a source can form multiple images is $2 \times R_{\rm Ein}$. For our sample, the typical $R_{\rm Ein}$ is 2–3 arcsec (for an isothermal sphere model with velocity dispersion 260–320 km s^{-1} and a source distant from the lens). We discovered nine galaxies with close-projected but apparently single-imaged sources within 6 arcsec. These galaxies are analysed to constrain the maximum lensing mass which produces no detectable counter-image, and hence the lens galaxy IMF ('Upper Limit Lensing' Smith, Lucey & Collier, 2018). We describe these close-projected systems in Section 5.3.4.

MUSE has a large 1×1 arcmin FoV. Within the datacubes, there are frequently clustered background emitters sharing a redshift. These are, in general, not lensed systems. In Section 5.3.2, we explain the criteria we use to exclude such systems.

5.3.1 Multiply imaged cluster lenses

In addition to J0403-0239, we discover multiply imaged sources behind two cluster BCGs (2MASXJ23570068-3445331 and 2MASXJ15164448+0701180). These detections are shown in Figures 5.1 and 5.2. We also report a third potential lens, 2MASXJ05571255-3728364, in Figure 5.3. These are each among the lowest redshift clusters known to have multiply imaged sources.

5.3.1.1 2MASX J23570068-3445331

The first candidate lens, J2357-3445, lies at $z = 0.0491$, and is the cluster BCG of A4059. This cluster lies at $z = 0.0487$, with a size of $R_{500} \simeq 0.96$ Mpc and a mass,

$M_{500} \simeq 2.67 \times 10^{14}\,M_{\odot}$ taken from the 'meta-catalogue of X-ray detected clusters of galaxies' (MCXC, Piffaretti et al., 2011). This cluster has been subject to multi-waveband observations, which could provide additional information to describe this lensing system. In *HST*/WFPC2 F814W imaging, (Choi et al., 2004), the presence of a dust lane is clear. Furthermore, large plumes of filamentary nebular emission at the cluster redshift (McDonald et al., 2010) is present in the MUSE data.

We detect two background emitters in the MUSE datacube separated by 17.15 arcsec which are at $z = 0.512$ (see Figure 5.1a). In the *HST* data, there is a very faint source coincident with image A, though it cannot be unambiguously determined as related. Though the separation is large, the spectra are similar, with consistent line ratios of [O III], Hβ and [O II], in Figure 5.1b,c,d. A strong suggestion of these sharing a common source, and not being two different background galaxies, is the presence of weak [Ne III] λ3869 and He I λ3888 lines, which are present in both spectra with similar line ratios. Neither of these lines is commonly observed in galaxy spectra, hence these images are likely to originate from a single background source. Image A appears slightly extended, which cannot be ruled out to be present in image B. Due to the small velocity offsets, and rare emission lines, this system is labelled a lens.

The very large angular separation means J2357-3445 is a weaker tool for investigating the IMF, as additional information is required to disentangle the dark and stellar matter once the lensing mass is estimated. Indeed, in such an environment, it is expected the cluster DM will dominate the lensing mass.

Fitting an SIE profile to images A and B, measures a lensing mass within the half image-separation of $1.79 \times 10^{12}\,M_{\odot}$. This is over six times larger than expected from the stellar mass alone, for a MW-like IMF, which indicates that DM is likely dominating the lensing mass. A more detailed discussion is presented in Section 5.4.1.

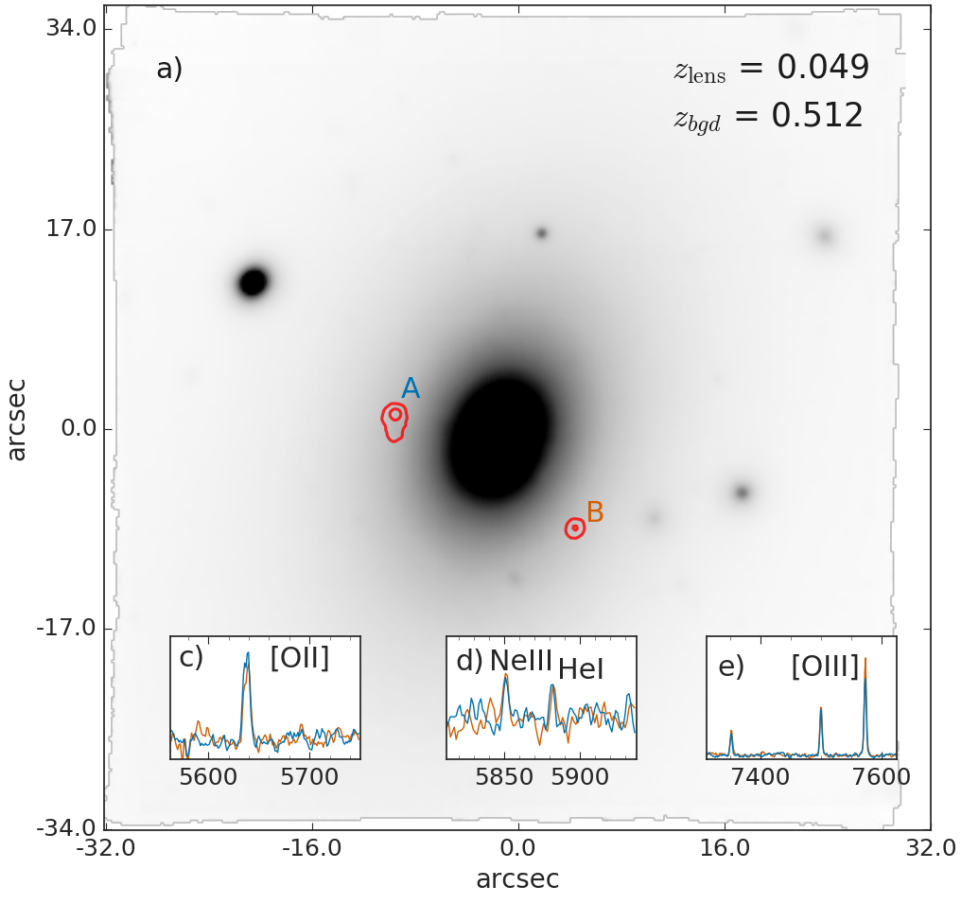

Figure 5.1: The MUSE data for the BCG J2357-3445, and the extracted spectra of the multiply imaged background emitter. Panel a) The MUSE data, collapsed over the full wavelength range, for J2357-3445. Contours at the peak [O III] emission for the background emitters are displayed in red. Panel b), c) and d) show the emission from the two images with their negligible velocity offset in [O II], [Ne III], and [O III] respectively, which confirm the single source of origin.

5.3.1.2 2MASXJ15164448+0701180

J1516+0701 is a massive elliptical galaxy, at $z = 0.0345$. It is the BCG of A2052 ($z = 0.0355$), which has an X-ray measured M_{500}, and R_{500}, of 2.5×10^{14} $M_{\odot}$ and 0.95 Mpc (Piffaretti et al., 2011) respectively. There is some extended emission in the datacube, indicating that this is an active galaxy, and complicating the detection of background objects.

The pair of emitters lie west-east in Figure 5.2a, and are separated by 19.4 arcsec. The closest image, A, is located 7.4 arcsec west, and B is 13.2 arcsec east from J1516+0701, and they are separated by $< 50\,\mathrm{km\,s^{-1}}$ in velocity space. The emitters were detected from the [O II] doublet at $z = 1.376$, see Figure 5.2b. There are no other spectral lines in the MUSE wavelength coverage. Both images appear to share the same structure, with two distinct clumps in A, and potentially the same in B. There are archival *HST* observations (WFPC2 F814W, 6500s; PI:Geisler) however we cannot detect any obvious counterparts to the MUSE detections. Due to the similar extended structure and clear doublet in image B, we label this a strong-lensing system.

This system is similar to J2357-3445, being located in a cluster environment, however the extended emission maybe indicates the presence of star formation or an active galactic nuclei. This makes the system even more complex for investigating the IMF as selecting a reference mass-to-light ratio (Υ_{ref}) is more uncertain.

From SIE paramaterised lens-modelling, the mass within half the image separation is 1.65×10^{12} $M_{\odot}$. This is seven times larger than expected from a stellar population alone from a MW-like IMF. Therefore the lensing mass for the galaxy probably has a significant contribution from DM. A more detailed discussion is presented in Section 5.4.1.

5.3.1.3 2MASXJ05571255-3728364

The final and least secure cluster candidate is J0557-3728, the BCG of AS555, which lies at redshift 0.0448. The cluster has a redshift, $z = 0.0440$, with an X-ray measured M_{500}

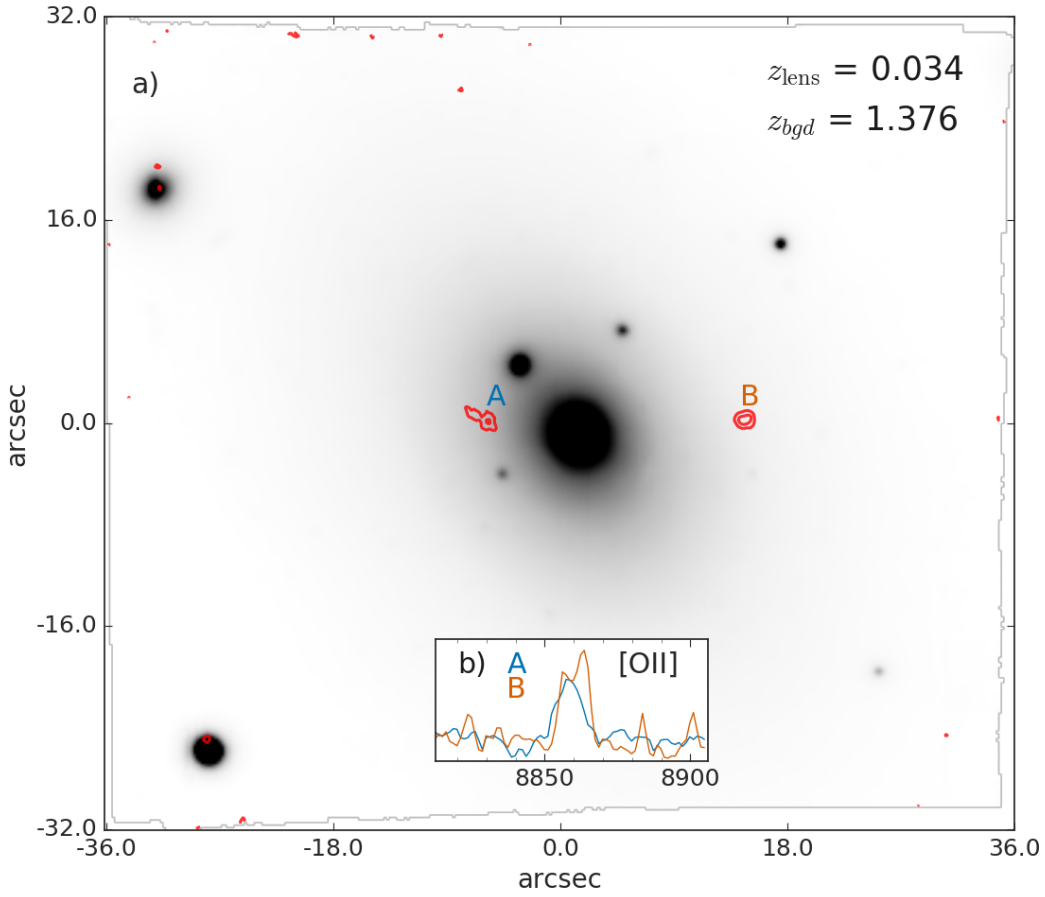

Figure 5.2: The MUSE data for the BCG J1516+0701, and the extracted background emitter spectra. Panel a) The MUSE data for J1516+0701 collapsed over the full wavelength range, with red contours denoting the position of the $z = 1.377$ background emitters. Panel b) The [O II] emission from images A and B overlaid. There is very little velocity offset, however A only hints at a complete doublet structure. The structure in image A cannot be ruled out in image B.

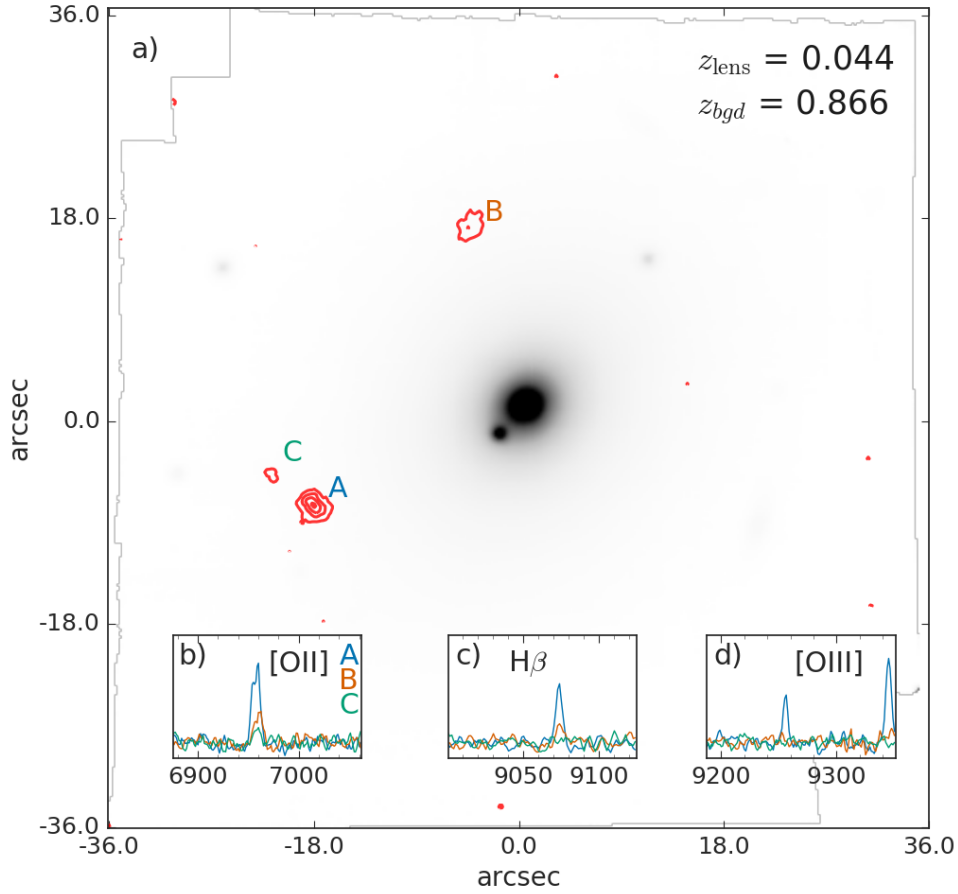

Figure 5.3: The MUSE data for the BCG J0557-3728, and the extracted background emitter spectra. Panel a) The MUSE data for J0557-3728 collapsed over the full wavelength range which shows the close, small companion galaxy. Overlaid on top are the contours of the [O II] emission for the candidate lensed images. Panels b), c) and d) show the strongest emission lines from the three clumps labelled in a).

and R_{500} of 0.97×10^{14} $M_\odot$ and 0.69 Mpc (Piffaretti et al., 2011). There is a significantly smaller companion galaxy separated by ~ 3.2 arcsec, but no similarly sized nearby galaxies within 2 arcmin. The emitters were discovered via strong [O II] emission, at redshift 0.87. However, the candidate lensed images do not follow a classic lensing configuration, A is located 20.7 arcsec south-south-east, with C only 3 arcsec further, and B is located 16.2 arcsec north, meaning that the images do not intersect the lens galaxy. There is a small velocity offset of 80 km s^{-1} between A and C, and between B and C. We tentatively label this system as a lens.

This system is significantly more complex than the previous two cluster lenses, and the exposure time was relatively short (2700 seconds) which limits the detection of faint

sources. The surrounding environment does not appear to suggest that a large external shear is the cause of the non-standard configuration. One potential explanation could be that J0557-3728 is offset from the centre of the AS555 cluster DM. An alternative explanation originates from the line strength ratios between the different images, Figure 5.3b,c,d. Common lines (i.e. Hβ and [O III]) are stronger, and weaker in varying ratios between the three images. This may be due to differential magnification of components of a single source. This may be explained by the source is crossing a caustic line, and the existence of image C potentially adds evidence for this explanation, as it may be part of image A. Due to the complex nature of this system, and few constraints, we do not attempt to model this system for the purpose of constraining the IMF.

Further data for J0557-3728, such as deeper MUSE observations, could help to confirm the lensing configuration. Additional faint counter-images could be ruled out or confirmed. These can further constrain this system.

5.3.2 Multiple close emitters

Within any search for multiply imaged lensing systems, there will be cases for which the observations do not provide conclusive evidence. Often the distinguishing features between a lensing and non-lensing interpretation require significant case-by-case analysis. As summarised in Section 5.3 the three main criteria are the redshift quality, the lensing configuration, and the velocity offset between images. To illustrate the decision process we show two examples of rejected systems, one in Section 5.3.3, and the other in Section 5.3.4.8. We provide an explanation of the evidence which led to them being rejected. The first case is rejected due to a significant velocity offset and varying line ratios. The second is excluded as there is no apparent counter-image, and the sources are located outside of the expected multiple-imaging regime.

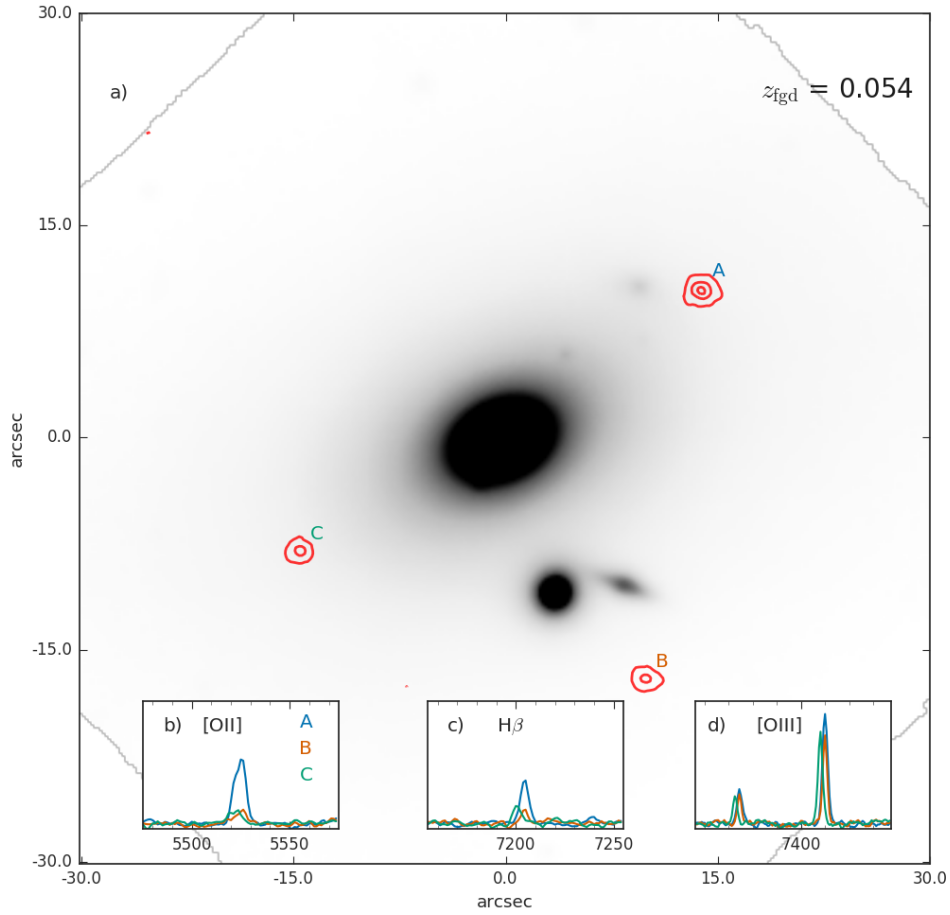

Figure 5.4: The MUSE data of J0058-1628, and the extracted background emitters. Panel a) The MUSE data of J0058-1628 collapsed over the full wavelength range, overlaid with contours of the background [O III] emission at common redshift, labelled A, B and C. Panels b,c,d) displays the [O II], H β and [O III] emission for each of the three emitters. The line strength ratios vary between the images, with very weak [O II] emission only present in image A. Image C can be seen to have a velocity offset compared to A and B, in all three panels. Therefore we do not consider these to have originated from a single source.

5.3.3 2MASXJ00585131-1628092

J0058-1628 is a redshift 0.054 massive elliptical with a companion separated by 11.5 arcsec. This system was previously observed with SINFONI, however, due to the small FoV of the instrument, three background clustered [O III] emitters were outside of the instrument FoV. However, in MUSE these emitters are detected, and shown in Figure 5.4.

The three emitters share very strong [O III] emission, but do not share the same [O II], and H β. There is also a significant velocity offset $\sim 200\,\mathrm{km\,s^{-1}}$ between C and the

other two, but only 10's km s^{-1} between A and B, seen clearly in Figure 5.4d). On face value, considering the images A and B the system appears similar to J2357-3445, which we label a lens. In this case, the candidate images are separated by ~28.28 arcsec, and > 15 arcsec from the galaxy centre, which far exceeds the stellar galaxy-galaxy lensing regime. However, this lens does not appear to be part of a larger galaxy group, and hence is unlikely to have the large dark matter halo required to have such large image separation (unlike J2357-3445). Finally, there is a weak Hγ line, seen in candidate image A, which is not seen in the spectrum of candidate B.

Therefore we label this system as a clustered group of background sources, and not a lensing system. Deeper observations and a more detailed understanding of the local matter distribution would be required to clearly define this system.

5.3.4 Singly-imaged candidates

Although multiple-image systems provide the strongest constraints, there is also information in estimating upper-limits for M/L of a lensing system in which only a single closely-projected emitter is detected (e.g. Shu et al., 2015; Smith et al., 2018). Accounting consistently for such systems can help mitigate lensing selection bias. Here, we follow the Smith et al. (2018) methodology, but with a larger and more uniform sample. We select singly imaged, but closely projected 'lenses' as those galaxies with an emitter within 6 arcsec of the galaxy centre, shown in Table 4.1 and 4.2. Within our dataset we discovered nine such candidates. Each detection is visually inspected in the spatial and spectral domain to confirm the emission lines. Each of the nine (six and three from the archival and targeted searches respectively) candidates is displayed in Figure 5.5, and are summarised in Table 5.1. These are the best candidates for single lensing analysis. We exclude 2MASXJ23363057+2108498, and 2MASXJ13242275-3142239 which each have sources within 6 arcsec in Table 4.2. In each of these cases the source only has a single line detected which we do not find compelling (due to the lack of clear [O II], or Lyα structure), and therefore do not have a confidently identified redshift.

In this subsection we outline each candidate, and then in Section 5.4.2 show the upper-limit lensing analysis results and make comment on whether any of these systems are promising candidates for follow-up observations.

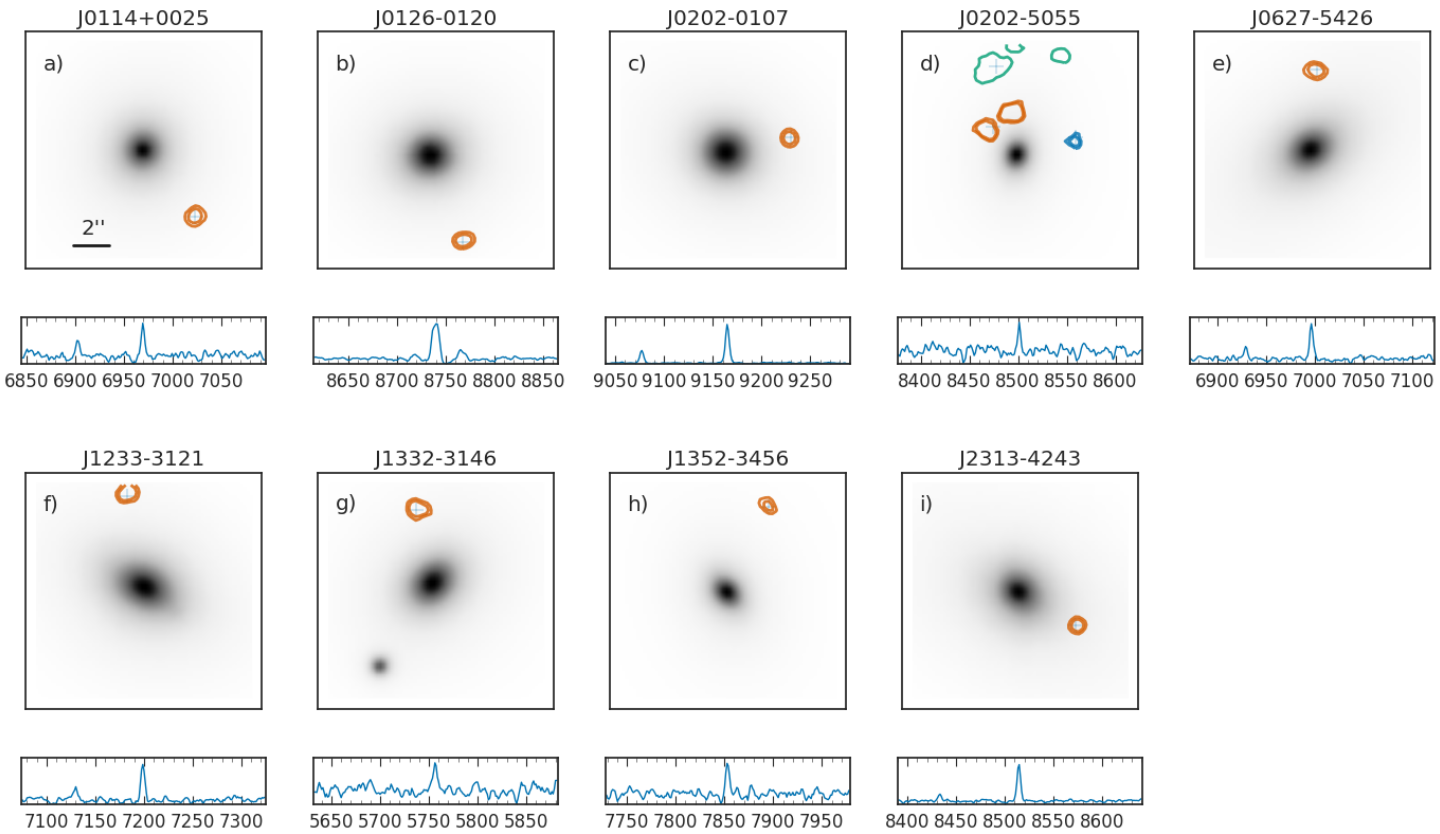

Figure 5.5: The single-imaged systems as described in Section 5.3.4. Each frame consists of the collapsed MUSE datacube across the full spectral range, overlaid with a orange contour of the brightest peak of emission for the single-imaged closely projected background emitter. All panels have the same scale, and are 12×12 arcsec. Underneath each MUSE frame is the spectrum extracted at peak of the emission, and only with the brightest peak/doublet shown. In the majority of cases this is the [O III] doublet. In the case of J0202-5055 we show all three emitters, the smallest angular separation in orange, then blue, and then green (The green contours have multiple regions, as there is a group of clustered emitters at the same redshift).

Table 5.1: The single-image candidates. For each galaxy we list the galaxy redshift, the redshift of the background source, and the separation in arcsec. The position angle is denoted in degrees north through east.

Galaxy (2MASX)	z_{gal}	z_{bgd}	Separation (arcsec)	Position Angle (degrees)
J01145760+0025510	0.04490	0.390	4.70	–141.8
J01260057-0120424	0.01824	0.332	5.39	–164.9
J02021730-0107405	0.04276	0.830	4.20	–103.0
J02023082-5055539	0.02148	0.295 (1.29, 0.907)	1.92 (3.37, 4.68)	50.0 (–78.0,–27.3)
J06273625-5426577	0.04856	0.3971	4.40	–2.5
J12332514-3121462	0.05194	0.4374	5.14	11.7
J13320334-3146430	0.04372	0.890	4.24	–102.7
J13522521-3456009	0.03824	0.1962	5.06	–23.5
J23135863-4243393	0.05640	0.700	3.60	–119.2

5.3.4.1 2MASXJ01145760+0025510

The BCG of A0168, J0114+0025 has $z = 0.04490$ ($\Delta v_{\rm cluster} = 70\,{\rm kms}^{-1}$). The observation is an archival MUSE-DEEP datacube with a PSF of 1 arcsec. MCXC X-ray data (Piffaretti et al., 2011) tabulates the cluster R_{500} at 0.75 Mpc, and $M_{500} = 1.25 \times 10^{14}\,{\rm M}_{\odot}$. The background emitter is separated by 4.7 arcsec to the south-west, and so is likely at the outskirts of the strong-lensing regime. The collapsed MUSE datacube is shown in Figure 5.5a with the emitter position overlain as a contour. In the spectrum, the emitter is clearly visible from its [O III] and H β, along with weaker [O II] and H α at $z = 0.39$.

In addition to the nearby emitter, there is a second [O II] source at $z = 0.82$ separated by 9.4 arcsec. We do not consider this in our lensing analysis due to the large separation. There are also a further three clustered [O III] emitters, at redshift ~ 0.39. They are offset from the single closely-projected emitter by $> 200\,{\rm kms}^{-1}$, and so did not originate from a common source. Furthermore the three clustered emitters are unlikely to share a single source, as two are offset in velocity space by $\sim 60\,{\rm kms}^{-1}$, and they are located 23.5 arcsec north and 23 arcsec west respectively.

5.3.4.2 2MASXJ01260057-0120424

J0126-0120 is a massive ETG ($\sigma_{\rm 6dF} = 262\,{\rm kms}^{-1}$) with a nearby companion separated by 30 arcsec (the BCG of A0194). The datacube PSF is 0.7 arcsec. It has a redshift of 0.0182 and has a velocity offset to the cluster of $\Delta v_{\rm cluster} = 72\,{\rm kms}^{-1}$. A0194 has a R_{500} 0.516 Mpc,

and $M_{500} = 0.40 \times 10^{14}\,\mathrm{M}_{\odot}$ (Piffaretti et al., 2011). The background emitter is separated by 5.4 arcsec to the south-west (see Figure 5.5b), and has a measured redshift of 0.332. The stellar population of this galaxy was previously studied with the Mitchell IFS data, finding radial metallicity gradients in [α/Fe] and [Fe/H] (Greene et al., 2019).

5.3.4.3 2MASXJ02021730-0107405

This system was previously reported in Smith et al. (2018).

J0202-0107 (PGC007748) is the BCG of A0295, and located at redshift 0.04276 ($\Delta \mathrm{v}_{\mathrm{cluster}}$ = 119 kms^{-1}). The datacube has a PSF of 0.8 arcsec. This galaxy has a redshift 0.83 emitter separated by 3.5 arcsec to the north-west, see Figure 5.5c. The strongest emission line is [O III]. A0295 is a poor cluster with $M_{500} = 6.0 \times 10^{13}\,\mathrm{M}_{\odot}$. Therefore the DM will have significantly less of an impact on the lensing mass for this system compared to other, larger clusters, i.e. AS1101, A3395 and A0168. There is a second similarly separated background source 4.2 arcsec to the north west ($z = 0.83$), however as the direction is very similar we will only consider the closer image which will provide stronger constraints.

5.3.4.4 2MASXJ02023082-5055539

J0202-5055 is a $z = 0.02148$, massive ETG ($\sigma_{\mathrm{6dF}} = 323\,\mathrm{km\,s}^{-1}$). The closest source is separated by only 1.92 arcsec north-east from the galaxy centre, see Figure 5.5d. This source lies at redshift 0.295, and has a velocity gradient. It was identified from [O II], [O III] and H α emission lines.

This system also contains another four background emitters, closely projected to the lens. Separated by 3.37 arcsec to the west is a faint [O II] emitter at $z = 1.289$. This potentially offers an additional constraint on the mass profile of J0202-5055. A further group of three emitters lies to the north, with a redshift of 0.907 from strong [O II] and H β (the closest separated by 4.68 arcsec).

J0202-5055 was observed with SINFONI by Smith et al. (2015) as part of the SNELLS survey, and only the $z = 1.289$ emitter is hinted at, close to the frame edge. The new MUSE

data uncover a much more complex system, which is potentially a powerful target for future observations, aiming to uncover any counter images to the $z = 0.29$ and $z = 1.29$ sources.

5.3.4.5 2MASXJ06273625-5426577

J0627-5426 is the BCG of A3395, at $z = 0.04856$, with a velocity dispersion of $\sigma = 276$ km s^{-1} (Smith et al., 2004). It is offset from the cluster by $\Delta v_{\rm cluster} = -519$ kms^{-1}. We use the combined MUSE-DEEP datacube with a seeing of 1.0 arcsec. MCXC X-ray data reported R_{500} as 0.930 Mpc, and $M_{500} = 2.40 \times 10^{14}$ M$_\odot$. Separated by 4.40 arcsec to the north, we detect the emitter with strong [O II], Hβ, [O III] and Hα, at $z = 0.3971$, shown in Figure 5.5e. The is no obvious counterpart to this source in shallow *HST* observations (Laine et al., 2003).

5.3.4.6 2MASXJ12332514-3121462

J1233-3121 is a massive ETG with a 6dFGSv velocity dispersion measured to be $\sigma_{\rm 6dF} = 348$ km s^{-1}, and at $z = 0.05194$. The background emitter is distant, at 5.14 arcsec, (still within the predicted 2 $R_{\rm Ein}$ for such a high σ system), located to the north of J1233-3121, see Figure 5.5f. The emitter's spectrum is contaminated by foreground Hα and [SII] emission from the lens galaxy. However, the spectrum is well fit with [O II], [O III] and Hβ at $z = 0.4374$, separate from the lens contamination.

5.3.4.7 2MASXJ13320334-3146430

J1332-3146 has a redshift of $z = 0.04372$, and a close star (5.3 arcsec) located to the south-east. Otherwise its local neighbourhood is sparsely populated, although it lies in a fairly dense region of the Shapley supercluster (Haines et al., 2018). The background emitter is unresolved and separated by 4.24 arcsec to the west, and is detected via its [O II] line at $z = 0.89$, see Figure 5.5g. This system also contains three additional $z \sim 0.89$ emitters, all of which also lie significantly more distant from the galaxy centre to the west (≥ 9.34 arcsec). These will not be included in the analysis due to their respective distance, and as they

are not consistent with a multiply imaged lensing scenario due to a combination of their velocity offsets, image separation and orientation from J1332-3146.

5.3.4.8 2MASXJ13522521-3456009

J1352-3456 is an E/S0 galaxy ($\sigma_{6dF} = 341\,\mathrm{km\,s^{-1}}$) with no nearby galaxies of comparable size, at $z = 0.03824$. The background emitter is separated by 5.06 arcsec, to the north-west, and has $z = 0.1962$ from H α and [O III] emission (see Figure 5.5h).

This system also includes three emitters within 6.9–7.5 arcsec (See Table 4.1), which are not multiply imaged but are of a similar redshift, all to the south. These are detected at redshift ~ 0.549, via strong [O III] and weaker [O II]. A fourth emitter can be seen in Figure 5.6a) to the south, but is poorly configured with the other three sources, and has a velocity offset of $210\,\mathrm{km\,s^{-1}}$ so is not considered part of the candidate lens system.

The spectra of the three objects are very similar, with A and C of comparable line strengths, and B the faintest. The largest velocity offset is between A and C, and is $\sim 90\,\mathrm{km\,s^{-1}}$, with B and C offset by $< 50\,\mathrm{km\,s^{-1}}$. However, in this system the problematic feature is the distance from the lens to the images, and the separation between the images. Were these images close, and hint at a some linked structure this may bear a resemblance to the lens reported in Smith (2017), with a large arc, and no clearly observable counter-image. However, no evidence is present to define this as an arc. The separation from the lens of ~ 6.5 arcsec lies at the limit of twice the expected $R_{\mathrm{Ein}}$for a similarly massive galaxy and hence unlikely to lie within the strongly lensing regime. Secondly to form three distinct images, each separated by over 1 arcsec is an unlikely lensing configuration. In addition there is no evidence for these candidate images forming a single arc, as no emission is detected in the spaces between C, B and A.

In order to understand this lensing system much deeper data would be required to test for the presence of a faint inner image, very close to the candidate lens core, or to identify C, B and A as a single arc. Furthermore these potential images lie at a distance which would only add weak constraints to the required mass for there to be no detectable counter image.

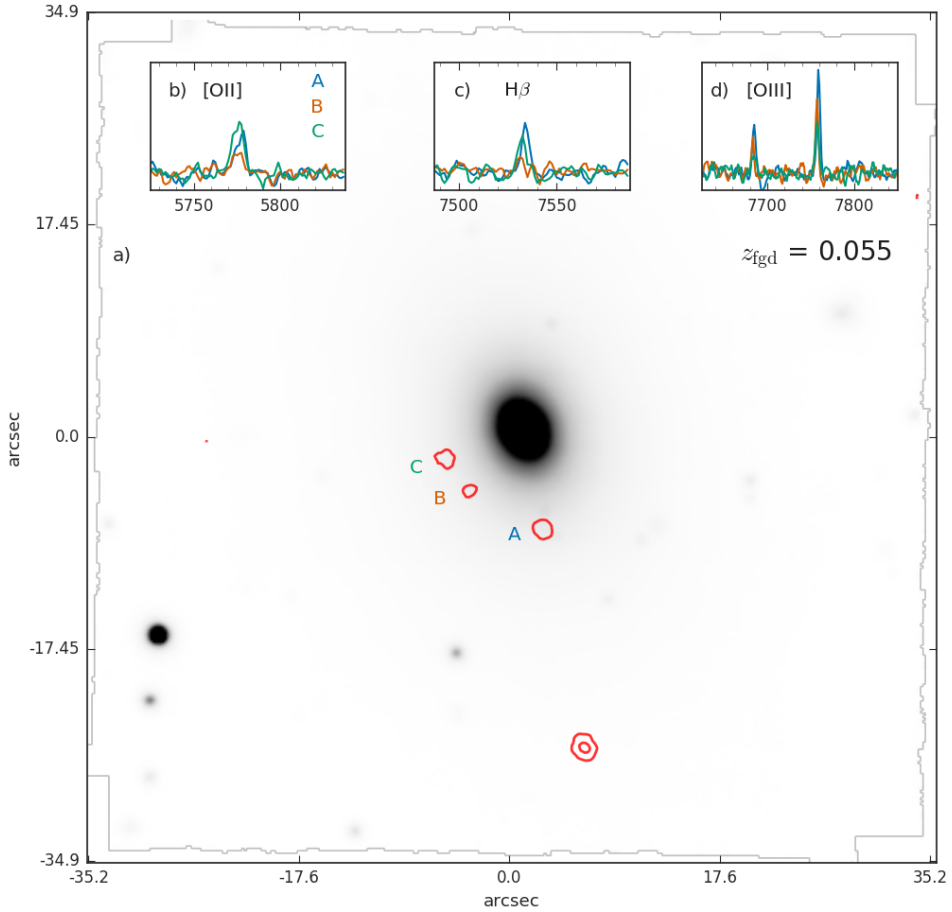

Figure 5.6: The MUSE data of J1352-3456, with the extracted background emitters spectra. Panel a) The MUSE imaging of J1352-3456 collapsed over the full wavelength range. Overlaid are the contours of the [O III] emission for the rejected candidate lensed images. Panels b,c,d) show the [O II], H β and [O III] respectively for each of the labelled emitters. The line strength ratios vary, between images A and C, along with all three being offset in velocity space from each other (seen most clearly in panel c), H β).

Hence, we label these emitters a group of background galaxies.

5.3.4.9 2MASXJ23135863-4243393

The BCG of AS1101, J2313-4243 lies at $z = 0.05640$ ($\Delta v_{cluster} = -480\,kms^{-1}$), and, as shown in Figure 5.5i, has an emitter separated by 3.6 arcsec to the south-west. The strongest emission is [O III], along with weaker H β and [O II] which is fit at $z = 0.700$. AS1101 has X-ray data from MCXC measuring R_{500} as 0.980 Mpc, and $M_{500} = 2.83 \times 10^{14}\,M_{\odot}$ which is similar to A3395.

5.4 Lensing Analysis

5.4.1 Multiply imaged cluster-scale systems

These cluster-scale strong lenses can only provide relatively poor constraints on the IMF, due to the large image-separation. Here we derive some initial quantities from purely strong lensing analysis for J2357-3445 and J1516+0701 from Sections 5.3.1.1, and 5.3.1.2, without attempting to disentangle the DM from the stellar matter.

For each of the two systems we model and optimise the mass profile with GRAVLENS to reproduce the image positions, and then estimate the DM contribution as the stellar mass, converted from the aperture luminosity with a Kroupa or Salpeter IMF, to the total mass from lensing. We model both galaxies with a SIE parameterisation, and fix the ellipticity and position angle to the light profile; the normalisation is left to vary. In order to account for extra complexity in the mass model, we include an external shear, with free parameters for the direction and amplitude, which will act as a proxy for the effects of the galaxy DM halo, and external structure in the cluster.

We then compare the lensing masses, within the half-image separation (see Table 5.2), to Υ_{ref} for Kroupa and Salpeter IMFs (assuming an old stellar population with solar metallicity), to estimate f_{DM}. (We measure the luminosity within the Einstein aperture

Table 5.2: The lensing analysis of the two cluster-scale lenses. The quoted masses are *total* lensing masses, including dark matter. The luminosity is Ks band 2MASS for J2357-3445, and WFPC2 F814W and 2MASS Ks for J1516+0701 The uncertainty is 0.1 arcsec for $R_{\rm ap}$. This follows through into the aperture mass as a 10 per cent uncertainty, and into the aperture luminosity as 2 per cent. We estimate that the uncertainty in the dark matter fraction is ∼5 per cent.

Name	band	$R_{\rm ap}$ (arcsec)	$M_{\rm ap}$ (10^{10} M$_\odot$)	$L_{\rm ap}$ (10^{10} L$_\odot$)	$\Upsilon_{\rm ref}$	mass-excess (α)	$f_{\rm DM}^{\rm Kroupa}$	$f_{\rm DM}^{\rm Salp}$
J2357-3445	Ks	8.5	179	28.34	0.96	6.56	85	76
J1516+0701	Ks	9.7	165	24.22	0.97	7.02	86	78
	F814W			8.84	2.66	6.99	86	78

with 2MASS Ks band data for both systems, and higher resolution *HST* WFPC2 F814W data for J1516+0701.) J2357-3445 requires a dark matter contribution of 76 per cent even for the higher stellar mass Salpeter IMF. Likewise J1516+0701 requires a 78 per cent DM contribution to have a stellar population comparable with a Salpeter IMF. Hence for any plausible IMF, the lensing mass is dominated by the DM rather than the stars. This highlights the importance of finding lenses for which the $R_{\rm Ein}$ probes the most central most stellar dense regions of the lens. The M/L derived from higher resolution *HST* WFPC2 F814W data, is in close agreement with that measured from the lower quality 2MASS data (see Table 5.2).

5.4.2 Single-image galaxy-scale systems

Whilst a multiple-image system provides the strongest constraints on the IMF, there is information stored in systems with only a single, close-projected emitter. In these cases we can constrain the M/L of the 'lens' as having to be consistent with mass profiles which does *not* produce a detectable counter-image. In turn, this translates to a maximal mass-to-light ratio excess parameter (α), and hence adds further constraints on the IMF in ETGs.

Here we present the analysis of the nine identified single-imaged close-projected systems. In order to be self-consistent we try to select a common source of K_s-band imaging for all candidates. The highest resolution data for this purpose is from the VISTA Hemisphere Survey (McMahon et al., 2013). Only J0627-5426 is not covered by VISTA. For this target we take the poorer resolution imaging from the 2MASS survey (Jarrett et al., 2000). The

average image PSF FWHM for the VISTA data is 1 arcsec, and for 2MASS is 3 arcsec. We derive all of our quantities in the K_s-band, using the Vega solar absolute magnitude quoted by EZGAL (Mancone & Gonzalez, 2012) for the 2MASS K_s-band in their filter list ($M^{\odot}_{K_s} = 3.295$).

We perform our lensing analysis with GRAVLENS (Keeton, 2001), using pixelised mass maps derived from the light profile of each galaxy. The mass profile is well traced by the light at scales comparable with, or smaller than, the $R_{\rm Eff}$. The central 7 arcsec of each galaxy is fit with a single Sérsic profile using GALFIT (Peng et al., 2010), fixing only the sky. Then the de-convolved model is converted into a pixelised mass map (with a fiducial scaling of $M/L = 1$). The mass maps are input to GRAVLENS and a range of shear (γ; 0–0.2) and shear position angles (θ; 0–180 deg) are applied for each scaling of M/L (M/L; 0.5–3.0). We select prior on the rms for each Cartesian shear component to be $s = 0.05$ as these are galaxy lenses without significant nearby mass distributions.

The mass maps are used to generate a grid of lensing models constrained by the position of the observed emitter. Then the number of detectable counter-images to the observed image is extracted. Following the framework outlined in Smith et al. (2018), we estimate the probability that the system only has a single detected image, for each trial value of M/L. The results are shown in Figure 5.7, with the *intrinsic* multiplicity curves showing the lensing regimes as we move from low to high M/L.

The curves display the regimes in which the background emitter is intrinsically singly imaged, then doubly imaged, quadruply imaged and then returns to doubly imaged as the source position required to recreate the observed image moves across the caustic lines on the source plane. Additionally we show the likelihood of there being no *detectable* counter image for each M/L bin (i.e. including the systems which are intrinsically multiply imaged, but where the counter-images are expected to be too faint to detect). We establish the S/N limits for an undetectable counter-image by re-inserting the detected source at random positions close to the foreground galaxy with different flux scalings. Each image is then visually inspected to determine whether the source would be recovered.

As all of our quantities are derived in the K_s-band, we can interpret the results with regards

to a different choice of IMF via the mass-excess parameter, $\alpha = (M/L)/\Upsilon_{\rm ref}$. We compare the measured M/L to a plausible range of $\Upsilon_{\rm ref}$ under the assumption of an old, metal rich population typical of early-type galaxies, and adopting a Kroupa IMF. Using the Conroy et al. (2009, hereafter C09) models accessed with EZGAL, for populations of metallicity $1-1.5\,Z_{\odot}$, and formation age 10–12 Gyrs, the sample galaxies have K-band $\Upsilon_{\rm ref}$ in the range $0.9 < \Upsilon_{\rm ref} < 1.1$.

Our choice of the C09 models leads to a subtle difference between this work and Smith et al. (2018), who used models from Maraston (2005). The $\Upsilon_{\rm ref}$ for a Salpeter IMF tabulated by C09 and M05 agrees to within a few per cent in the 2MASS Ks-band, (for old populations with solar metallicity) (see Mancone & Gonzalez, 2012). However, due to different treatments of the low-mass stars and the intrinsic uncertainty in the passive luminosity evolution of a galaxy, the ratio of $\alpha_{\rm Kroupa}$ and $\alpha_{\rm Salpeter}$ is different by ~ 8 per cent. Therefore in this paper for a result in agreement with a Salpeter IMF, $\alpha_{\rm Kroupa} \simeq 1.64$, instead of $\simeq 1.52$. Secondly, and key, is the adopted solar absolute magnitude. The K-band tabulated by M05 relates to the Johnson-Cousins K, used in Maraston (1998, hereafter M98), prior to the advent of the 'short' K (i.e. Ks) filter which dealt better with zero point issues due to H_2O in the atmosphere (see Bessell, 2005). Hence, the M98 $M_{\rm K}^{\odot} = 3.41$, is 0.115 mags offset from $M_{\rm Ks}^{\odot} = 3.295$, and this leads to a 11 per cent decrease in the derived luminosity when the correct value is used.

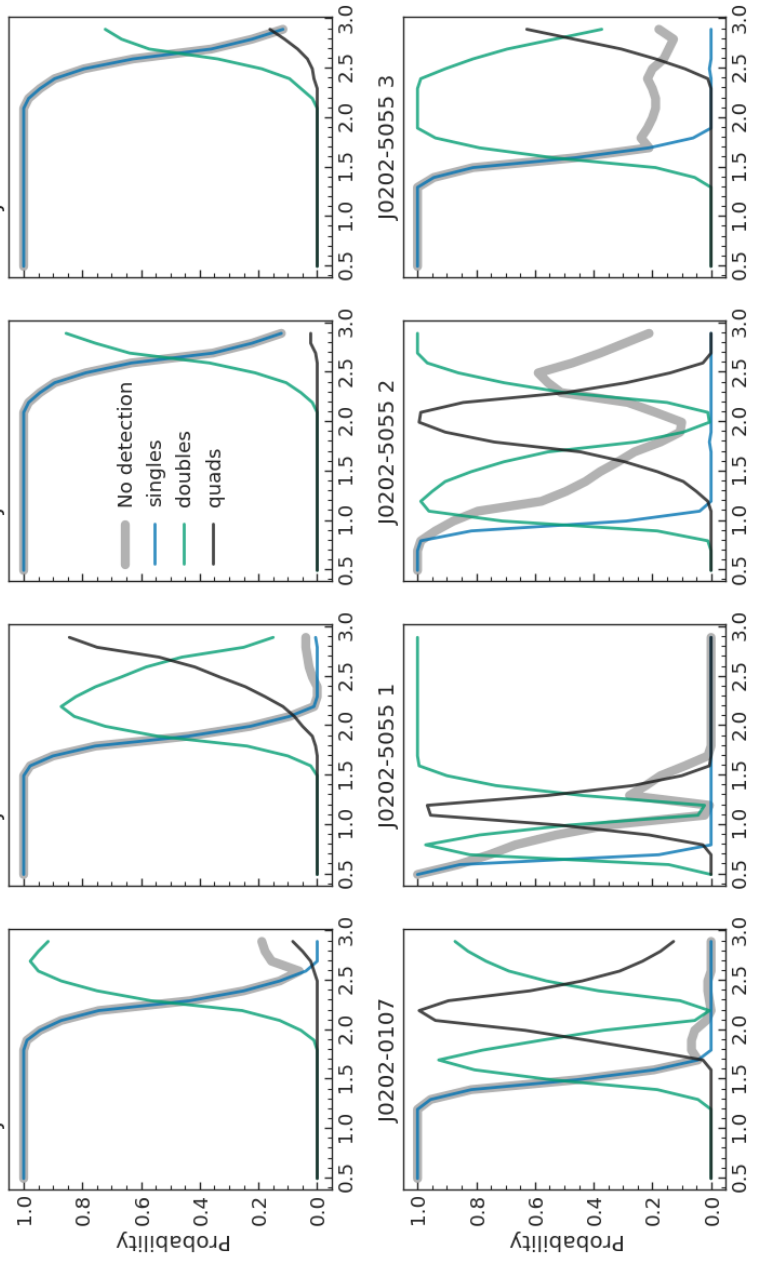

Figure 5.7: Upper-limit results for six galaxies with a single closely-projected image, plotted as probability against K_s-band mass-to-light ratio (M/L). The grey lines denote the probability of *not* detecting a counter-image in each case. The blue/green/black lines are the fraction of intrinsic singles/doubles/quads within each M/L bin as the requirement to reproduce the observed image is met. These range from producing multiple images only at the highest of M/L, J1332-3146, to J0202-5055 which for even low M/L there are many more intrinsically multiply imaged systems. The systems J0202-0107 and J0202-5055 are constrained to have the lowest M/L in the sample. J0202-5055 has panels 1/2/3 representing the $z = 0.295$, 1.289 and 0.907 sources.

For several galaxies in this sample, the background emitter is not multiply imaged within the full range of M/L and is therefore excluded from any further analysis (J0126-0120, J0627-5426 and J1352-3456). In addition, from those presented in Figure 5.7, J2313-4243, J1332-3146, J0114+0025 and J1233-3121 are each single-imaged at masses larger than predicted by a Salpeter IMF ($M/L = 1.6$). Therefore we do not make further comment on these systems in this section. However, the systems are included for investigating the ETG population in an ensemble sense, in Section 7.4.

We will now convert from M/L to α for the two galaxies with the strongest constraints (J0202-0107, J0202-5055). This conversion uses $\Upsilon_{\rm ref}$ from C09 for an old population, typical for low-z ETGs. This therefore sets a MW-like IMF to have $\alpha = 1.0$, a Salpeter IMF to have $\alpha = 1.64$ and we define a "heavyweight" IMF with $\alpha = 2.0$. We do not model the contribution from DM within the lens galaxies, therefore the α measurements are slightly overestimated. The current low-z lenses have a correction of about 20 per cent (Smith et al., 2015; Collier et al., 2018a). A system which is expected to form multiple images with a relatively light (i.e. Kroupa) IMF is a promising candidate for deeper follow-up, as the observational depth is likely to be the limiting factor. In the following subsections, 5.4.2.1 and 5.4.2.2 we will describe J0202-0107, J0202-5055 respectively in reference to the IMF.

5.4.2.1 J0202-0107

J0202-0107 transitions from intrinsically singly to multiply imaged for M/L between 1.25–1.75, see Figure 5.7 (blue and green tracks). As this source is bright, the probability of a non-detection (thick grey) follows very closely the intrinsically single-imaged (blue) track. After converting from M/L to α it is clear for any IMF heavier than Salpeter the emitter must be intrinsically multiply imaged (Figure 5.8).

If we compare our 50 per cent probability cut off to that reported in Smith, Lucey & Collier (2018), this result is 20 per cent larger. The revised solar absolute magnitude contributes to a 12 per cent increase. The remaining difference must originate from other modelling

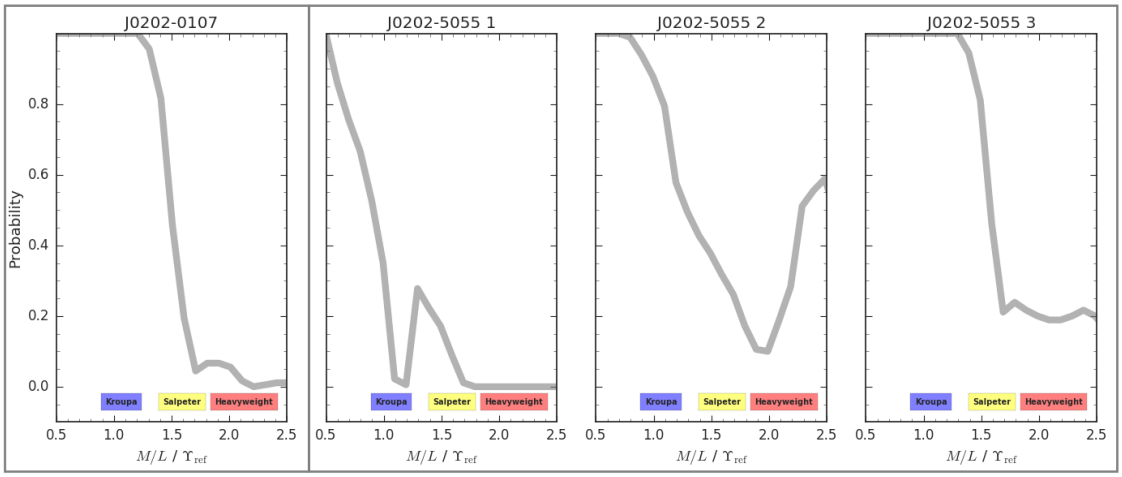

Figure 5.8: The constraints for the upper-limit lensing analysis converted from K-band M/L to α. The grey lines show the probability of the source having no *detectable* counter-image. Marked along the horizontal axis are approximate bounds for different choices of IMF. The panels are labelled for the galaxy they relate to, *left:* J0202-0107, *middle left/ middle right/ right:* J0202-5055 $z = 0.295$, 1.289 and 0.907 sources.

uncertainty. In the earlier paper we fitted a de Vaucouleurs profile ($n = 4$) to a Pan-STARRS y-band image and scaled the resulting model to a 5 arcsec aperture 2MASS K_s flux. We now instead fit directly to VISTA K_s-band imaging, and allow a free Sérsic parameter. This leads to a difference of 0.05 mags between the apparent magnitude here using the de-convolved GALFIT model, compared to the psf-corrected measurement from 2MASS (due to the much larger 2MASS PSF). Finally, our cosmology leads to a 3 per cent change, with an increased H_0 value. Therefore, the changes in how the lens light is modelled, and the cosmology account for the difference relative to the earlier work.

5.4.2.2 J0202-5055

The M/L constraints for the nearest three emitters in the J0202-5055 system are displayed in Figure 5.7. We do not consider the effect of multiple-plane lensing for any of the sources. The source with the smallest separation is also at the lowest redshift, so there is no multi-plane effect in this case. In principal there is an impact on the other two sources from those preceding in redshift, but the effects are likely negligible because the lensed galaxies are likely to be very low-mass.

The inner source is separated from the galaxy centre by 1.92 arcsec with $z = 0.29$, and the outer source is separated by 3.4 arcsec, at $z = 1.29$. The inner source is expected to be *intrinsically* multiply imaged even for stellar populations described by $M/L = 1$. As the source is faint, and the probability for a non-detection is low in the quad regime. There is a small tail at $M/L = 1.2$–1.5. Hence the depth of our observation is the limiting factor for a non-detection of a counter-image for this source. The second source is more distant, and hence can be intrinsically single-imaged for more massive systems up to $M/L \simeq 1.1$–1.3.

As with J0202-0107, we convert from M/L to α in order to investigate this system with respect to the IMF (See Figure 5.8). If the foreground galaxy formed with an IMF consistent with Kroupa, the first source should be multiply imaged, but the second and third sources are likely not. If we consider a Salpeter IMF, or an α consistent with that predicted from Atlas3D (~ 1.5, Cappellari et al., 2013) the first and second source are intrinsically multiply imaged. A galaxy forming with a "heavyweight" IMF may even produce counter-images for all three sources.

J0202-5055 offers a promising system for further observations, as for any reasonable IMF parametrisation a deeper observation is likely to unveil a counter-image to the innermost source. Analysis can then constrain α, using the same technique as the other low-z systems (i.e. J0403-0239 in Collier et al., 2018b, and Chapter 6). In addition, the second faint source, separated by 3.4 arcsec, offers a potential double source-plane if the lens IMF is even modestly heavier than Kroupa (including DM).

5.4.2.3 Summary

Out of the nine apparently single-imaged systems presented in Figure 5.5, analysis showed two systems which likely have faint counter images for even a low M/L lens (J0202-0107, J0202-5055, see Figure 5.7). However, more detailed analysis shows that J0202-0107 cannot rule out having formed with a moderately heavy IMF (α; 1.25–1.75). This range is consistent with the α-vs-σ relation measured with stellar dynamics by Cappellari et al. (2013), which predicts $\alpha = 1.5 \pm 0.3$ for $\sigma = 264\,\mathrm{kms}^{-1}$. For J0202-5055, if the lens forms

with an IMF consistent with the α-vs-σ relation, then a double source plane lens will be discovered with deeper observations. If confirmed by future observations, J0202-5055 will be the first known low-z double source-plane system.

5.5 The MNELLS search efficiency

In this Section we will assess the MNELLS programme technique. In Section 5.5.1 we test the flux detection threshold as a function of wavelength, and then of distance from the centre of the target galaxy. In Section 5.5.2, we determine the number density of background emitters in our dataset. Then in Section 5.5.3 we discuss potential modifications to the observing strategy, and contrast our technique to the MaNGA survey.

5.5.1 Detection threshold with artificial point sources

The flux detection limit for a background source is the key parameter for assessing the efficiency of the MNELLS observing setup. This will test whether the true observed depth matches our expectation based on other surveys and inform plans for future observing campaigns.

We compute the recovery fractions by injecting fake point sources, convolved to a representative PSF, into a real datacube. There is scatter in the sky background from galaxy to galaxy, so we select J2318-1023 which contains few other bright emitters and has noise properties representative of the median of our sample. Each source is modelled with a gaussian with a FWHM of 5 Å and a spatial FWHM matched to the datacube seeing of 0.8 arcsec, typical for an emission line within our survey. Sixteen sources are injected into the datacube as a 4×4 source grid, with a subpixel scatter applied to each position in both the spatial and spectral dimensions. For each wavelength and flux we had nine realisations to total 154 sources. The sources are then scaled to total fluxes ranging from $10^{-15.25}$ to $10^{-18.5}$ erg s^{-1} cm^{-2}, in steps of 0.25 dex.

We perform this test for four wavelength channels which are representative of the typical noise situations for the background emitters. The channels are chosen as 5000 Å, 6861.25 Å, 7100 Å, 7242.5 Å, which covers the blue, less sensitive region of the datacube (5000 Å), a mid-way low sky noise region (7100 Å), and then two regions of the datacube close to sky lines. These are selected to match the wavelengths used in equivalent analysis by Herenz et al. (2017). For each cube with simulated sources the full processing and emission line detection is carried out, as described in Section 4.4, and the recovery fractions are measured.

The most sensitive of these channels is the 7100 Å channel, with a 90 per cent threshold of $\sim 10^{-16.15}$ erg s^{-1} cm^{-2}. In contrast, the bluest channel (5000 Å) has a significantly lower sensitivity, ~0.4 dex offset from 7100 Å see Figure 5.9. This is likely due to a high lunar continuum, i.e. a high fraction of lunar illumination (FLI), which ranges up to 0.9, during the time of our observations. Note that in practice, the impact of a low detection threshold in blue channels could be reduced as the emission lines detected in the blue are mainly low-z [O II] emitters. These may still be identified from strong [O III] and H α lines, which will be present in lower background redder channels. The only lines with no strong counterparts in the cleaner spectrum are Ly-α emitters.

For comparison to these results, we have performed the same fake source injection into a MUSE-Wide datacube. We reach a threshold ~ 0.5 dex fainter (at 7100 Å) with these data. The difference originates from the sky background due to their observations taking place in dark time. After the ETG is filtered, the MNELLS background is on average three times higher, with the most significant difference seen at 5000 Å (due to the high FLI), and the weakest at 7242.5 Å where the noise is instead dominated by a bright sky line.

Our search is designed to target sources which are close to the centre of a foreground galaxy. Hence we incur a much larger contribution to the noise than just the sky background at small lens-source angular separation. Figure 5.10 shows the detection limit for the 7100 Å channel as a function of radius. Within 6 arcsec of the galaxy centre ($\sim 2\,R_{\rm Ein}$), the flux threshold is typically 0.35 dex brighter than the full FoV. Beyond a radius of 10 arcsec the sensitivity shows no strong radial dependence.

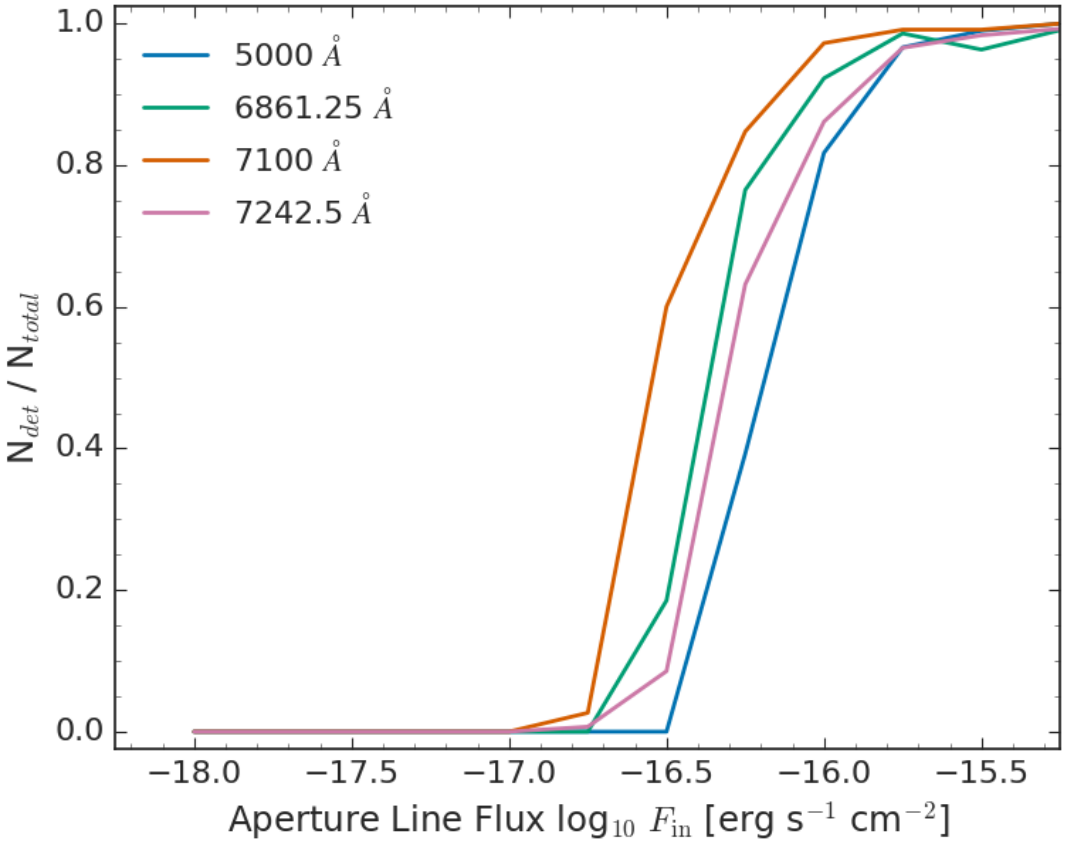

Figure 5.9: Recovery fraction detected/injected, from the insertion and detection of fake point sources for four different wavelengths within a single MUSE datacube. The detection process follows that used for the targeted observations.

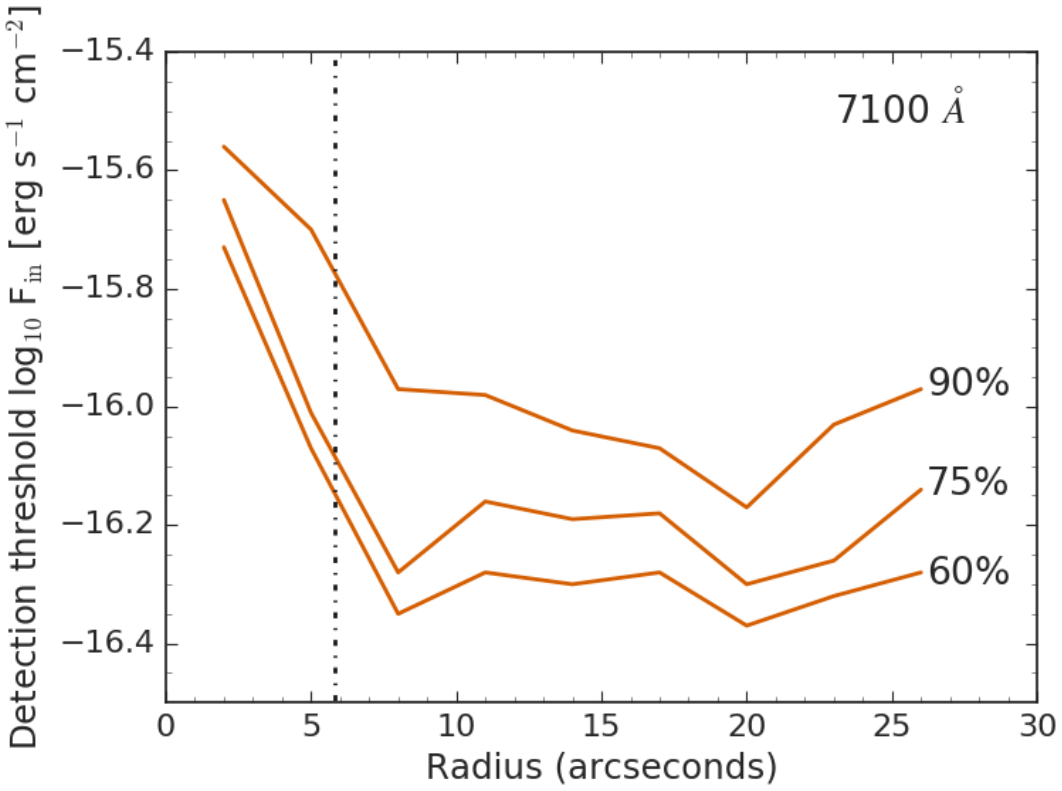

Figure 5.10: The detection threshold radially binned for fake sources injected into a real datacube. This is for only the 'best' wavelength channel from Figure 5.9 is taken (7100Å). We show the detection limit within each bin for changing recovery fraction. There is a large drop in the threshold for the centremost radii due to the subtraction of the foreground candidate 'lens'. The typical predicted $2R_{\rm Ein}$ is marked with a dashed line.

5.5.2 Number density of background emitters

In this subsection we consider the number density of background emitters actually detected within our targeted observations. We also compare to the MUSE-Wide for our measured flux threshold. The MNELLS observations are shallow exposures taken in poor seeing conditions, see Section 4.3.1. In our calculations we only include the fourteen fields which have the full exposure time; in total these fields have 164 detected emitters. The average full depth area within a combined datacube is 0.92 square arcmin, therefore the median number density of emitters within our full depth observations is 12.7 per square arcmin; the field-to-field standard deviation is 5.5.

The full depth MUSE-wide survey reaches a number density of 37.4 emitters per square arcmin. In comparison with MNELLS, each observation is 20 per cent longer (a 1 hr exposure), in conditions with a lower sky background (observed in dark/grey time instead of grey/bright). So, using their figure 13, and with our cut off at a depth of $10^{-16.1}$ erg s^{-1} cm^{-2} (for 90 per cent to be detected), we would predict 6.3 emitters per square arcmin. The number density from our MUSE data (12.7 per square arcmin) is actually twice this. The detection threshold which aligns these two values is a flux limit of $10^{-16.5}$ erg s^{-1} cm^{-2}. From Figure 5.9, this suggests we should adopt a 60 per cent detection limit to align our numbers with the MUSE-Wide.

For the central 6 arcsec where the detection threshold for 60 per cent recovery (to match the achieved number density of emitters) is $10^{-16.15}$ erg s^{-1} cm^{-2}, the MUSE-wide predicted number count is 6.3 per square arcmin (an 80 per cent decrease). For the average targeted galaxy, the strong lensing regime encompasses 23 square arcsec ($\pi {R_{\rm Ein}}^2$; $R_{\rm Ein} = 2.7$ arcsec). The resulting probability for a lens galaxy having a detectable multiply imaged source is 0.04. So we expect one in 25 observed galaxies will exhibit a multiply imaged background source. Note that the counter-images may be fainter than the detection threshold.

5.5.3 Considerations for future MNELLS-like surveys

The MNELLS project observational constraints (e.g. no moon constraints) were selected to maximise the number of executed observations by taking advantage of under-used observatory conditions, under the assumption that the ETG will dominate the background. We predict the number of lenses to be one in every twenty-five full depth observations, and in calculating this we uncovered a few key contributions affecting our detection limits which need to be considered for future targeted surveys.

The background noise from the lunar continuum and sky brightness has clearly affected our detection limits. The variable observing conditions (specifically the FLI and sky background) may provide a simple explanation for the origin of the large field-to-field scatter in the number of detected emitters, independent of the lens light. In addition the presence of the ETG light also negatively impacts the detection threshold. Hence, these two effects (higher background, and lens subtraction) reduce our detection threshold compared to the MUSE-Wide survey by almost 0.5 dex. The centre of the datacube is less sensitive to faint emitters, which cannot be avoided, but at shorter wavelengths we are also offset by 0.4 dex from channels less affected by the lunar continuum. For future surveys, as a trade off for the number of observations, a tighter constraint on the moon illumination may be considered to reduce the sky background.

In addition to altering the observing conditions, we can consider an alternative selection method, which may improve the likelihood of a lens discovery. Our current selection criteria (Section 4.3.1) uses a single-fibre velocity dispersion as a proxy for stellar mass, and hence $R_{\rm Ein}$. Instead we could directly measure $R_{\rm Ein}$ from a mass-follows-light profile, (such as those used in our upper-limit lensing calculations), and select galaxies to maximise the lensing cross-section. However, using the light profile measured $R_{\rm Ein}$ as a part of the selection process introduces additional computation, which will require additional cuts in parameter space to be efficient. Instead the current technique is considerably simpler, and the $R_{\rm Ein}$ scales with the velocity dispersion (Bolton et al., 2008).

An alternative to the 'targeted' blind search methods like MNELLS is to exploit large IFU

surveys. For example the Mapping Nearby Galaxies at APO (MaNGA) survey (Bundy et al., 2015) has a sample median redshift of $\langle z \rangle = 0.05$ ($100 < \sigma < 400$ kms^{-1}), which is comparable to MNELLS. The full MaNGA survey will take IFU observations of over 10 000 galaxies and hence will discover a number of low-z strong gravitational lenses. To date, Talbot et al. (2018) worked with a sample of 2812 ETGs, and so far has produced 2–6 candidate lenses.

Although MaNGA's median redshift is comparable to that of MNELLS, it aims to observe a broad range of galaxy sizes, including a high fraction of low-σ ETGs. The larger (higher-σ) ETGs typically lie more distant than their median redshift, so that the same fraction of $R_{\rm Eff}$ is imaged within the FoV (See Fig.8, Bundy et al., 2015). This has two implications. First, the low-z, low-σ galaxies are less likely to be gravitational strong lenses so the number of discovered lenses is likely reduced. Secondly, the higher σ galaxies which are more likely to be lenses lie at higher redshift and are hence subject to larger DM uncertainties. Such lenses, (e.g. J1701+3722, Smith, 2017; Smith et al., 2020, $z = 0.12$), are complimentary to SNELLS/MNELLS nearby lenses, but not identical. However, lenses within this redshift range may offer an avenue to address the differences between the SLACS and SNELLS/MNELLS conflicting samples.

5.6 Summary

This chapter presented the lensing analysis of two out of the three newly-discovered cluster-scale strong lenses, and nine singly imaged but closely projected source systems. The cluster-scale lenses are dominated by dark matter, even for a Salpeter-like IMF, and hence no constraints on the IMF are inferred. Of the nine 'upper limit' systems, two are likely to be intrinsically multiply imaged for a Salpeter or lighter IMF. In particular, J0202-5055 has a source projected at 1.92 arcsec which has a high probability of being multiply imaged for even a MW-like IMF. For this system, deeper data may uncover the lowest-redshift lensing system yet found.

The flux limit within the MNELLS datacubes is $10^{-16.5}$ erg s^{-1} cm^{-2} but the central

sensitivity is 0.35 dex lower due to the foreground galaxy continuum. The detection threshold in the blue region of the spectrum suggests the lunar background significantly affects the observations. This effect is likely to only affect Ly α emitters, as [O II] will have longer wavelength strong emission lines present in regions of lower background. However, future optical observations may prefer a more restrictive lunar continuum to detect higher redshift, fainter, Ly-α emission.

Comparing the detection threshold with the MUSE-wide number counts, a multiply imaged strong lens is predicted to occur at a rate of one in every twenty-five observations. In 14 targets there are two closely projected but singly imaged sources and no strong lenses (our reported strong-lensing galaxies are from the archival sample), which is consistent with Poisson statistics of these predictions.

In addition to the cluster-scale lenses and the singly imaged but closely projected source systems, there is one remaining 'success' from Chapter 4. The galaxy-scale multiply imaged system is comparable to the SNELLS lenses presented in Chapter 3. In the next chapter, I present the lensing analysis of the confirmed multiply imaged lens J0403-0239.

CHAPTER 6

A fourth low-z strong lensing ETG

6.1 Preamble

The three cluster-scale lenses and nine 'upper limit' systems described in the previous chapter do not strongly constrain the IMF of each individual system. In contrast, the IMF within a multiply imaged galaxy-scale system can be inferred directly. In this chapter, I report the discovery and subsequent analysis of J0403-0239. This lens galaxy is a giant elliptical at $z = 0.06604$ with a velocity dispersion of $\sigma = 314\,\mathrm{km\,s^{-1}}$. The lensed source has a redshift of 0.19165 and forms a pair of bright images on either side of the lens centre. The Einstein radius is 1.5 arcsec, projecting to 1.8 kpc, which is just one-quarter of the galaxy effective radius.

The chapter closely follows the work published in Collier et al. (2018b). However, since publication, new *HST* and ESO/VLT FORS2 data were acquired for J0403-0239. Using these data, the concerns raised about our analysis by Galbany et al. (2018) are addressed. Using a spectrum extracted from the MUSE data they measured a 2.75 Gyr light-weighted population, suggesting that an old stellar population should not be assumed.

6.2 Introduction

The IMF is fundamental to understanding galaxy formation and evolution, as well as to interpreting observed properties (e.g. estimating stellar masses). Within the different star forming environments in the Milky Way, the stellar initial mass function (IMF) is well constrained, and approximately invariant (Bastian et al., 2010; Offner et al., 2014). Deviations toward a flatter IMF have been reported for some resolved ultra-faint Local Group dwarfs (Geha et al., 2013).

For galaxies beyond the Local Group, resolved studies are not possible, and the IMF must be inferred from the integrated light and/or gravitational mass tracers. Broadly, the observational techniques fall into two categories. The first method infers the stellar population via high signal-to-noise spectroscopy. The strength of gravity sensitive absorption lines are measured by fitting detailed stellar population synthesis templates. The second method indirectly measures the stellar population by comparing a stellar mass-to-light ratio (M/L) measured from stellar dynamics or strong lensing to a reference M/L from a fixed IMF stellar population model. Studies independently using both techniques have found evidence for an increasingly 'heavy' IMF (more measured mass than a fixed IMF model predicts) in the most massive ETGs (e.g. Treu et al., 2010; Cappellari et al., 2012; Conroy & van Dokkum, 2012b; La Barbera et al., 2013).

The mass measurements from gravitational lensing require careful treatment to disentangle the contributions of stellar mass and dark matter (DM). For example, Treu et al. (2010) analysed lenses at $z \sim 0.2$ by combining lensing and stellar kinematics to constrain the parameters of a two-component mass model. This approach involves several assumptions (spherical geometry, constant stellar mass-to-light ratio, etc). In contrast, *nearby* ($z \leq 0.1$) lenses offer a geometry in which the Einstein radius ($R_{\rm Ein}$) is reached at smaller physical radii and hence probes the dense stellar-dominated core. In such cases, the relative uncertainty from DM is minimized, as the ratio of dark to stellar matter is reduced and "pure" lensing constraints on the stellar mass can be obtained (i.e. with no additional information from stellar kinematics).

At present, the best studied $z < 0.1$ lensing ellipticals are those discovered by SNELLS (Smith, Lucey & Conroy, 2015). This targeted approach used an integral field unit (IFU) to search for background emitters behind massive elliptical galaxies, finding SNL-1 ($z = 0.031$) and SNL-2 ($z = 0.052$), and 'rediscovering' the previously-known lens SNL-0 ($z = 0.034$) (Smith et al., 2005; Smith & Lucey, 2013). The SNELLS galaxies yielded lensing masses in strong disagreement with 'heavy' IMFs for massive ETGs, instead measuring M/L consistent with a MW-like IMF (Kroupa, 2001), both in low resolution ground based (Smith et al., 2015) and high resolution space-based observations (Collier, Smith & Lucey, 2018a).

With only three galaxies, the possibility that the SNELLS sample *by chance* was drawn from the 'tail' of an intrinsically broad distribution in IMFs cannot be ruled out. As such, with small number statistics, increasing the sample size is essential to investigate further this conclusion, and to test whether these lenses are representative of the parent population.

Discovering low-redshift lenses is challenging due to the high surface brightness of the massive foreground galaxy. While SNELLS pre-selected high-probability lenses using velocity dispersion measurements, an alternative approach exploiting large multi-IFU surveys like SAMI and MaNGA (Bryant et al., 2015; Bundy et al., 2015) has recently yielded new systems (Smith, 2017; Talbot et al., 2018). A third technique, which we are pursuing currently, is to search for lensed line emitters behind galaxies targeted for other science goals, using data from public archives. Observations made with MUSE (Bacon et al., 2014) on the ESO VLT are well suited to this method, due to the very high sensitivity and wide spectral range (4750–9300 Å) of the instrument.

This chapter presents the discovery of the first multiply imaged strong gravitational lens from this programme. In Section 6.3, we briefly describe the modified lens search process. In Section 6.4, we present the new lens system properties. In Section 6.5 we present lensing mass constraints and the IMF mass excess parameter. In Section 6.6, we revise the lens mass estimates with *HST* data, and refit the age of the stellar population to an ESO/VLT FORS2 spectrum. The results are compared and combined with the SNELLS sample in Section 6.7.

6.3 A MUSE archival lens search

Our new lensing system was identified in the course of a systematic search for multiply imaged line emitters behind low-redshift ETGs in public archival MUSE data. The full description of this programme is presented in Chapter 4; here, we briefly summarise the sample selection and main processing steps to provide context for the new discovery.

For this lens search, we are analysing public MUSE observations which overlap with luminous nearby galaxies selected from the 2MASS Redshift Survey (Huchra et al., 2012). We focus our search on targets with redshift $5\,000 < cz < 20\,000\,\mathrm{km\,s^{-1}}$, and $M_K < -25.7$.

The analysis begins with "Phase 3" pipeline-reduced products retrieved from the ESO Science Archive. Our primary goal is to detect faint lensed background emitters behind the central regions of nearby ETGs. Before attempting line detection, we therefore process the pipeline-reduced data-cubes to subtract the bright stellar foreground, effectively fitting elliptical isophote models to each wavelength channel. The residual cubes are noise-normalised and filtered to suppress instrumental artifacts.

Candidate emission lines are then identified above a significance threshold in the processed residual cubes. Spectra for likely sources are extracted, and redshifts are estimated automatically using MARZ (Hinton et al., 2016). Finally, the resulting object catalogue is visually inspected, and searched for any spatially-separated line-emitters with similar redshifts, which are potentially multiply imaged background galaxies.

Although we optimise our search method to detect faint background emission, the first galaxy-scale lens discovered was over 100 times brighter than our detection limit. Hence we report this system as a "special case" in this paper.

6.4 The new lens

2MASXJ04035024–0239275 (hereafter J0403-0239) is a luminous ($M_K = -25.7$) elliptical galaxy at heliocentric redshift $z_\mathrm{H} = 0.06655$ (Jones et al., 2009). In imaging from the Pan-

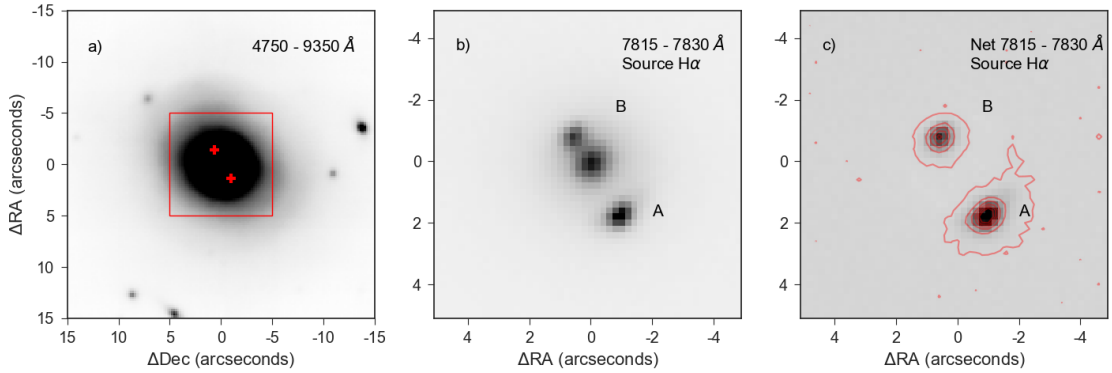

Figure 6.1: MUSE data of J0403-0239, within different wavelength ranges (shown in the top right). a) displays a broadband image collapsed over the entire MUSE wavelength range, displaying the lens structure. The red crosses mark the arc positions, while the red box encompasses the region shown in panels b) and c). In b) we collapse about the H α line in the background source, revealing arcs A and B, separated by 2.94 ± 0.06 arcsec, without the need for lens subtraction. c) shows the continuum-subtracted image at the same wavelength, with contours to show the outer isophotes of the arcs.

STARRS PS1 survey (Chambers et al., 2016) J0403 shows a smooth inner light profile, well fitted by a Sersic profile with index $n \approx 4$. In the outer regions (radius > 20 arcsec), some low-surface-brightness (i–band $\sim$25 mag arcsec^{-2}) tidal structures are visible. J0403-0239 is a relatively isolated galaxy, with no overdensity of similar-colour objects visible in PS1 imaging. The closest comparable brightness companion (2MASXJ04034531–0236595) is a spiral galaxy, fainter by 1.3 magnitudes, with relative velocity +550 km s^{-1}, at a projected distance of ~ 210 kpc (2.7 arcmin). There are no catalogued clusters with comparable redshift within a radius of 2 degrees (9.5 Mpc).

J0403-0239 was observed with MUSE as part of a study targeting supernova hosts (ESO programme 098.D-0115(A); PI L. Galbany). The exposure time was $\sim$ 2400s, with seeing $\lesssim 0.8$ arcsec (estimated FWHM from compact sources). The MUSE field-of-view is 1×1 arcmin^2 ($\sim 80 \times 80$ kpc^2).

In the MUSE data (Figure 6.1a), the light profile of J0403-0239 is smooth at small radii, with evidence for the faint tidal features seen in the PS1 imaging. Extracting narrow band images (Figure 6.1b) highlights a pair of extended background emitters (arcs A and B) either side of the galaxy centre. Strong H α, [O III], and H β lines are present in the

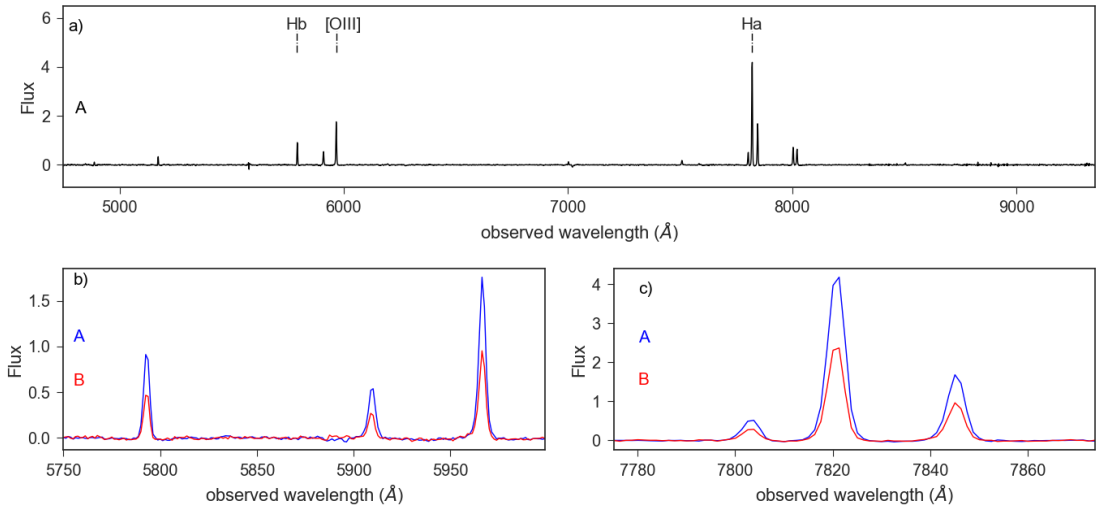

Figure 6.2: MUSE spectra of the lensed images, with flux in units of 10^{-16} ergs^{-1}cm^{-2}Å^{-1}. In a) we display the arc spectrum extracted from a continuum-subtracted residual datacube, showing the bright Hα, [N II], [O III], Hβ, Hγ and [S II] emission lines, at a redshift of 0.19165. In b) and c), we overlay the emission from images A and B, for the [OIII] and Hα regions, respectively. There is negligible velocity offset ($\lesssim 50$ km s^{-1}) between the two spectra, and image A has been subject to a greater magnification.

spectra of both emitters, with the same redshift, $z_{\rm H} = 0.19165$ (Figure 6.2). The respective velocity offset between A and B is ≤ 50 km s^{-1}, providing strong evidence of a common source. When the continuum is subtracted, image A shows slight curvature at low surface brightness levels (Figure 6.1c). There is some evidence of a small velocity gradient (~ 50 km s^{-1} peak-to-peak) across arc A, which is mirrored in arc B. A broad–band counterpart to arc A is readily visible in the PS1 imaging, and the counter–arc is recovered after subtraction of a smooth light profile for J0403-0239. The balance of evidence in this case strongly favours a lensing interpretation.‡

The lensed images are separated by 2.94 ± 0.06 arcsec (~ 3.75 kpc), where the uncertainty is derived from measurements at various emission lines. For our lensing analysis we adopt $R_{\rm Ein}$ as half of the image separation, 1.47 ± 0.03 arcsec, and extract an aperture spectrum ($\leq R_{\rm Ein}$) of J0403-0239, shown in Figure 6.3. The spectrum displays the strong absorption features typical of an old stellar population, with strong Na D, Mg I and TiO,

‡After the submission of our paper, Galbany et al. (2018), independently reported the discovery of this lens.

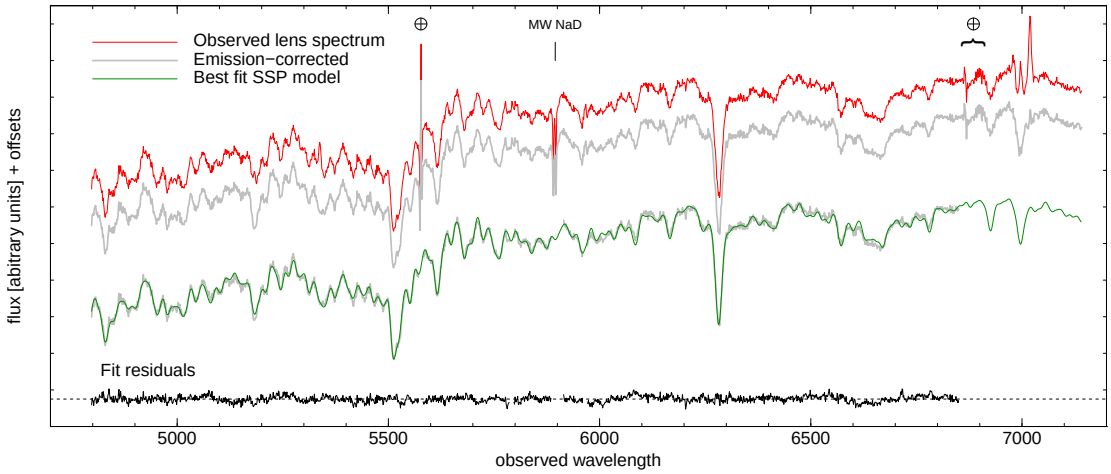

Figure 6.3: The MUSE spectrum of the lens galaxy J0403-0239, extracted within the Einstein aperture, i.e. radius 1.5 arcsec, after masking pixels strongly affected by the arcs. For clarity, only the region of the MUSE spectral range (4750–6850 Å) used for fitting the stellar population models is shown. The observed spectrum (red) shows that the galaxy has an absorption-dominated spectrum, but also has a nebular line emission component, seen most easily in the Hα–[N II] region. The corrected spectrum, shown in grey, after subtracting an emission-line model, fitted to the Hα–[N II] complex, and assuming Case B recombination and galactic (no internal) extinction, to predict the Hβ emission. Below, we reproduce the emission-corrected spectrum, and show the best-fitting stellar population (green), derived from the models of Conroy & van Dokkum (2012a). This model has age 12 Gyr and metal abundances typical for massive ellipticals. The fit residuals, shown in black, have a 1 per cent rms. In fitting this model, we exclude the Hα region, as well as wavelengths contaminated by atmospheric artifacts (indicated by $\oplus$) and the MW neutral sodium doublet.

along with weak H α and H β emission. The measured heliocentric redshift, $z_{\rm H} = 0.06604$, and velocity dispersion of $\sigma = 314 \pm 5$ km s^{-1}, are found by fitting this central region using PPXF (Cappellari & Emsellem, 2004).

Using i-band imaging from the Pan–STARRS (PS1) survey we measure a total magnitude for J0403 of 14.26 ± 0.04 mag and an effective (half-light) radius of 5.7 arcsec (i.e. 3.9 times the size of $R_{\rm Ein}$). Within $R_{\rm Ein}$ we measure an aperture magnitude of 16.35 ± 0.01 mag. As the PS1 point spread function (PSF)(~ 1.1 arcsec) is comparable in size to $R_{\rm Ein}$, a PSF correction is necessary. We determine the correction by fitting a Sersic model via GALFIT (Peng et al., 2010), with a convolution kernel derived from a set of adjacent stars. The magnitude difference between the Sersic model before and after convolution was 0.22 ± 0.02 mag and hence we adopt a PSF-corrected Einstein-aperture magnitude of $i_{\rm Ein} = 16.13 \pm 0.02$ mag.

6.5 Lensing mass and the IMF

Gravitational lensing provides a precise measurement of the total projected mass within the Einstein radius ($M_{\rm Ein}$). Measuring $M_{\rm Ein}$ and the luminosity within the same aperture, $L_{\rm Ein}$, the resulting mass to light ratio can be related to the IMF mass excess parameter, α. This factor is defined as:

$$\alpha = \frac{\Upsilon}{\Upsilon_{\rm Ref}} = \frac{M^{*}_{\rm Ein}}{L_{\rm Ein}} \times \frac{1}{\Upsilon_{\rm Ref}} = \frac{M_{\rm Ein} - M^{\rm DM}_{\rm Ein}}{\Upsilon_{\rm Ref} L_{\rm Ein}} \ ,$$

where $M^{\rm DM}_{\rm Ein}$ is the dark matter component. We compare Υ, the observed stellar mass-to-light ratio, to $\Upsilon_{\rm Ref}$, a reference mass-to-light ratio for a modelled stellar population with comparable properties (i.e. metallicity, age), with a fixed Kroupa (2001) IMF. Hence a Kroupa IMF has $\alpha = 1$ by definition, while a Salpeter IMF (Salpeter, 1955), with more low mass stars, has $\alpha = 1.55$.

We compute $M_{\rm Ein}$ using the symmetric lens equation (see Smith et al., 2015, section 4.1). We adopt cosmological parameters from the 7-year *Wilkinson Microwave Anisotropy Probe* (WMAP), i.e. $\rm H_0 = 70.4$ km s^{-1} Mpc^{-1}, $\Omega_{\rm m} = 0.272$ and $\Omega_{\Lambda} = 0.728$ (Komatsu et al., 2011),

to calculate the lensing geometry for redshifts in the CMB frame ($z_{\rm CMB} = 0.06569, 0.19130$ and $\frac{D_{\rm l} D_{\rm s}}{D_{\rm ls}} = 400.5$ Mpc). We derive a total projected mass, $M_{\rm Ein} = 10.64 \pm 0.23 \times 10^{10}$ M$_\odot$, with the 2 per cent uncertainty dominated by the measurement of $R_{\rm Ein}$. Including a small ellipticity ($e \approx 0.1$ as measured from GALFIT) increases the mass by 3 per cent, and the inclusion of a small external shear (< 5/1 per cent for SIS/SIE) reproduces the image positions perfectly. In order to account for these additional possible complexities, we revise the uncertainty in $M_{\rm Ein}$ to ~4 per cent, i.e. 0.4×10^{10} M$_\odot$.

The DM mass component is estimated following Smith et al. (2015), using the EAGLE hydrodynamical cosmological simulation (Schaye et al., 2015). We measure the average DM mass which would be projected inside an aperture of 1.8 kpc, averaged over all EAGLE halos hosting galaxies with stellar velocity dispersions >275 km s^{-1}. This indicates a contribution of $\mathrm{M}_{\rm Ein}^{\rm DM} = 2.01 \pm 0.36 \times 10^{10}$ M$_\odot$ (i.e. 19 per cent of M$_{\rm Ein}$), which yields an aperture stellar mass $M_{\rm Ein}^{*}$ of $8.63 \pm 0.54 \times 10^{10}$ M$_\odot$.

Other mass contributions within the Einstein aperture are expected to be small. For typical ETGs from the ATLAS^{3D} sample the gas contribution measured within $2R_{\rm eff}$ is $\sim 10^9$ M$_\odot$ for the cold gas (Young et al., 2011, 2018), and $\sim 10^9$ M$_\odot$ for the hot gas (Su et al., 2015). As the Einstein aperture is significantly smaller than this, the gas contribution is expected to be less than 1 per cent of the measured lensing mass. The average contribution from a black hole hosted by a comparable ($\sigma \approx 300$ kms^{-1}) galaxy is $\sim 2 \times 10^9$ M$_\odot$ (van den Bosch, 2016), i.e. ~2 per cent of the lensing mass. We do not apply a correction for these effects.

The lens aperture luminosity is calculated from the PSF corrected $i_{\rm Ein}$, with additional corrections for the line-of-sight galactic extinction and the k–correction.

Despite being located at fairly high galactic latitude ($b = -38°$), J0403-0239 lies in a region of relatively high galactic extinction, with $A_i = 0.26$ according to the Schlafly & Finkbeiner (2011). Alternatively, maps based on PS1 stellar photometry (Schlafly et al., 2014; Green et al., 2018) indicate slightly smaller values, with $A_i = 0.22$. The MUSE spectrum shows a clear galactic Na D absorption doublet (~1 Å equivalent width), which supports the presence of substantial interstellar material along this sightline. We adopt a correction of

0.24 mag, and allocate an error of 0.04 mag (16 per cent of the extinction in magnitudes, following Schlegel et al. (1998). The k–correction is estimated from the lens g–i colour index (1.7) to be $k_i = 0.04 \pm 0.01$ mag (Chilingarian et al., 2010; Chilingarian & Zolotukhin, 2012) .

The final corrected Einstein-aperture apparent magnitude is $i_{\rm Ein} = 15.87 \pm 0.05$, which for the adopted cosmology ($D_{\rm L} = 295.7$ Mpc), and the solar AB i–band absolute magnitude of 4.534 (Blanton & Roweis, 2007), yields an aperture luminosity of $2.59 \pm 0.12 \times 10^{10}\,{\rm L}_{\odot}$. The uncertainty is dominated by the applied corrections. Combined with $M^{*}_{\rm Ein}$ the observed stellar mass-to-light ratio is $\Upsilon = 3.33 \pm 0.26$ solar units.

To convert from mass-to-light ratio (Υ) to the IMF mass factor α, we need an estimate for the reference mass-to-light ratio for a given fiducial IMF (here Kroupa, 2001), which depends on the stellar population properties: age (or star-formation history), metallicity, etc. To estimate these parameters, we make use of the MUSE spectrum of the lens galaxy extracted within the Einstein aperture, shown in Figure 6.3 (red line). However, the presence of significant nebular emission, combined with limited spectral coverage in the blue, presents some challenges. Specifically, the stellar population age is constrained only by the Hα and Hβ absorption lines, but both are contaminated by gas emission, to different extent.

We tackle the nebular emission by first fitting a three-gaussian model to the Hα and [N II] lines, with an assumed stellar continuum model. The relative amplitudes of the [N II] lines are fixed, and all lines are assumed to have the same velocity and width. The amplitudes of Hα and the [N II] doublet are allowed to vary. From this model, we can predict the Hβ emission line, assuming Case B recombination for the intrinsic line ratio, and a relative attenuation factor of 1.135 for Hβ from the MW extinction (we assume no internal extinction for this exercise). Because the underlying Hα absorption has only low sensitivity to the stellar population age, the emission correction is quite robust against changes to the age assumed in the first step.

After making this correction to remove the emission-infilling of the spectrum at Hβ, we perform a full-spectrum fit over the interval 4500–6400 Å, using single-burst models from

Conroy & van Dokkum (2012b), (Figure 6.3, green). We allow for variation in abundances of Mg, Fe, Na, and C, as well as variation in age. Formally, the fit implies an old population, with age 12.0 ± 1.0 Gyr, high metallicity [Z/H] $\approx$ [Mg/H] $\approx +0.15 \pm 0.02$ and typical massive elliptical galaxy abundance ratios [Mg/Fe] $\approx +0.3$, [Na/Fe] $\approx +0.5$, [C/Fe] $\approx +0.2$.

The reference mass-to-light ratio is estimated with Conroy et al. (2009) stellar population models accessed via EZGAL (Mancone & Gonzalez, 2012). For a Kroupa (2001) IMF, with an old, solar metallicity stellar population ($z_{\rm form} = 3$), the models predict $\Upsilon^*_{\rm Ref} = 2.90 \pm 0.10$. The uncertainty is derived from small variations in the metallicity and age (e.g. $z_{\rm form} = 2.5$–3.5, metallicity 1–1.5 solar). The resulting IMF mass excess parameter, with its statistical error, is $\alpha = 1.15 \pm 0.10$.

Several adopted parameters and assumptions affect the value of α derived above. If we had prescribed the Planck Collaboration et al. (2016) cosmology, α would be 4 per cent lower, due to the variation in H_0. If we had attributed the total lensing mass entirely to the stellar component (i.e. no DM inside $R_{\rm Ein}$), we would have found $\alpha = 1.42$, a 25 per cent increase. If we had assumed, due to the limited blue (most age sensitive) coverage from MUSE, that the population may be 8.5 Gyrs old ($z_{\rm form} = 1.5$), α would have increased by 14 per cent. If we had adopted the Maraston (2005) models, α would increase by 10 per cent.

6.6 J0403-0239 re-analysed

The strong-lens J0403-0239, with the assumption of an old stellar population, has a measured M/L consistent with a Milky-Way like IMF. However, in Galbany et al. (2018), they suggest "*we note that to discriminate between different IMFs is unfeasible*", and point towards the MUSE coverage as lacking key features below $\lambda > 4750$ Å such as CaII and the high order Balmer lines. Furthermore, should the age of J0403-0239 be consistent with their STARLIGHT fit, which includes a 'frosted' younger population, then $\Upsilon_{\rm ref}$ will decrease, and α may be consistent with Salpeter or 'heavier' IMFs. Potential supporting factors for this case are the hints of a perturbation to J0403-0239 in the MUSE data. To the East there is a region of [NII] emission at the lens redshift, and there are extended shells

in deep optical data (DESI legacy survey Dey et al., 2019). Therefore additional analysis with improved data and a coverage of wavelengths shorter than from MUSE is required to address these proposed issues.

6.6.1 Improved lens modelling

After the publication of (Collier et al., 2018b), we acquired *HST* observations (PI: Smith) of J0403-0239. The imaging uses Wide Field Camera 3 (WFC3/UVIS) with the F814W and F390W filters, for 1040, and 3900 s respectively. The data are shown in Figure 6.4. From these images, the light profile can be inspected for any hints of the perturbations seen in the MUSE data, or recent star formation. Furthermore, a more complex approach to modelling the lens system will be adopted in this section.

The lens has a smooth light distribution in the red (F814W), and the extended lensed images have well-defined clumpy structure at shorter wavelengths (F390W). However in the F390W imaging, there are signs of irregular patchy dust obscuration running close to the lens galaxy near to the inner image (see right panel, Figure 6.4). This, in addition to the evidence from the MUSE datacube (patchy [NII] emission in the same direction, more distant from the lens) and wide-field imaging (more hints of tidal interaction) appear to strongly suggest this galaxy has been recently perturbed. This interaction could have simply been a 'dry' merger in which no gas is deposited and no further star-formation has occurred, or may have added a new supply of gas and triggered a burst of star formation, leading to a 'frosted' stellar population.

Already described in Section 6.5, with the MUSE discovery data we estimated the lensing mass with the assumption of a spherically symmetric model. The uncertainty incorporated GRAVLENS to describe the change in $M_{\rm Ein}$ due to a potential external shear. However Chapter 2 discusses PYAUTOLENS which incorporates both the information from the light profile of the lens and the lensed images to model the lens system. The bright extended lensed images are ideal for this style of analysis.

Using PYAUTOLENS we model the lensing system with a Sérsic profile for the light and

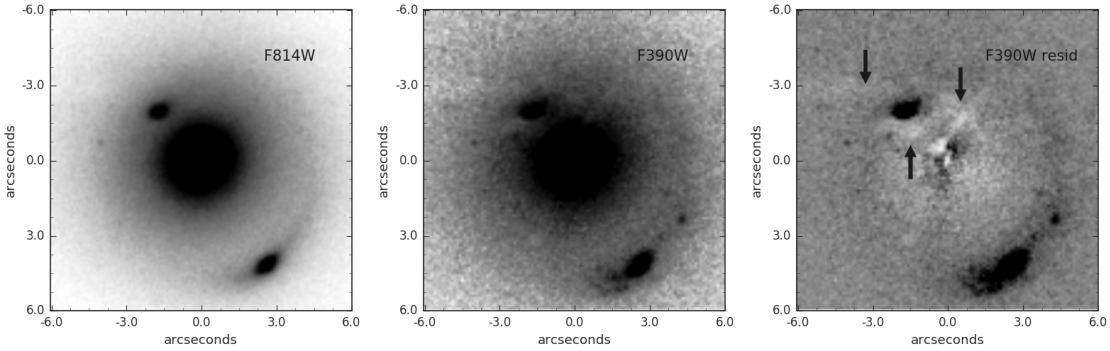

Figure 6.4: *HST* imaging for J0403-0239. *Left*: F814W *HST* data, showing a smooth lens light profile. The lensed images appear smooth, and a hint of a faint arc can be seen about the outer image. *Middle*: F390W *HST* data, displaying structure in the outer image. *Right*: A lens light subtracted image. The strongest evidence for a recent interaction is the clumpy residual which can be traced inside to the inner image, and a small plume more distant than the inner image (marked by the arrows). The residual is less notable in the F814W imaging.

a SIE mass profile. This method was discussed in Chapter 2. The source is fit with a Sérsic profile. The corresponding fit is shown in Figure 6.5, and the key image positions are reproduced to high accuracy, with residuals of order 2 per cent (some image complexity cannot be reproduced with the Sérsic model). The measured mass within R_{ap} is $M_{Ein} = 11.00 \pm 0.40 \times 10^{10}\,M_{\odot}$, where R_{ap} is the $R_{Ein} = 1.47 \pm 0.03$ measured from MUSE. With the improved lens modelling, the mass measured increased by 3 per cent, as compared to the GRAVLENS fit.

6.6.2 The Age of J0403-0239

A potentially much larger contribution to the uncertainty in α could stem from the age of the stellar population. In order to infer the IMF, the measured M/L must be compared to a Υ_{ref}. Changing the age of a stellar population from 12 Gyrs to ~3 Gyrs will change Υ_{ref} by almost of a factor of two. Therefore the age is a vital parameter to constrain.

We observed J0403-0239 with ESO/VLT FORS2. The wavelength coverage of the new data (3660 – 5110 Å) is blueward of MUSE (4750 – 9350 Å), and hence contains the higher order Balmer series and the Ca II doublet. These absorption features are key to precisely constraining the age of a stellar population. With the FORS2 data we can test our

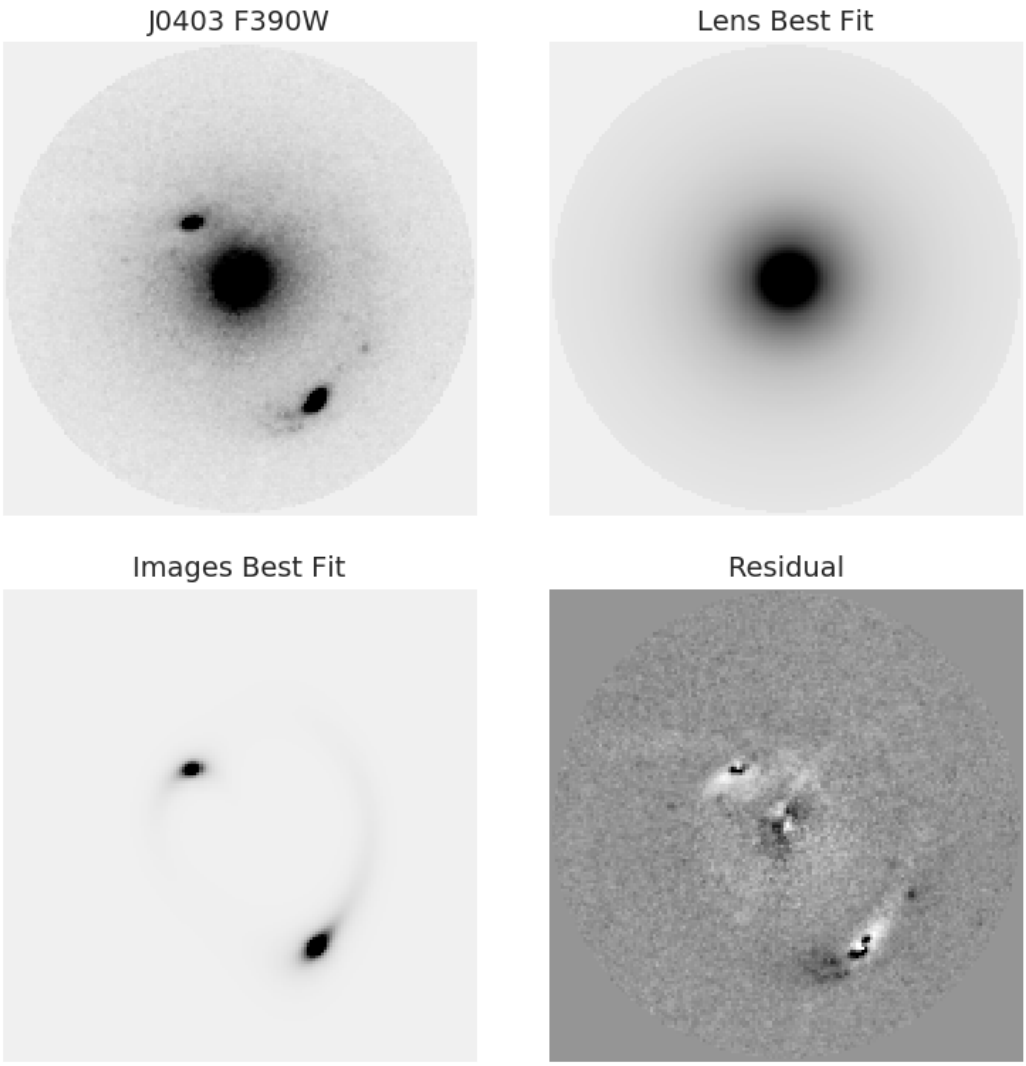

Figure 6.5: The PYAUTOLENS output for fitting the light profile and mass model of J0403-0239. a) The *HST* F390W data. b) The best fit model for the lens. c) The reconstructed lensed images for the best fit source. d) The residual from input image, when the best fit models for the lens and source are subtracted. The Sérsic source does not recover all of the structure seen in the outer lensed image, which is seen in the residual.

assumption that J0403-0239 has a single, old stellar population against the considerably younger luminosity-weighted age (old population 'frosted' with a considerably more recent starburst) which is measured from an extracted MUSE spectrum with STARLIGHT (Galbany et al., 2018).

We extract a spectrum within an aperture matched to the $R_{\rm Ein}$, covering the wavelength range 3900 – 5000 Å to include the high-order Balmer series, see Figure 6.6. As a simple comparison, we overlay the FORS2 spectrum with two different age SSPs from the MILES models (Vazdekis et al., 2010), assuming a bimodal IMF with a slope of –1.30. We select models which are α-enhanced, and metal-rich with ages of 2.75 Gyrs (Galbany et al., 2018, measured a 2.6 Gyr luminosity-weighted population) and 12 Gyrs (an old population was assumed by Collier et al., 2018b) which are redshifted to 0.066 and smoothed to $\sigma = 314\,{\rm kms}^{-1}$.

The FORS2 spectrum does not exhibit the strong Hγ and Hδ absorption expected from a < 3 Gyr stellar population, nor the strong high-order Balmer absorption characteristic of composite populations with < 1 Gyr components. Despite the evidence for a recent interaction or accretion event in J0403-0239, the FORS2 spectrum supports the assumption in Collier et al. (2018b) of an old stellar population inside the $R_{\rm Ein}$.

Investigating features in the spectrum by eye is an important first step, however a rigorous fit of the complete FORS2 spectrum is required to reliably constrain the age of the population. I select to work with the extended Conroy and Van Dokkum models, (Villaume et al., 2017), which cover a wide range of spectral features and abundances. The models are fit using PYSTAFF which is an open source python code developed to fit the stellar population of NGC 1399 (Vaughan et al., 2018).

The continuum shape of J0403-0239 is strongly affected by galactic dust. Using dust models from the Pan-STARRS and 2MASS surveys (Schlafly et al., 2014; Green et al., 2018), the continuum shape can be corrected for the reddening. However, even with this correction the shape of the spectrum is uncertain, and instead we match the continuum

Available from Sam Vaughan's GitHub https://github.com/samvaughan/PyStaff

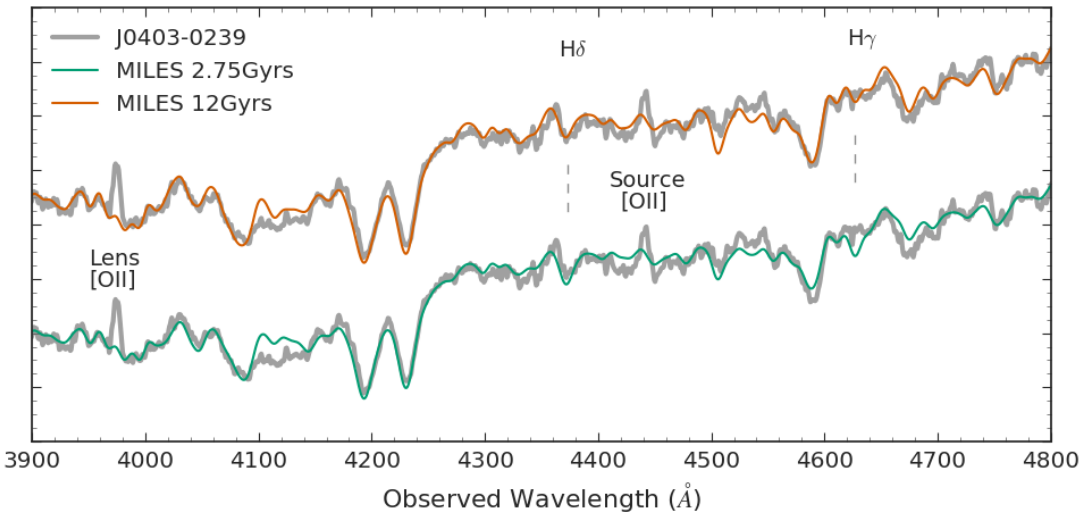

Figure 6.6: The recently acquired ESO/VLT FORS2 data for J0403-0239 extracted within $R_{\rm Ein}$, is displayed in grey. The data are not flux calibrated, and hence we match the continuum shape to an old stellar population. We compare the data with two differently aged SSPs from the MILES library (Vazdekis et al., 2010). The upper, is an old, 12 Gyr population which is α-enhanced and metal-rich. The lower, is a 2.75 Gyr population as suggested by Galbany et al. (2018). We label the H δ and H γ absorption features, which appear better matched by the older population.

shape of each model to the FORS2 data.

The fit is performed over the rest-frame wavelength range 3750–4600 Å, which covers all of the Balmer lines in the FORS2 wavelength range. We estimate an uncertainty on the spectrum from the variation between neighbouring pixels. We fix the IMF slope to Kroupa, and allow the velocity dispersion, metallicity and emission line strength of H β to vary during the fitting process. The best fit solution for the age is 12.5 ±0.3 Gyrs, with a velocity dispersion of 317 ±12 kms^{-1} and a metallicity of –0.07 ±0.10; the fit is shown in Figure 6.7. In each case these are the formal uncertainties within the PYSTAFF fitting. The bootstrapped uncertainty on the parameters are 50–75 per cent smaller.

We test if the fit is invariant to other variations of element abundances. We systematically remove parts of the spectrum which may influence the age of a stellar population. Removing the Ca doublet, or H β has no effect on the best fit age, within the uncertainty quoted. In addition, allowing the IMF slope to vary in the fits still returns fitted parameters for the slope consistent with Kroupa. Electing to vary or hold fixed element abundances of Na, Ca, Fe, C, N, Ti, Mg, Si and Ba also does not affect the age of the population outside of the

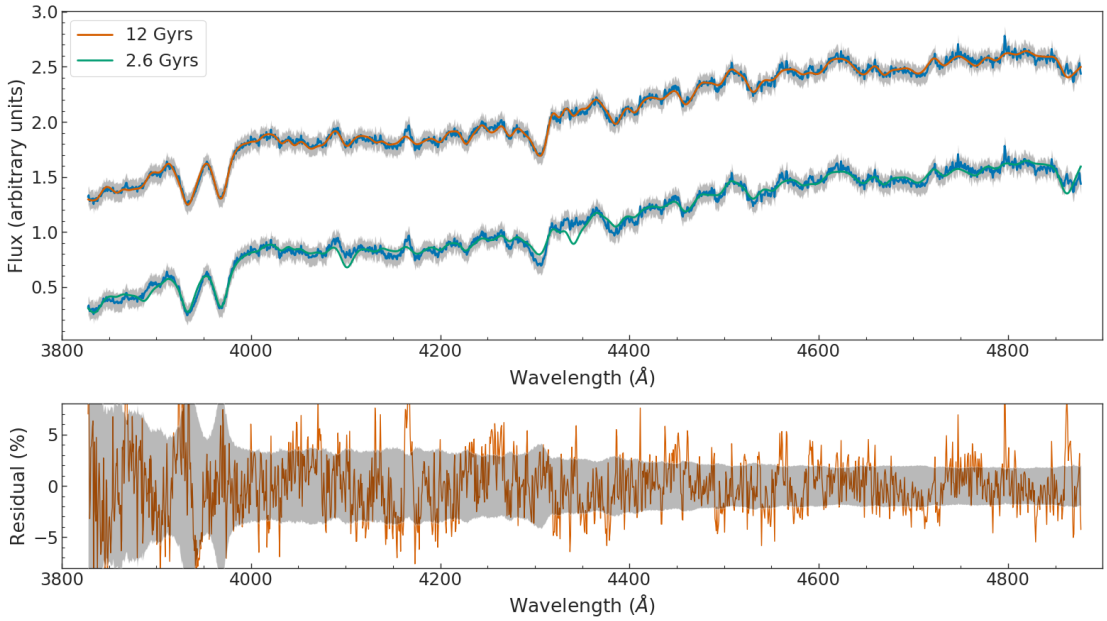

Figure 6.7: The FORS2 spectrum (3850–4890 Å) of the stellar population of J0403-0239 (black line) fit with PYSTAFF. Here, the models age is 12.4 Gyrs, with a metalicity Z = -0.06 and a velocity dispersion of 320 km/s, shown in blue. The 3 σ uncertainty region on the spectrum is shown in grey. In the lower panel, the residuals are shown, and are of order ±4 per cent.

uncertainty. The IMF slope and metallicity remain consistent with varying the wavelength range and element abundances.

6.6.3 Revisiting the stellar IMF

With the lensing mass revised, and the age confirmed we can now re-measure α. In order to compare to the previous measurement I will adopt R_{ap} to be 1.47 arcsec, which was the measured R_{Ein} from MUSE.

The new lensing mass is $M_{Ein} = 11.00 \pm 0.40 \times 10^{10}\,M_\odot$, and the age is confirmed as old, and hence $\Upsilon_{ref} = 2.58 \pm 0.10$ in WFC3 F814W. Using the *HST* data, with the previous k-correction, galactic reddening, and a correction for the lensed image flux, the aperture luminosity in F814W is $3.00 \pm 0.10 \times 10^{10}\,L_\odot$. The uncertainty is dominated by the applied corrections. Adopting the dark matter contribution from Section 6.5, the stellar M/L is $\Upsilon = 3.00 \pm 0.19\,M_\odot L_\odot^{-1}$.

The new α measurement will be independent of the previous data (only the selection of

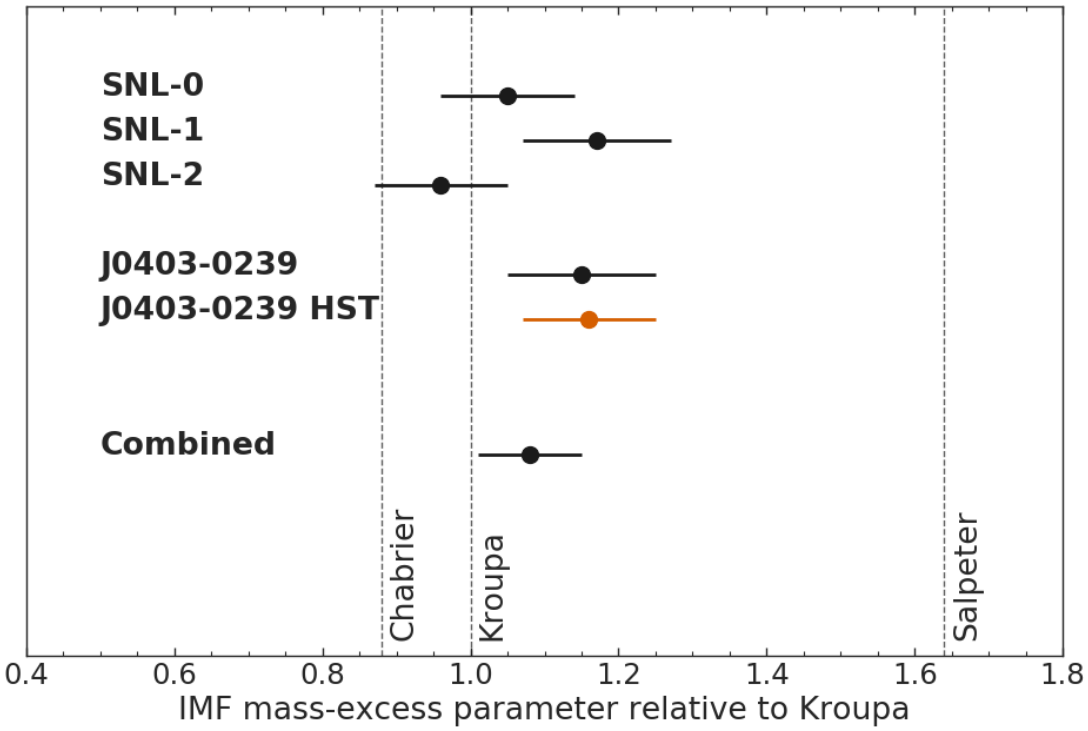

Figure 6.8: The distribution of the mass excess parameter (α) for the combined SNELLS and J0403-0239 sample. In black, is the SNELLS sample with results for SNL-0 from Newman et al. (2017), SNL-1, SNL-2 from Collier et al. (2018a), and J0403-0239from Collier et al. (2018b). The revised measurement of J0403-0239 is shown in orange. The sample average is $\langle\alpha\rangle = 1.08 \pm 0.08$, with an inferred *intrinsic* scatter of < 0.32, at 90 per cent confidence. These galaxies on average favour a Milky-Way like IMF in preference to a Salpeter or heavier IMF.

R_{ap} matches the MUSE R_{Ein}), and using a different software for the gravitational lensing. Using the quantities measured above, the inferred $\alpha = 1.16 \pm 0.09$, with a bootstrapped error. This is fully consistent with the previous measurement from MUSE, and is less than 1 per cent larger, see Figure 6.8. The revised intrinsic population mean, $\langle\alpha\rangle$, marginalised over the intrinsic scatter is 1.08 ± 0.08 for an assumed lognormal distribution.

6.7 Discussion and Conclusions

We have discovered a new low-redshift gravitational lens, with a bright background galaxy, and a small Einstein radius, probing the stellar-dominated core of a massive elliptical galaxy. From the discovery MUSE data and Pan-STARRS i–band imaging, we have

measured the lensing mass and the Einstein aperture luminosity to estimate the IMF mismatch parameter, $\alpha = 1.15 \pm 0.10$. We attribute a further uncertainty of (∼15 per cent) ± 0.17 for the systematics. Using the luminosity measured within follow-up imaging from *HST* (F814W) and extended source lens modeling, revised the estimate to $\alpha = 1.16 \pm 0.09$. Both measurements hence favour a lightweight (MW-like) IMF, rather than a heavy (e.g. Salpeter) one.

In comparison to the SNELLS systems, J0403-0239 is more distant ($z_{\rm lens} = 0.066$ vs 0.031–0.052), but the background source is at much lower redshift ($z_{\rm src} = 0.19$ vs 0.93–2.14). As a result, the Einstein radius is smaller in angular terms (1.5 vs 2.2–2.9 arcsec). Thus despite the greater lens distance, $R_{\rm Ein}$ projects to a similar radius in physical units (1.8 kpc vs 1.5–2.2 kpc) or in galaxy scale units (0.25 $R_{\rm Eff}$ vs 0.3–0.7 $R_{\rm eff}$). Like the SNELLS galaxies, J0403-0239 has high velocity dispersion and metal abundances typical for massive elliptical galaxies. Furthermore, the lensing aperture mass is compatible with the SNELLS results, favouring a MW-like IMF, and inconsistent with very bottom-heavy IMFs.

Combining our estimate of α for J0403 with the three estimates from SNELLS (taking the values from Newman et al., 2017; Collier et al., 2018a, i.e. SNL-0, SNL-1, SNL-2 = 1.05 ± 0.09, 1.17 ± 0.09, 0.96 ± 0.10), as shown in Figure 6.8, we can infer limits on the *intrinsic* distribution of this quantity among $\sigma \approx 300\,{\rm km\,s^{-1}}$ ETGs. We compute the joint likelihood of the four α measurements as a function of the unknown population mean $\langle\alpha\rangle$ and dispersion ν, accounting for the measurement errors. Marginalising over ν, with a flat prior, we infer $\langle\alpha\rangle = 1.08 \pm 0.08$ (the error is larger than for a calculation which assumes no intrinsic dispersion). Marginalising over the mean, we infer only an upper limit on the scatter, with $\nu < 0.32$ at 90 per cent confidence. (For comparison the same treatment applied to SNELLS alone yields an upper limit of $\nu < 0.7$, highlighting the impact of adding just one new measurement to the analysis.)

One important difference between J0403-0239 and the SNELLS sample, which is relevant for future work, is that the J0403-0239 arcs are both very bright and appear to be quite extended. Hence among all of the known low-redshift lenses, this system is uniquely suitable for pixelized lens inversion methods, which can yield much more powerful

constraints on the mass distribution (e.g. Nightingale et al., 2017; Oldham et al., 2017a). Upcoming observations with Hubble Space Telescope will provide high-resolution images for use in such studies.

6.8 Summary

The fourth low-z ETG strong-gravitational lens, J0403-0239, was discovered within public ESO/VLT MUSE archival data. The data were taken as part of a survey of supernovae hosts. The lensed images are sufficiently bright, in an extracted H α narrowband image, to be visible even without subtraction of the lens light. The lens is at $z = 0.06604$, which is more distant than the SNELLS systems, however, the background emitter is significantly closer, at $z = 0.1965$. Therefore $R_{\rm Ein}$ is one-quarter of $R_{\rm Eff}$ which is consistent with the SNELLS systems.

The analysis of this system as discovered in the MUSE data and followed up with *HST* observations provides a robust constraint on the stellar mass-to-light ratio. Using the ESO/VLT FORS2 data we constrain the age of the stellar population to be 12 Gyr. We find that the mass-excess parameter of the galaxy is inconsistent with a Salpeter IMF at $> 4\sigma$ significance given the measurement uncertainties, and $> 2\sigma$ given the systematic uncertainties.

Assuming a model distribution, the intrinsic mean and scatter of α within the ETG population is constrained using the four low-z lenses. In the following chapter, I combine the 'upper limit' systems with the lenses to improve the constraints on the distribution of α.

CHAPTER 7

The IMF within the ETG population

This chapter is based on section 5 of *MNELLS: The MUSE nearby Early-Type Lens Locator Survey* (Collier et al., 2020).

7.1 Preamble

There are four known multiply imaged low-z ETG strong lenses with $\sigma \simeq 300\,\mathrm{km\,s^{-1}}$. The distribution of mass-to-light ratios inferred from this sample has an intrinsic mean of $\langle\alpha\rangle = 1.08 \pm 0.08$ and an intrinsic scatter of $\nu < 0.32$. However, the predicted IMF of the total population appears to be overestimated when only lenses are considered (Sonnenfeld et al., 2019).

The 'upper limit' analysis presented in Chapter 5 provides nine systems to improve the constraints on the distribution of α within the ETG population. A further two systems, SNL-4 and MaNGA target J0728+4005, were analysed by Smith et al. (2018) with a consistent method. Here, all of the systems presented in the previous chapters (excluding the cluster-scale lenses) are incorporated into a single fit for the intrinsic population of $\sigma \simeq 300\,\mathrm{km\,s^{-1}}$ ETGs.

7.2 Introduction

The difference between SNELLS-like and SLACS-like lenses are the resulting IMF mass-excess parameters measured from lensing analysis, see Section 1.6. The SNELLS systems, which are consistent with a MW-like IMF, are currently few in number. The SLACS coverage of $\sigma \simeq 300\,\mathrm{km\,s^{-1}}$ is also limited, motivating new lens searches around massive ETGs. As the current sample size is small, the inferred population for massive ETG lenses has a sizeable intrinsic scatter and does not rule out the Salpeter-like lenses being drawn from the distribution.

The addition of a fourth low-z lens, J0403-0239, constrained the population mean sufficiently to demonstrate a deviation from a Salpeter-like IMF at a $> 5\sigma$ level. However, the intrinsic scatter remains large, ~ 0.32, due to small number statistics. While increasing the sample size is key to reduce the effect of small number statistics, the 'upper limit' systems offer an alternative approach to improve the constraint on the intrinsic scatter.

The strongest IMF constraints are from multiply imaged strong gravitational lenses. However, analysis of systems with only a single close-projected emitter produces an 'upper limit' of the 'lens' M/L. The limit is predicted by scaling the mass profile in M/L, and testing if a counter-image is *not* detectable. In turn, this translates to a maximal mass-to-light ratio excess parameter (α), and constrains further the IMF in ETGs.

In the SLACS lens search, 'grade-A' lenses were confirmed multiply imaged systems (Bolton et al., 2006). However, they also discovered a number of singly imaged background sources, named 'grade-C' lenses. The stellar masses of the grade-C lenses were predicted probabilistically (see Shu et al., 2015). The results from analysing the grade-C systems were consistent with the 'grade-A' lenses.

In this chapter, the intrinsic population of ETGs are inferred by combining the multiply imaged lenses with the singly imaged but close-projected systems. Section 7.3 introduces each of the galaxies which have not been previously discussed but are included in the forthcoming analysis. In Section 7.4, the intrinsic population is constrained with a log-

normal distribution.

7.3 The additional galaxies

In the preceding chapters, three lenses—SNL-1, SNL-2 and J0403-0239—and nine singly imaged but close-projected systems are analysed. We include a fourth strong lens for the analysis in this chapter, SNL-0, and a summary of its discovery and subsequent analysis is provided here. 'Upper limit lensing' was introduced with a sample of three galaxies, SNL-4, J0728+4005 and J0202-0107 (Smith et al., 2018). We re-analysed J0202-0107 in Chapter 5, and SNL-4 and J0728+4005 are introduced here.

7.3.1 SNL-0

The near-complete Einstein ring around the $z = 0.035$ massive elliptical galaxy ESO325–G004 was a serendipitous discovery. Observed with the Advanced Camera for Surveys (ACS) onboard *HST* (Smith et al., 2005), the lensed arcs are distinct in colour from the foreground lens at a radius of approximately one-quarter of $R_{\rm Eff}$. The background source redshift was measured with X-SHOOTER as $z = 2.141$. The stellar population was fit, with a VIMOS spectrum, to be old (~ 12 Gyrs), and the mass-excess parameter was measured to be $\alpha = 1.05 \pm 0.09$. This measurement disfavours a Salpeter or heavier IMF at the $5\,\sigma$ level (Smith & Lucey, 2013; Smith et al., 2015). SNL-0 was analysed with stellar dynamics and stellar population modelling.

Analysis combining stellar dynamics and lensing produced a result consistent with lensing alone. However, the stellar population synthesis modelling favours a heavy IMF with a mass larger than $M_{\rm Ein}$ (see table 1, Newman et al., 2017). The tension between spectral fitting and the lensing analysis is alleviated if Na I is removed from the fitting.

In this section, the lensing measured α value is taken as 1.05 ± 0.09.

7.3.2 SNL-4

Two new strong lenses, SNL-1 and SNL-2, and a single-imaged closely-projected lens, SNL-3, were discovered by SNELLS (Smith et al., 2015). In a second observing programme with the same selection, 2MASX J04431291-1542101 (hereafter SNL-4) was discovered to have a single emitter separated by 4.25 arcsec.

Whereas SNL-3 was dominated by a central dust lane, SNL-4 displays a very regular elliptical morphology. SNL-4 has a redshift of 0.037, and the background source lies at $z = 1.38$ (Smith et al., 2018). The system was fitted with a $r^{1/4}$ power law mass profile. The 50 per cent probability upper limit is $M/L = 1.8$. However, there is a tail to the distribution beyond $M/L = 2.3$ when the counter-image leaves the FoV (see figure 4, Smith et al., 2018).

7.3.3 J0728+4005

The MaNGA survey targets ETGs with a broad range in velocity dispersion. The sample has been searched for strong-lensing systems, and for several cases only a single source was discovered (Talbot et al., 2018). The most massive galaxy with the closest projected background source was 2MASX J07281702+400502, hereafter J0728+4005, which has a velocity dispersion of 268 km s^{-1}. The 'lens' has a redshift of 0.05, and the background emitter is situated at $z = 0.954$. The system has an 'upper limit' 50 per cent threshold close to $M/L = 1.3$. However, the probability remains > 20 per cent for much of the M/L range and so no firm estimate could be obtained (see figure 6, Smith et al., 2018).

7.4 The ETG population

The *intrinsic* distribution of the IMF within ETGs can be inferred from the four confirmed low-z lenses (taking Υ values for SNL-0, SNL-1, SNL-2, J0403-0239 from Newman et al., 2017; Collier et al., 2018a,b). Assuming a normal distribution and a flat prior on the

mean, and marginalising over the intrinsic scatter, we find $\langle\alpha\rangle = 1.09 \pm 0.08$. Alternatively, by marginalising over the mean, the 90 per cent upper limit on ν is 0.32 (29 per cent). However, if there is a sizeable scatter in the IMF within the ETG population, then the lensing systems are likely to be biased towards those with the highest mass. This was found by Sonnenfeld et al. (2019), who compared the SLACS lens population to weak lensing of non-strong-lensing ETGs. Therefore, combining the 'upper limits' and the confirmed lenses may better constrain the *ensemble* population (see also Shu et al., 2015). Here, we use seven of the nine upper limit systems presented in this paper. Due to the lack of constraint even at the top of our M/L range, we do not include J0627-5426 and J1352-3456. We add the two systems analysed in Smith et al. (2018) from other surveys (SNL-4 and J0728+4005) along with the four confirmed lenses.

We model the intrinsic population as a log-normal (base e) distribution in α, described with a mean, $\langle\alpha\rangle$, and an intrinsic scatter, ν, as currently there are too few systems to constrain the shape of the distribution. A log-normal distribution is physically motivated as it cuts off at $\alpha = 0$. However, modelling α with a normal distribution does not significantly affect the results. We set flat priors on $\langle\alpha\rangle$ and ν, for the ranges $[0, 2.5]$, and $[0, 0.5]$, respectively. The derived α value for each lens is either measured directly from lensing analysis, or indirectly inferred from the 'upper-limit' analysis, see the shaded regions in Figure 7.1a. Systems comparable with J0202-5055, which have tight upper-limits on α that are *comparable* with those measured from confirmed lenses, offer the most information.

For each confirmed lens, we estimate the likelihood of drawing $\alpha_{\rm meas}$ from the intrinsic population, $P(\alpha|\langle\alpha\rangle,\nu)$, with a broadening on ν from the uncertainty in the measurement. A grid-based exploration of $\langle\alpha\rangle$ and ν with step size 0.01 produces the dashed contours shown in Figure 7.1b. The intrinsic distribution, marginalised over ν, has $\langle\alpha\rangle = 1.07 \pm 0.09$, shown in Figure 7.1c, which is consistent with the result of $\langle\alpha\rangle = 1.09 \pm 0.08$ from Collier et al. (2018b) for the same lenses.

To include the upper limits, a slightly more complex approach is required. The probability

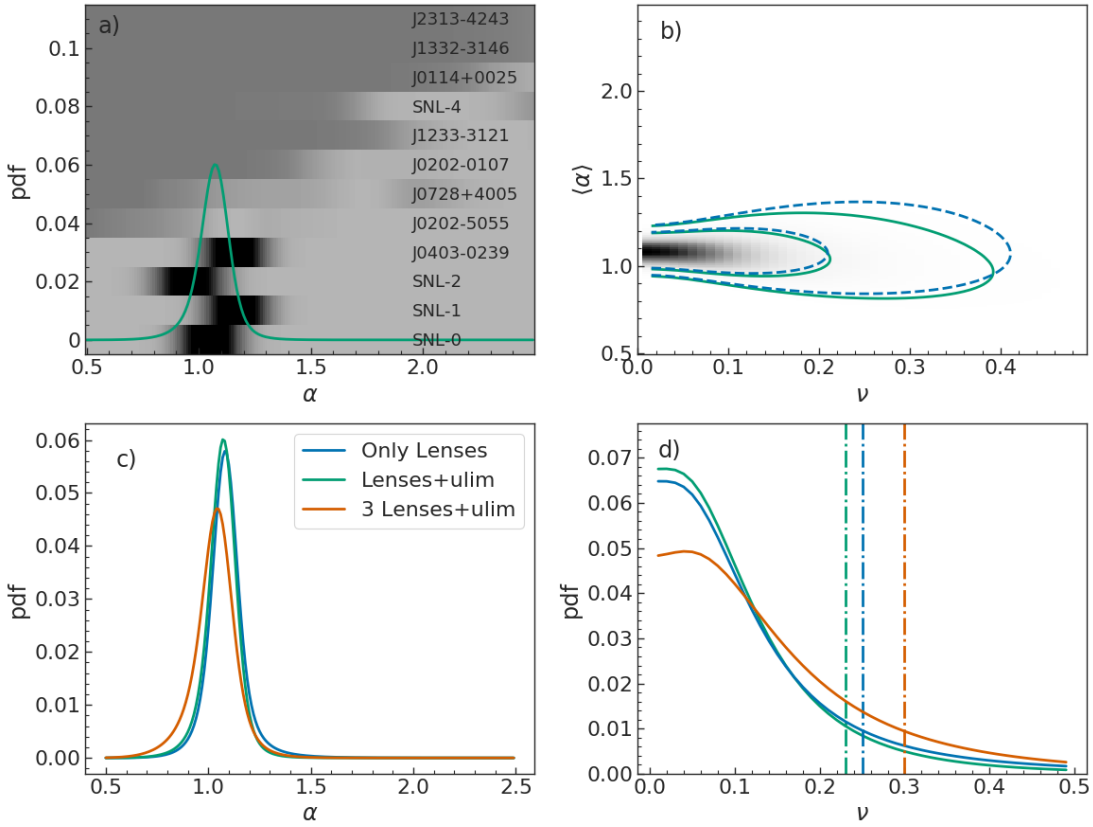

Figure 7.1: The distribution of α for the population of both lenses and single-imaged systems. Values calculated with just the four lenses are in blue, the four lenses combined with the upper limit analysis is green, and analysis on the sample after removing J0403-0239, leaving 3 lenses and the upper limits is displayed in orange. *Panela*) The intrinsic distribution of α for the lenses and 'upper limit' systems. The shaded background regions show the probability of a given alpha for the lenses (lowest four), or upper limit analysis. *Panelb*) Contours showing the distribution in $\langle\alpha\rangle$ and ν (the intrinsic scatter) space with and without the 'upper limit' analysis. The twist to lower α at higher ν can clearly be seen. *Panelc*) The intrinsic distribution in α as we change the sample. Removing the lens J0403-0239 has the largest effect, and shifts the distribution to favour lower α. Adding the upper-limits shifts the peak of the distribution to lower α, compared to just the lenses. This is due to the significant effect of J0202-5055. *Paneld*) The predicted intrinsic scatter of the distribution in base e, with dashed lines at the 90 per cent confidence interval for each case. As can be seen, adding the upper-limits favours a population with a smaller scatter than just the lenses. Removing J0403-0239, and including the upper-limits increases the intrinsic scatter significantly (30 per cent).

of a given $\langle\alpha\rangle$ and ν combination ($P_i(\langle\alpha\rangle,\nu)$) is now given by

$$P_i(\langle\alpha\rangle, \nu) = \int U(\alpha_i)P(\alpha_i|\langle\alpha\rangle, \nu)d\alpha_i, \tag{7.4.1}$$

where $U(\alpha_i)$ is the likelihood for a galaxy to have a given α (in the range $[0, 3.0]$), from the 'upper limit' analysis. This is related to $U(M/L)$ by a convolution with a Gaussian uncertainty contributed by $\Upsilon_{\rm ref}$. Including this likelihood allows us to marginalise over the unknown true value of α for each galaxy.

The distribution from the upper limits alone is strongly skewed towards low $\langle\alpha\rangle$. Therefore, combining this with the confirmed lenses skews the overall distribution towards lower $\langle\alpha\rangle$ (see Figure 7.1c), which also reduces the intrinsic scatter, ν. The combined distribution has a mean of $\langle\alpha\rangle = 1.06 \pm 0.08$, shown in Figure 7.1a. The 90 per cent confidence upper limit on ν is 0.24 (20 per cent). This is a nine per cent decrease compared to using only the four confirmed lenses.

We consider what finding additional single-imaged galaxies might do to the distribution by testing the addition of hypothetical systems consistent with those presented in this paper. If we add new hypothetical systems consistent with J2313-4243, we find that these do not change $\langle\alpha\rangle$ or ν. However, adding four hypothetical systems alike to J0202-0107, where the 20 per cent probability for a non-detected counter image lies at $\alpha = 1.5$, reduces the inferred intrinsic scatter in the population, without changing $\langle\alpha\rangle$. Finally, additional hypothetical systems consistent with J0202-5055 and J0728+4005 will *increase* ν and *reduce* $\langle\alpha\rangle$, as the upper-limits suggests that they formed with IMFs lighter than $\langle\alpha\rangle$ predicted from only the confirmed lenses.

Our analysis demonstrates that the strong-lens systems favour a comparably heavier IMF than those systems which include only a single emitter. The population of low-z strong lenses are offset, by 8 per cent, from M/L predicted by a Kroupa IMF. However, these are biased towards a higher α, and the distribution has a smaller mean. The population of low-z strong lenses are offset to larger M/L than predicted by a Kroupa IMF (by 8 per cent). However, these are biased towards a higher α, and the distribution has a smaller mean. Therefore, the *ensemble* population lies in closer agreement with the Kroupa IMF. Our

distribution of $\langle\alpha\rangle = 1.06 \pm 0.08$ is within 3σ of similar attempts to combine strong-lensing constraints with other independent techniques (e.g. Sonnenfeld et al., 2019, who found $\alpha = 0.80 \pm 0.11$).

7.5 Conclusions

In this chapter, we combined the four confirmed lenses with seven singly imaged but close-projected systems from chapter 5, and two, (SNL-4 and J0728+4005), taken from Smith et al. (2018). to infer the ETG population, assuming a log-normal distribution for α. The population has $\langle\alpha\rangle = 1.06 \pm 0.08$, and a 90 per cent confidence intrinsic scatter of $\nu = 0.24$.

The addition of the 'upper limits' reduces the previous $\langle\alpha\rangle = 1.08 \pm 0.08$ and $\nu < 0.32$ from only the confirmed lenses in Chapter 6. This implies that there is a higher likelihood of discovering strong lensing around massive galaxies with higher stellar mass (or more compact) due to their increased surface mass-density. Therefore, as SNELLS and MNELLS lenses on average measure α a few per cent larger than MW-like, the total population lies even closer to a MW-like IMF.

The change in $\langle\alpha\rangle$ is driven by the most restrictive upper limits, with the intrinsic scatter only being affected by systems consistent with, or lighter than, J0202-0107. We also show that removing a lens has a significantly greater impact on the distribution parameters than all nine 'upper limit' systems. The addition of four hypothetical lenses consistent with SNELLS and J0403-0239 reduce the intrinsic scatter ν to 0.12. For a population described by this P($\langle\alpha\rangle = 1.06, \nu = 0.12$), a measurement consistent with a Salpeter-like IMF is a $5\,\sigma$ outlier.

7.6 Summary

In this chapter, the 'upper limit' lenses were combined with the low-z lenses to investigate the intrinsic ETG population. The measured parameters are $\langle\alpha\rangle = 1.06 \pm 0.08$, with a 90

per cent confidence upper limit on the intrinsic scatter of $\nu = 0.24$. These parameters do not rule out the SLACS lenses being drawn from the low-z population.

The 'upper limits' reduce the intrinsic mean and scatter. However, this is driven by the systems with the tightest constraints, i.e. J0202-5055. A single, well-characterised lens has a greater impact on the intrinsic mean or scatter than nine 'upper limit' systems.

CHAPTER 8

Conclusion

8.1 Overview

This thesis presented an investigation of the IMF within the central, stellar dense core of massive ($\sigma = 300\,\mathrm{kms}^{-1}$) ETGs. In low-$\sigma$ ETGs, the IMF is MW-like whether inferred by spectral features, stellar dynamics or gravitational lensing (Treu, 2010; Conroy & van Dokkum, 2012a; Cappellari et al., 2012). However, all three studies also found a trend of increasing stellar mass-to-light ratios (Υ) with velocity dispersion, inferred as requiring an increasingly 'heavy' IMF. The cores of massive ETGs are typically measured with Υ up to twice that predicted for a MW-like IMF.

The focus was on using low-z strong gravitational lenses to precisely measure Υ and hence make inferences about the IMF. The IMF mass-excess parameter, α, is defined as

$$\alpha = \frac{\Upsilon}{\Upsilon_{\mathrm{ref}}}, \tag{8.1.1}$$

where Υ_{ref} is the stellar mass-to-light ratio for a model stellar population with a MW-like (Kroupa) IMF. The previous massive low-z lenses, from the SINFONI Nearby Elliptical Lens Locator Survey (SNELLS, Smith et al., 2015), have α consistent with a MW-like

IMF.

The work is composed of two complementary parts. First, a lensing analysis of two previously known low-z lenses, SNL-1 and SNL-2, using follow-up *HST* data. Second, a MUSE-based lens search, using data from a targeted blind survey and the ESO archive. The archival search yielded the fourth low-z ETG strong gravitational lens, J0403-0239. In this chapter, I will provide a summary of this thesis, and suggest some future work which will further address the questions posed in Chapter 1, which are repeated below.

- Are the SNELLS lenses robust against improved lens modelling and the inspection of higher-resolution photometry?
- Can the SNELLS search techniques be applied to other IFUs successfully?
- Are the three currently known SNELLS lenses outliers of the intrinsic population?
- Is the IMF a universal quantity?

8.2 Summary of the Presented Work

8.2.1 The SNELLS lenses

The SNELLS sample comprises three strong gravitational lenses. SNL-0 was a serendipitous discovery within *HST* data (Smith et al., 2005). The lens is a $\sigma = 335\,\mathrm{kms}^{-1}$ elliptical galaxy at $z = 0.034$. The background source, $z = 2.141$, is lensed to a near-complete Einstein ring. The most up-to-date lensing IMF measurement for SNL-0 is $\alpha = 1.05 \pm 0.09$ (Newman et al., 2017). The other two lenses SNL-1 and SNL-2 were discovered during a blind search for lensed emitters with SINFONI. SNL-1 is a $\sigma = 280\,\mathrm{kms}^{-1}$ S0 at $z = 0.031$. The background source is at $z = 0.926$ and is doubly imaged. For this system, $\alpha = 1.18 \pm 0.12$. SNL-2 is a $\sigma = 274\,\mathrm{kms}^{-1}$ elliptical, at $z = 0.052$. SNL-2 has a similar-brightness close companion. The source is doubly imaged, at $z = 1.969$. The IMF mass-excess parameter is $\alpha = 0.96 \pm 0.14$. The spectra of all three systems are very similar to massive ETGs selected

from SDSS. When compared to a stack of SDSS galaxies with similar velocity dispersion, the residual has only a 0.32 per cent rms (Newman et al., 2017).

The previous lensing analysis of Smith et al. (2015) used image positions measured from the SINFONI data, which had a 0.25 arcsec pixel scale. As the source in each system is doubly imaged, the amplitude and position angle of the external shear and the lens mass could not be constrained without a degeneracy. Hence, the aperture lensing mass for SNL-1 and SNL-2 had relatively large associated errors of $0.4 \times 10^{10}\,\mathrm{M}_{\odot}$ and $1.2 \times 10^{10}\,\mathrm{M}_{\odot}$, respectively.

Chapter 3 presented a new analysis of SNL-1 and SNL-2 from SNELLS. The stellar mass-to-light ratio (Υ) was measured by combining lensing constrints and photometry from new *Hubble Space Telescope* imaging (in F814W, and F336W/F390W filters for SNL-1/SNL-2, respectively).

SNL-1 has two compact lensed images. The lensed-image separation is 4.86 arcsec, when measured from the *HST* imaging. This is 2 per cent larger than measured with the poorer resolution SINFONI data. The brighter background source shows some spiral structure, whereas the fainter inner image has little to no structure. The relative flux between the lensed images was used to constrain the external shear. Using GRAVLENS with SIS, SIE and MFL profiles the lensing mass was measured as $M_{\mathrm{Ein}} = 9.49 \pm 0.15 \times 10^{10}\,\mathrm{M}_{\odot}$. The uncertainty is calculated from the flux ratio, and the model-to-model scatter. Compared with Υ_{ref} from Newman et al. (2017), $\alpha = 1.17 \pm 0.09$, which is 3 per cent smaller than 1.20 ± 0.13 found by Smith et al. (2015).

SNL-2 has two compact, unresolved lensed images. The *HST* measured lensed-image separation was 4.60 arcsec. This is 4 per cent larger than the SINFONI measurement. Due to the similar brightness galaxy separated by 7 arcsec, SNL-2 has a more complex lensing configuration than SNL-1. In this system, the external gravitational effects will be dominated by the companion, and hence the flux constraints were used to constrain the mass of the companion. The lensing mass is measured to be $M_{\mathrm{Ein}} = 12.59 \pm 0.30 \times 10^{10}$ $\mathrm{M}_{\odot}$ for a MFL lens, and an SIE or MFL companion. The derived α is 0.96 ± 0.10, which is a 2 per cent increase upon 0.94 ± 0.17 measured by Smith et al. (2015).

Both SNL-1 and SNL-2 remained consistent with the MW-like IMF inferred from the SINFONI data. Each deviates by more than 3 σ from Salpeter or 'heavier' IMFs.

8.2.2 A new lens search

Chapter 4 introduced the MUSE nearby early-type lens locator survey, MNELLS. This is a direct follow-on of the SNELLS survey, which discovered two low-z ETG strong lenses. MNELLS was a poor weather programme which blindly targeted 16 ETGs, selected by redshift ($z < 0.060$), and velocity dispersion ($\sigma > 300\,\mathrm{kms}^{-1}$). To supplement the MNELLS search, we selected 36 galaxies from the ESO archive, by redshift ($z < 0.07$) and 2MASS absolute K-band magnitude (K < –25.4). The foreground galaxy was subtracted slicewise, and the residual datacube was searched for background emission-line objects.

The systems of interest discovered within the survey separate into three categories: multiply imaged galaxy-scale lenses, multiply imaged cluster-scale lenses, or singly imaged background sources close-projected to the foreground galaxy (within 6 arcsec). One galaxy-scale lens, J0403-0239, three cluster-scale lenses and nine systems with a singly imaged but close-projected source were discovered (see Chapter 5). While J0202-5055 had been observed previously with SINFONI, the MUSE wavelength coverage revealed two previously unknown background sources. The emitter projected closest, at $z = 0.29$, is separated by 1.92 arcsec . This would lie within the SINFONI FoV, but outside of the wavelength coverage.

The cluster-scale lenses are J2357-3445, J1516+0701, and J0557-3728. There are the cluster BCGs of A4059, A2025, and S555, respectively. J0557-3728 has a complex lensing configuration, and therefore no further analysis was presented. J2357-3445, $z = 0.0491$, has two lensed images, separated by 17.15 arcsec at $z = 0.512$. For an assumed SIE profile and a Salpeter IMF, the mass-excess parameter implied a 76 per cent dark matter (DM) contribution. This increases if a MW-like IMF is assumed, see Table 5.2. J1516+0701, $z = 0.0345$, has a pair of lensed images separated by 19.4 arcsec at $z = 1.376$. In this system, a 78 per cent DM contribution is required for a stellar mass-to-light ratio consistent with a

Salpeter IMF. For the cluster-scale lenses, disentangling the DM from the cluster,and the galaxy is complex and uncertain. Therefore, no inference about the IMF was drawn from these systems.

The nine single-imaged but close projected systems were presented in Chapter 5. For each system, a MFL profile was scaled for a range of M/L, with a fixed observed image position. The output lensing configurations were tested for a non-detection of a counter-image. This does not make a direct measurement of the Υ of each system, but it does give a probability distribution over the range of M/L. No DM contribution is applied to these systems.

To investigate the effectiveness of the MNELLS search technique the detection threshold was tested and compared to the MUSE-wide survey (Herenz et al., 2017). The estimated yield of strong lenses was predicted to be one in every twenty-five observations. The MNELLS background was significantly higher than the MUSE-wide survey over the full spectral range. Particularly the blue end was affected by a high lunar continuum. However, this likely only affected the detection of Ly α sources, as low-z [O II] emitters may have been identified from [O III] or H α emission in the lower background redder channels. There was also a 0.35 dex reduction measured in the sensitivity towards the centre of the galaxy, which limits our detection of faint counter-images.

8.2.3 A new lens and the IMF

Chapter 6 presented the discovery of J0403-0239, a $z = 0.0665$ massive elliptical, with a pair of background sources at $z = 0.1965$. The lensed images are separated by 2.94 arcsec and show some radial structure. The projected $R_{\rm Ein}$ is one-quarter of the lens $R_{\rm Eff}$. Initially using MUSE data and Pan-STARRS1 imaging, and then with *HST* imaging, the measured Υ is consistent with a MW-like IMF for an assumed old stellar population.

Using a spectrum extracted from ESO/VLT FORS2 data, we found a best fit age of 12.5 $\pm$0.3 Gyrs. Taking $\Upsilon_{\rm ref}$ for an old stellar population and the Υ measured from the *HST* data, $\alpha = 1.16 \pm 0.09$, which deviates at a significance of 5 σ from a Salpeter IMF; $\alpha = 1.64$ for Conroy et al. (2009) models. From the MUSE spectrum alone, Galbany et al. (2018)

measured a light-weighted age of 2.6 Gyr. However, this was ruled out by the age-sensitive blue coverage of the higher-order Balmer lines and Ca H and K absorption features within the FORS2 data.

J0403-0239 was combined with the three SNELLS lenses to infer the α distribution of $\sigma \simeq 300\,\mathrm{kms}^{-1}$ ETGs. The mean of the population is $\langle\alpha\rangle = 1.08 \pm 0.08$, when marginalising over the intrinsic scatter, ν, the uncertainty is larger than for a calculation which assumes no intrinsic scatter. The upper limit on the scatter, is $\nu < 0.32$ at 90 per cent confidence.

In Chapter 7, all systems analysed in Chapters 5, and 6 were combined, along with two additional low-z systems from Smith, Lucey & Collier (2018). The 'upper limits' were treated as α probability distributions. The population has $\langle\alpha\rangle = 1.06 \pm 0.08$ and an upper limit on the intrinsic scatter of $\nu = 0.24$ at 90 per cent confidence. Incorporating the 'upper limit' systems reduced the intrinsic scatter by 25 per cent. Salpeter-like IMFs are $2.4\,\sigma$ outliers for a population described by P($\langle\alpha\rangle$,ν).

8.2.4 Discussion of the main results

This thesis addressed the four main questions relating to the IMF within massive ETGs. In Chapter 3, the lensing analysis from the lower-resolution IFU data was found to be robust when compared to higher-resolution imaging from *HST*. The SNELLS technique was successfully applied to MUSE and is being extended to FOCAS IFU data attained on Subaru (Smith et al., 2020). The 'upper limits' and J0403-0239 are consistent with the SNELLS lenses. They do not appear to be outliers from this distribution. The following section will discuss the results with regards to other studies.

The combination of four low-z lenses and 'upper limits' measure $\langle\alpha\rangle$ to be consistent, at $1\,\sigma$, with a MW-like IMF. However, the intrinsic scatter of 0.24 does not rule out a broad distribution in α. This sizeable scatter would imply a range of star formation conditions across ETGs, and not a single universal IMF. However, 'heavyweight' IMFs ($\alpha = 2$) are ruled out at the $4\,\sigma$ level. A comparable result of $\langle\alpha\rangle = 0.80 \pm 0.11$ (converted to $\alpha = 1$ for a Kroupa IMF, Sonnenfeld et al., 2019), was found by investigating the Baryon Oscillation

Spectroscopic survey constant mass sample.

The total lensing mass for each of the low-z lenses, with no contribution attributed to DM, is inconsistent with a Salpeter IMF at $> 1\,\sigma$. This suggests that the stellar mass component within $R_{\rm Ein}$ is overestimated in the SLACS sample. The stellar masses measured with lensing and stellar dynamics for 45 SLACS lenses were compared with the weak-lensing measurements for a sample of 1700 massive quiescent galaxies (Sonnenfeld et al., 2018). The study found, to simultaneously model both samples, a radial Υ gradient must be incorporated into the stellar dynamics. These gradients *increase* the Υ with decreasing radius. This reduces the stellar mass in the centres of the SLACS lenses. Hence, this drives the α parameters measured for SLACS closer to Kroupa-like, although the precise size of this shift is dependent on the assumed DM halo structure. These gradients will also reduce the α measured directly from stellar dynamics.

Similar radial Υ gradients to those observed in the SLACS lenses may be present in the low-z lenses. To date, only one low-z lens has been analysed with radial gradients. For SNL-0, the gradient was found to be centrally concentrated ($< 0.2\,R_{\rm Eff}$) and steep (Collett et al., 2018). The modelling suggested a 3 per cent DM contribution within $R_{\rm Ein}$, significantly lower than the projected DM mass within simulated halos (~ 20 per cent Smith et al., 2015). The mass excess parameter within $R_{\rm Ein}$ was $\alpha = 1.30 \pm 0.1$, which deviates from Salpter at a significance of $> 2\,\sigma$. A similar analysis of SNL-1 and SNL-2 will investigate the potential Υ gradients within MUSE data, and provide a single self-consistent model for the stellar population, dynamics and lensing (Oldham, in prep.). The lensing analysis implies that any variation will be centrally concentrated as MW-like IMFs were inferred.

The radial Υ gradient in SNL-0 increases α, in contrast to the SLACS lenses for which a gradient reduces the measurement. The varied effect of Υ gradients was also reported in the early-type/early-type galaxy lens sample, (Oldham & Auger, 2018). Therefore, introducing radial gradients into the dynamical modelling and incorporating the dynamics for the low-z lenses could draw the results closer to the re-analysed SLACS lenses. Further analysis of the low-z lenses is required as the previous lensing and dynamics study assumed a constant Υ (Newman et al., 2017). To compare low-z lenses to a large population and

infer population parameters, following the Bayesian hierarchical approach of Sonnenfeld et al. (2018), additional lenses need to be discovered.

This thesis was unable to answer the question "Is the IMF universal?". However, it discovered a new low-z strong lens, and provided an up-to-date and robust determination of the distribution of the IMF with the ETG population. With only four lenses, and nine single-imaged systems, there remains a sizeable intrinsic scatter. However, adding four new lenses with α mass excess parameters consistent with the low-z lenses, the upper limit on the intrinsic scatter would be 0.12. This will place heavier than MW-like IMFs, i.e. Salpeter, as $> 5\,\sigma$ outliers.

8.3 Continuation and future work

8.3.1 MNELLS continued

The MNELLS observations presented in this work are from ESO P101. There were observations of 21 galaxies in ESO P103 and P104. The initial analysis found no objects of interest. However, including these observations will improve the constraints on the number density of background sources, and hence refine future searches. With 37 MNELLS observations, 1.5 lenses are expected, and zero have been discovered. This is within the Poisson uncertainty.

For ‘upper limit’ lensing, the choice of model introduces an intrinsic uncertainty. The contribution of a specific model is yet to be fully explored. For example, the results in Chapter 4 show that selecting a free or an n = 4 Sérsic profile has a 5 per cent effect on the inferred M/L. A better approach would be to fit a two-component model to the light profile: one component to fit the central core, and the other to fit the outer ‘envelope’. As a MFL profile is assumed in the modelling, the mass will become more centrally concentrated, and this may further increase the derived ‘upper limits’.

8.3.2 Follow-up observations

Several galaxies have closely projected single-imaged background sources. These warrant deeper observations. The best candidate is J0202-5055, which has three background sources at different redshifts, each of which could be multiply imaged (see Figure 5.8). The closest candidate lensed image is separated by 1.92 arcsec. For an IMF consistent with the MW, the source will be intrinsically multiply imaged. Targets from MaNGA have been followed-up and confirmed with deeper IFU observations (Smith et al., 2020). A similar strategy could be applied to J0202-5055.

Candidates with a small angular separation would benefit from adaptive optics assisted observations. In this way, the detection depths of future 30m-class telescopes could be tested with a current 8m-class telescope.

8.3.3 Current/Future Instruments and Surveys

Although targeted observations have the highest percentage yield, the current and future IFU surveys will cover tens if not hundreds of thousands of galaxies. Within these huge datasets, many new lenses will be detected. This section will briefly describe some of the ongoing and future IFU surveys.

- **Mapping Nearby Galaxies at the Apache Point Observatory** (MaNGA, Bundy et al., 2015)**:** This survey will finish in early 2020. It will target 10^4 galaxies, in the range $z = 0.01$–0.15, which are selected to have an approximately flat distribution in stellar mass ($M > 10^9\,M_\odot$), and a uniform radial coverage of $R_{\rm Eff}$. The instrument has a large wavelength range, 3600–10300 Å, with a hexabundle of fibres, each of size of 2 arcsec. Candidate lenses were reported from a sample of 2812 galaxies (Talbot et al., 2018), and two have been confirmed (Smith, 2017; Smith et al., 2020). Compared to SNELLS and MNELLS the majority of candidate lenses are at $\sigma \sim 200\,{\rm kms}^{-1}$. The massive, comparable σ galaxies mostly lie at $z \simeq 0.1$. A

total of ~ 8 massive lenses are predicted if the current yield of confirmed lenses are extrapolated to the full sample.

- **Sydney-AAO Multi-object Integral field spectrograph** (SAMI, Croom et al., 2012; Bryant et al., 2015)**:** Between 2013 and 2018 this survey targeted ~ 3400 galaxies, in the range $z = 0.004$–0.095 with masses $> 10^{8.2}\,M_{\odot}$. Currently, public data release two contains 1559 galaxies (Scott et al., 2018). The wavelength coverage is split into two arms, 3700–5700 Å and 6250–7350 Å. There are 71 fibres, each of which subtends 1.6 arcsec on the sky. Compared to MNELLS or SNELLS, the wavelength coverage significantly restricts the background volume. To date, no lenses have been reported from SAMI.

- **Hector at the Anglo-Australian Telescope** (Bland-Hawthorn, 2015)**:** This survey will commence in the next few years. When the instrument was proposed, the hexabundle contained two components, a coarser sampled outer ring (61 fibres) and an increased angular sampling in the core (34 fibres) of target galaxies. There will be 10^5 galaxies targeted with a wavelength range 3700–9000 Å. As Hector will target 10 times more galaxies than MaNGA, many new strong-gravitational lenses will be discovered. For a factor of ten larger yield, there could be sufficient massive galaxies to constrain the IMF within the ETG population at $\sigma \simeq 300\,\mathrm{kms}^{-1}$.

In addition to the surveys with IFUs, others using both single fibre observations or broad-band imaging will observe thousands, if not millions of galaxies in the next ten years.

- **ESO-*Gaia* mission:** This optical broad-band survey aims to produce a census of 1 billion stars in the MW. In the process, numerous extragalactic objects such as unresolved galaxies or QSOs are detected. Both data releases, DR1 and DR2, have been exploited to uncover new quasar lenses, either by comparing the source and lens colour (Lemon et al., 2018, 2019) or comparing relative positions of multiple closely projected detections to simulated lenses (Delchambre et al., 2018, 2019). However, typically these systems have distant or faint lenses. For these systems,

the lensed images are brighter than the lens. Specific to the low-z lens search, the brighter outer image of J0403-0239 was detected in DR1. Therefore, a search could be conducted for detected sources near to massive ETGs. *Gaia* may find a handful of candidate lenses which are suitable for IMF studies.

There will be several wide-area deep surveys completed within the next ten years. In the optical/infra-red, there is the Dark Energy Survey (DES), the DECam Legacy Survey of the SDSS Equatorial Sky (DECaLs), the Large Synoptic Survey Telescope (LSST), and *Euclid*. At radio wavelengths, the Square-Kilometer Array (SKA), will survey 3π sr. The challenge with these surveys will be efficiently searching for lenses within the huge data sets. However, when those issues are addressed the number of new lens systems will be orders of magnitudes larger than at present. Estimates of the number of galaxy-galaxy lenses discovered by each survey are 2400 (DES), 120000 (LSST) and 170000 (*Euclid*) and 10^5 (SKA), (Collett, 2015; McKean et al., 2015).

The volume of observational data which will become available in the next ten years will change the statistical nature of gravitational strong-lens analyses. As an alternative to working with the few systems available, for a given problem, the lenses will be 'cherry-picked'. However, the low-z lenses are typically very bright compared to the background source, and depending on the detection technique, these may be missed, especially within broad-band imaging. Therefore, the short term goal of increasing the sample size to tens of lenses is still required. Dedicated searches return the highest yield. With the current generation of telescopes, turning any galaxy into a strong-gravitational lens may require an unreasonably long integration time to reach a depth to statistically observe a background emission line object. However, the next generation of massive telescopes (i.e. E-ELT) may reach these depths in relatively short observations.

The coming years will produce the lenses and the detailed lens modelling techniques to robustly investigate the universality of the IMF within these massive ETGs.

Bibliography

Alcock C., et al., 1993, Nature, 365, 621

Alton P. D., Smith R. J., Lucey J. R., 2018, MNRAS, 478, 4464

Auger M. W., Treu T., Bolton A. S., Gavazzi R., Koopmans L. V. E., Marshall P. J., Bundy K., Moustakas L. A., 2009, ApJ, 705, 1099

Auger M. W., Treu T., Gavazzi R., Bolton A. S., Koopmans L. V. E., Marshall P. J., 2010, ApJ, 721, L163

Bacon R., et al., 2001, MNRAS, 326, 23

Bacon R., et al., 2014, The Messenger, 157, 13

Barnabè M., Czoske O., Koopmans L. V. E., Treu T., Bolton A. S., 2011, MNRAS, 415, 2215

Bartelmann M., Schneider P., 2001, Phys. Rep., 340, 291

Bastian N., Covey K. R., Meyer M. R., 2010, ARA&A, 48, 339

Baumgardt H., Hilker M., Sollima A., Bellini A., 2019, MNRAS, 482, 5138

Bernardi M., Sheth R. K., Dominguez-Sanchez H., Fischer J. L., Chae K. H., Huertas-Company M., Shankar F., 2018, MNRAS, 477, 2560

Bessell M. S., 2005, Annual Review of Astronomy and Astrophysics, 43, 293

Blackburne J. A., Pooley D., Rappaport S., Schechter P. L., 2011, ApJ, 729, 34

Bland-Hawthorn J., 2015, in Ziegler B. L., Combes F., Dannerbauer H., Verdugo M., eds, IAU Symposium Vol. 309, Galaxies in 3D across the Universe. pp 21–28 (arXiv:1410.3838), doi:10.1017/S1743921314009247

Blanton M. R., Roweis S., 2007, AJ, 133, 734

Bolton A. S., Burles S., Koopmans L. V. E., Treu T., Moustakas L. A., 2006, ApJ, 638, 703

Bolton A. S., Burles S., Koopmans L. V. E., Treu T., Gavazzi R., Moustakas L. A., Wayth R., Schlegel D. J., 2008, ApJ, 682, 964

Bovy J., 2017, MNRAS, 470, 1360

Brownstein J. R., et al., 2012, ApJ, 744, 41

Bruzual G., Charlot S., 2003, MNRAS, 344, 1000

Bryant J. J., et al., 2015, MNRAS, 447, 2857

Bundy K., et al., 2015, ApJ, 798, 7

Campbell L. A., et al., 2014, MNRAS, 443, 1231

Cappellari M., 2012, arXiv e-prints, p. arXiv:1211.7009

Cappellari M., 2016, ARA&A, 54, 597

Cappellari M., Emsellem E., 2004, PASP, 116, 138

Cappellari M., et al., 2006, MNRAS, 366, 1126

Cappellari M., et al., 2011, MNRAS, 413, 813

Cappellari M., et al., 2012, Nature, 484, 485

Cappellari M., et al., 2013, MNRAS, 432, 1709

Carter D., Visvanathan N., Pickles A. J., 1986, ApJ, 311, 637

Cenarro A. J., Gorgas J., Vazdekis A., Cardiel N., Peletier R. F., 2003, MNRAS, 339, L12

Chabrier G., 2003, PASP, 115, 763

Chabrier G., Hennebelle P., Charlot S., 2014, ApJ, 796, 75

Chambers K. C., et al., 2016, preprint, (arXiv:1612.05560)

Chen G. C. F., et al., 2019, MNRAS, 490, 1743

Chilingarian I. V., Zolotukhin I. Y., 2012, MNRAS, 419, 1727

Chilingarian I. V., Melchior A.-L., Zolotukhin I. Y., 2010, MNRAS, 405, 1409

Choi Y.-Y., Reynolds C. S., Heinz S., Rosenberg J. L., Perlman E. S., Yang J., 2004, ApJ, 606, 185

Clowe D., Bradač M., Gonzalez A. H., Markevitch M., Randall S. W., Jones C., Zaritsky D., 2006, ApJ, 648, L109

Collett T. E., 2015, ApJ, 811, 20

Collett T. E., et al., 2018, Science, 360, 1342

Collier W. P., Smith R. J., Lucey J. R., 2018a, MNRAS, 473, 1103

Collier W. P., Smith R. J., Lucey J. R., 2018b, MNRAS, 478, 1595

Collier W. P., Smith R. J., Lucey J. R., 2020, MNRAS,

Conroy C., van Dokkum P., 2012a, ApJ, 747, 69

Conroy C., van Dokkum P. G., 2012b, ApJ, 760, 71

Conroy C., Gunn J. E., White M., 2009, ApJ, 699, 486

Couture J., Hardy E., 1993, ApJ, 406, 142

Croom S. M., et al., 2012, MNRAS, 421, 872

Daddi E., et al., 2005, ApJ, 626, 680

Dalal N., Kochanek C. S., 2002, ApJ, 572, 25

Delchambre L., et al., 2018, arXiv e-prints, p. arXiv:1807.02845

Delchambre L., et al., 2019, A&A, 622, A165

Dey A., et al., 2019, AJ, 157, 168

Djorgovski S., Davis M., 1987, ApJ, 313, 59

Dyson F. W., Eddington A. S., Davidson C., 1920, Philosophical Transactions of the Royal Society of London Series A, 220, 291

Eggen O. J., Lynden-Bell D., Sandage A. R., 1962, ApJ, 136, 748

Eisenhauer F., et al., 2003, in Iye M., Moorwood A. F. M., eds, Proc. SPIEVol. 4841, Instrument Design and Performance for Optical/Infrared Ground-based Telescopes. pp 1548–1561 (arXiv:astro-ph/0306191), doi:10.1117/12.459468

Elmegreen B. G., Scalo J., 2006, ApJ, 636, 149

Estrada-Carpenter V., et al., 2019, ApJ, 870, 133

Evans N. W., Witt H. J., 2003, MNRAS, 345, 1351

Faber S. M., Jackson R. E., 1976, ApJ, 204, 668

Fassnacht C. D., Xanthopoulos E., Koopmans L. V. E., Rusin D., 2002, ApJ, 581, 823

Ferreras I., La Barbera F., de La Rosa I. G., Vazdekis A., de Carvalho R. R., Falcon-Barroso J., Ricciardelli E., 2013, MNRAS, 429, L15

Gaia Collaboration et al., 2018, A&A, 616, A1

Galbany L., Collett T. E., Méndez-Abreu J., Sánchez S. F., Anderson J. P., Kuncarayakti H., 2018, preprint, (arXiv:1803.09277)

Geha M., et al., 2013, ApJ, 771, 29

Gonzaga S., 2012, The DrizzlePac Handbook

Graves G. J., Faber S. M., 2010, ApJ, 717, 803

Green G. M., et al., 2018, preprint, (arXiv:1801.03555)

Greene J. E., et al., 2019, ApJ, 874, 66

Haines C. P., et al., 2018, MNRAS, 481, 1055

Herenz E. C., et al., 2017, preprint, (arXiv:1705.08215)

Hinton S. R., Davis T. M., Lidman C., Glazebrook K., Lewis G. F., 2016, Astronomy and Computing, 15, 61

Hoekstra H., Jain B., 2008, Annual Review of Nuclear and Particle Science, 58, 99

Hubble E., 1923, Popular Astronomy, 31, 644

Hubble E. P., 1925, Popular Astronomy, 33, 252

Huchra J. P., et al., 2012, ApJS, 199, 26

Jarrett T. H., Chester T., Cutri R., Schneider S., Skrutskie M., Huchra J. P., 2000, AJ, 119, 2498

Jeans J. H., 1922, MNRAS, 82, 122

Jedrzejewski R. I., 1987, in de Zeeuw P. T., ed., IAU Symposium Vol. 127, Structure and Dynamics of Elliptical Galaxies. pp 37–44

Jones D. H., et al., 2009, MNRAS, 399, 683

Keeton C. R., 2001, preprint, (arXiv:0102340)

Keeton C. R., Kochanek C. S., 1997, ApJ, 487, 42

Keeton C. R., Kochanek C. S., Seljak U., 1997, ApJ, 482, 604

Kochanek C. S., 2006, in Meylan G., Jetzer P., North P., Schneider P., Kochanek C. S., Wambsganss J., eds, Saas-Fee Advanced Course 33: Gravitational Lensing: Strong, Weak and Micro. pp 91–268

Kochanek C. S., Keeton C. R., McLeod B. A., 2001, ApJ, 547, 50

Kochanek C. S., Morgan N. D., Falco E. E., McLeod B. A., Winn J. N., Dembicky J., Ketzeback B., 2006, ApJ, 640, 47

Komatsu E., et al., 2011, ApJS, 192, 18

Koopmans L. V. E., Treu T., Bolton A. S., Burles S., Moustakas L. A., 2006, ApJ, 649, 599

Krajnović D., Emsellem E., den Brok M., Marino R. A., Schmidt K. B., Steinmetz M., Weilbacher P. M., 2018, MNRAS, 477, 5327

Kroupa P., 2001, MNRAS, 322, 231

Kroupa P., Tout C. A., Gilmore G., 1993, MNRAS, 262, 545

La Barbera F., Ferreras I., Vazdekis A., de la Rosa I. G., de Carvalho R. R., Trevisan M., Falcón-Barroso J., Ricciardelli E., 2013, MNRAS, 433, 3017

La Barbera F., Vazdekis A., Ferreras I., Pasquali A., Cappellari M., Martín-Navarro I., Schönebeck F., Falcón-Barroso J., 2016, MNRAS, 457, 1468

La Barbera F., et al., 2019, MNRAS, 489, 4090

Laine S., van der Marel R. P., Lauer T. R., Postman M., O'Dea C. P., Owen F. N., 2003, AJ, 125, 478

Larkin J., et al., 2006, OSIRIS: a diffraction limited integral field spectrograph for Keck. p. 62691A, doi:10.1117/12.672061

Leavitt H. S., Pickering E. C., 1913, Harvard College Observatory Circular, 179, 1

Lee C.-H., 2017, Research Notes of the American Astronomical Society, 1, 12

Lehár J., et al., 2000, ApJ, 536, 584

Lemon C. A., Auger M. W., McMahon R. G., Ostrovski F., 2018, MNRAS, 479, 5060

Lemon C. A., Auger M. W., McMahon R. G., 2019, MNRAS, 483, 4242

Li H., et al., 2017, ApJ, 838, 77

Loeb A., Peebles P. J. E., 2003, ApJ, 589, 29

Lucey J. R., Smith R. J., Schechter P. L., Bosh A. S., Levine S. E., 2018, Research Notes of the American Astronomical Society, 2, 62

Madau P., Dickinson M., 2014, ARA&A, 52, 415

Mancone C. L., Gonzalez A. H., 2012, PASP, 124, 606

Mao S., Schneider P., 1998, MNRAS, 295, 587

Maraston C., 1998, MNRAS, 300, 872

Maraston C., 2005, MNRAS, 362, 799

Martín-Navarro I., La Barbera F., Vazdekis A., Falcón-Barroso J., Ferreras I., 2015, MNRAS, 447, 1033

McDonald M., Veilleux S., Rupke D. S. N., Mushotzky R., 2010, ApJ, 721, 1262

McKean J., et al., 2015, in Advancing Astrophysics with the Square Kilometre Array (AASKA14). p. 84 (arXiv:1502.03362)

McMahon R. G., Banerji M., Gonzalez E., Koposov S. E., Bejar V. J., Lodieu N., Rebolo R., VHS Collaboration 2013, The Messenger, 154, 35

Messier C., 1781, Catalogue des Nébuleuses et des Amas d'Étoiles (Catalog of Nebulae and Star Clusters), Connoissance des Temps ou des Mouvements Célestes

Metcalf R. B., et al., 2019, A&A, 625, A119

Miller G. E., Scalo J. M., 1979, ApJS, 41, 513

Morgan C. W., Kochanek C. S., Morgan N. D., Falco E. E., 2010, ApJ, 712, 1129

Naab T., Johansson P. H., Ostriker J. P., Efstathiou G., 2007, ApJ, 658, 710

Navarro J. F., Frenk C. S., White S. D. M., 1996, ApJ, 462, 563

Newman A. B., Smith R. J., Conroy C., Villaume A., van Dokkum P., 2017, ApJ, 845, 157

Nightingale J., Dye S., Massey R., 2017, preprint, (arXiv:1708.07377)

Nightingale J. W., Massey R. J., Harvey D. R., Cooper A. P., Etherington A., Tam S.-I., Hayes R. G., 2019, MNRAS, 489, 2049

Offner S. S. R., Clark P. C., Hennebelle P., Bastian N., Bate M. R., Hopkins P. F., Moraux E., Whitworth A. P., 2014, Protostars and Planets VI, pp 53–75

Oldham L., Auger M., 2018, MNRAS, 474, 4169

Oldham L., et al., 2017a, MNRAS, 465, 3185

Oldham L., Auger M., Fassnacht C. D., Treu T., Koopmans L. V. E., Lagattuta D., McKean J., Vegetti S., 2017b, MNRAS, 470, 3497

Oppenheimer B. D., Davé R., Katz N., Kollmeier J. A., Weinberg D. H., 2012, MNRAS, 420, 829

Parikh T., et al., 2018, MNRAS, 477, 3954

Peebles P. J. E., 1971, A&A, 11, 377

Peng C. Y., Ho L. C., Impey C. D., Rix H.-W., 2002, AJ, 124, 266

Peng C. Y., Ho L. C., Impey C. D., Rix H.-W., 2010, AJ, 139, 2097

Piffaretti R., Arnaud M., Pratt G. W., Pointecouteau E., Melin J. B., 2011, A&A, 534, A109

Planck Collaboration et al., 2016, A&A, 594, A13

Planck Collaboration et al., 2018, arXiv e-prints, p. arXiv:1807.06209

Posacki S., Cappellari M., Treu T., Pellegrini S., Ciotti L., 2015, MNRAS, 446, 493

Press W. H., Schechter P., 1974, ApJ, 187, 425

Reid I. N., Gizis J. E., 1997, AJ, 113, 2246

Ritondale E., Vegetti S., Despali G., Auger M. W., Koopmans L. V. E., McKean J. P., 2019, MNRAS, 485, 2179

Rusin D., Kochanek C. S., Keeton C. R., 2003, ApJ, 595, 29

Rusu C. E., Berghea C. T., Fassnacht C. D., More A., Seman E., Nelson G. J., Chen G. C. F., 2019, MNRAS, 486, 4987

Salpeter E. E., 1955, ApJ, 121, 161

Sandage A., 2005, ARA&A, 43, 581

Sarzi M., Spiniello C., La Barbera F., Krajnović D., van den Bosch R., 2018, MNRAS, 478, 4084

Scalo J. M., 1986, Fundamentals Cosmic Phys., 11, 1

Schawinski K., et al., 2014, MNRAS, 440, 889

Schaye J., et al., 2015, MNRAS, 446, 521

Schechter P. L., Wambsganss J., 2002, ApJ, 580, 685

Schechter P. L., Pooley D., Blackburne J. A., Wambsganss J., 2014, ApJ, 793, 96

Schlafly E. F., Finkbeiner D. P., 2011, ApJ, 737, 103

Schlafly E. F., et al., 2014, ApJ, 789, 15

Schlegel D. J., Finkbeiner D. P., Davis M., 1998, ApJ, 500, 525

Scott N., et al., 2018, MNRAS, 481, 2299

Shapley H., Curtis H. D., 1921, Bulletin of the National Research Council, 2, 171

Sharples R., et al., 2013, The Messenger, 151, 21

Shu Y., et al., 2015, ApJ, 803, 71

Smith R. J., 2014, MNRAS, 443, L69

Smith R. J., 2017, MNRAS, 464, L46

Smith R. J., Lucey J. R., 2013, MNRAS, 434, 1964

Smith R. J., et al., 2004, AJ, 128, 1558

Smith R. J., Blakeslee J. P., Lucey J. R., Tonry J., 2005, ApJ, 625, L103

Smith R. J., Lucey J. R., Carter D., 2012, MNRAS, 426, 2994

Smith R. J., Lucey J. R., Conroy C., 2015, MNRAS, 449, 3441

Smith R. J., Lucey J. R., Collier W. P., 2018, MNRAS, 481, 2115

Smith R. J., Collier W. P., Ozaki S., Lucey J. R., 2020, MNRAS, 493, L33

Sollima A., 2019, MNRAS, 489, 2377

Somerville R. S., Davé R., 2015, ARA&A, 53, 51

Sonnenfeld A., Leauthaud A., Auger M. W., Gavazzi R., Treu T., More S., Komiyama Y., 2018, MNRAS, 481, 164

Sonnenfeld A., Jaelani A. T., Chan J., More A., Suyu S. H., Wong K. C., Oguri M., Lee C.-H., 2019, A&A, 630, A71

Spiniello C., Trager S. C., Koopmans L. V. E., Chen Y. P., 2012, ApJ, 753, L32

Spiniello C., Trager S. C., Koopmans L. V. E., 2015, ApJ, 803, 87

Spinrad H., 1962, ApJ, 135, 715

Spinrad H., Taylor B. J., 1971, ApJS, 22, 445

Stockton A., 1980, ApJ, 242, L141

Su Y., Irwin J. A., White Raymond E. I., Cooper M. C., 2015, ApJ, 806, 156

Suyu S. H., Marshall P. J., Hobson M. P., Bland ford R. D., 2006, MNRAS, 371, 983

Talbot M. S., et al., 2018, MNRAS, 477, 195

Thomas D., Maraston C., Bender R., Mendes de Oliveira C., 2005, ApJ, 621, 673

Thomas J., et al., 2011, MNRAS, 415, 545

Torrey P., et al., 2018, MNRAS, 477, L16

Treu T., 2010, ARA&A, 48, 87

Treu T., Koopmans L. V. E., 2004, ApJ, 611, 739

Treu T., Auger M. W., Koopmans L. V. E., Gavazzi R., Marshall P. J., Bolton A. S., 2010, ApJ, 709, 1195

Vaughan S. P., Davies R. L., Zieleniewski S., Houghton R. C. W., 2018, MNRAS, 479, 2443

Vazdekis A., Sánchez-Blázquez P., Falcón-Barroso J., Cenarro A. J., Beasley M. A., Cardiel N., Gorgas J., Peletier R. F., 2010, MNRAS, 404, 1639

Vegetti S., Koopmans L. V. E., 2009, MNRAS, 392, 945

Villaume A., Conroy C., Johnson B., Rayner J., Mann A. W., van Dokkum P., 2017, ApJS, 230, 23

Walsh D., Carswell R. F., Weymann R. J., 1979, Nature, 279, 381

Wang Y., Mukherjee P., 2006, ApJ, 650, 1

Whitaker K. E., van Dokkum P. G., Brammer G., Franx M., 2012, ApJ, 754, L29

Witt H. J., Mao S., 1997, MNRAS, 291, 211

Wong K. C., et al., 2019, arXiv e-prints, p. arXiv:1907.04869

York D. G., et al., 2000, AJ, 120, 1579

Young P., Gunn J. E., Kristian J., Oke J. B., Westphal J. A., 1980, ApJ, 241, 507

Young L. M., et al., 2011, MNRAS, 414, 940

Young L. M., Serra P., Krajnović D., Duc P.-A., 2018, MNRAS, 477, 2741

Zieleniewski S., Houghton R. C. W., Thatte N., Davies R. L., Vaughan S. P., 2017, MNRAS, 465, 192

Zwicky F., 1937, Phys. Rev., 51, 290

van Dokkum P. G., Conroy C., 2010, Nature, 468, 940

van Dokkum P. G., et al., 2008, ApJ, 677, L5

van Dokkum P., Conroy C., Villaume A., Brodie J., Romanowsky A. J., 2017, ApJ, 841, 68

van de Kamp P., 1971, ARA&A, 9, 103

van den Bosch R. C. E., 2016, ApJ, 831, 134

van der Wel A., et al., 2011, ApJ, 730, 38